Mixed Valency and Anionogenic Magnetism in Alkali Metal Oxides

Front cover page:Author's artistic and imaginative interpretation of glove box chemistry and magnetism generated by molecular oxygen ions (anionogenic magnetism). Cover page picture sketched by **Lalitha Saradyamini Nanduri**.

university of groningen / faculty of mathematics and natural sciences / zernike institute for advanced materials

The work described in this thesis was performed in the "Solid State Materials for Electronics" group of the Zernike Institute for Advanced Materials at the University of Groningen, The Netherlands. This work is supported by the University of Groningen.

Printed by: Offpage, Amsterdam. www.offpage.nl

Zernike Institute for Advanced Materials PhD thesis series 2012-23

ISSN 1570-1530

ISBN: 978-90-367-5862-8 (Paper version)

ISBN: 978-90-367-5863-5(Electronic version)

RIJKSUNIVERSITEIT GRONINGEN

Mixed Valency and Anionogenic Magnetism in Alkali Metal Oxides

Proefschrift

ter verkrijging van het doctoraat in de
Wiskunde en Natuurwetenschappen
aan de Rijksuniversiteit Groningen
op gezag van de
Rector Magnificus, dr. E. Sterken,
in het openbaar te verdedigen op
vrijdag 9 november 2012
om 11:00 uur

door

Shivakumara Giriyapura Parameshwarappa

geboren op 5 mei 1983
te Giriyapura, India

Promotor:	Prof. dr. T.T.M. Palstra
Copromotor:	Dr. G.R. Blake
Beoordelingscommissie:	Prof. dr. P. Rudolf
	Prof. dr. A. Maignan
	Prof. dr. C. Pappas

Dedicated to

Sangappa & Shantha Parameshwarappa

"Nothing is too wonderful to be true if it is consistent with the laws of nature".-Michael Faraday.

Contents

Preface **x**

1 Introduction to Mixed Valency and Anionogenic Magnetism in Alkali Metal Oxides **1**

1.1 Molecular oxygen ions and their compounds 3

1.2 Anionogenic Magnetism in Alkali oxides 5

1.2.1 Molecular ordering and orbital degeneracy in alkali oxides: structural properties 6

1.2.2 Magnetic properties of alkali oxides 9

1.2.3 Cooperative phenomena and magnetic exchange interactions 10

1.2.4 Magnetogyration and field induced magnetic transitions 15

1.3 Mixed Valency in Alkali Oxides 16

1.4 Electron transfer (charge transfer) phenomena 19

1.5 Motivation of this thesis 21

Bibliography **22**

2 Synthesis and Characterization of Alkali Metal Oxides **29**

2.1 Synthesis of alkali metal oxides and sample processing . . . 29

2.1.1 Synthesis of alkali oxides by solution method 30
2.1.2 Controlled thermal decomposition 36
2.2 Structural Characterization 37
2.2.1 X-Ray Powder Diffraction (XRPD) 37
2.2.2 Neutron Diffraction 39
2.3 Physical and Chemical Property Measurements 40
2.3.1 Magnetic property measurements (MPMS) 40
2.3.2 Capacitance measurements 42
2.3.3 Thermal Analysis: (Differential Scanning Calorimetry (DSC) – Thermo-Gravimetric Analysis (TGA)) . 43
2.3.4 Raman Spectroscopic analysis 44

Bibliography **46**

3 Anionogenic Magnetism in Mixed Valent $K_xBa_{1-x}O_2$ **47**
3.1 Introduction 48
3.2 Experimental 49
3.2.1 Synthesis and characterization 49
3.3 Results 52
3.3.1 X-ray and neutron diffraction 52
3.3.2 Magnetic properties 57
3.4 Discussion 64
3.5 Conclusion 66

Bibliography **68**

4 Charge Transfer in Mixed-Valent $K_xBa_{1-x}O_2$ **71**
4.1 Introduction 72
4.1.1 Mixed valence: Robin–Day model 74
4.2 Experimental 77
4.3 Results and discussion 78
4.3.1 Raman spectroscopy analysis 80
4.3.2 Theoretical implications 81

4.3.3 Photo-induced charge transfer 83
4.4 Summary and conclusion 92

Bibliography **95**

5 Sodium Superoxide (NaO_2) -Mixed valency and polymorphism **99**
5.1 Introduction 100
5.2 Experiments and techniques 102
5.2.1 Synthesis 102
5.3 Results 107
5.3.1 $Na(O_2)_{1-x}(OH)_x$ 107
5.3.2 Sodium superoxide (NaO_2) 115
5.4 Summary and Conclusion 121

Bibliography **123**

6 Non-stoichiometry and Anionogenic Magnetism in AO_{2-x} (A=Cs, K) **125**
6.1 Introduction 126
6.2 Experimental 128
6.2.1 Synthesis 128
6.3 Results and Discussion 131
6.3.1 Non-stochiometric CsO_{2-x} 131
6.3.2 Non-stoichiometric KO_{2-x} 140
6.4 Summary 146

Bibliography **148**

Summary and conclusion **151**

Samenvatting en conclusies **157**

Acknowledgement **163**

Chapter 1

Introduction to Mixed Valency and Anionogenic Magnetism in Alkali Metal Oxides

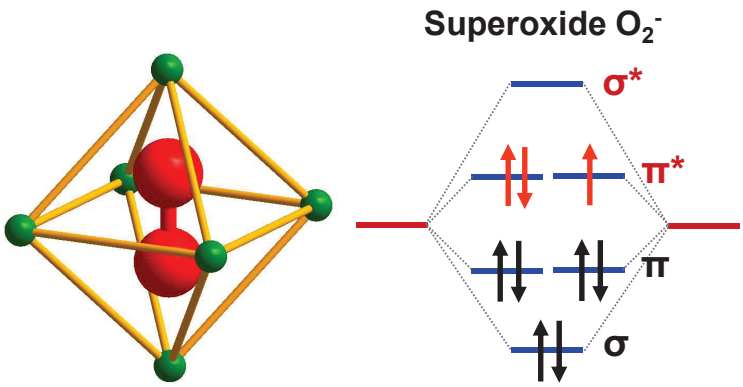

In the past few decades the evolution of many of our modern technologies has improved our quality of life in ways that would previously have been almost unimaginable. The development of technology goes hand in hand with the development of materials and chemical compounds, without which these technologies could not function. The focus of scientific research thus moves toward a greater understanding of complex systems, in which new materials often play an important role. In this thesis the focus lies on new materials based on oxygen. The gas of life, oxygen, is believed to have been essential ever since life began to exist on earth. If we look at the current composition of our atmosphere, the oxygen content is 21 % compared to the nitrogen content of 79 %, with trace amounts of inert gases, CO_2 and water. The importance of oxygen became apparent with time as man evolved and gained an understanding of Mother Nature's secrets. As man evolves, his curiosity is exerted around him and is also applied to the need for survival. Thus, the gas of life has been a constant concern in many aspects from the beginning of life. Today, a wide variety of oxygen-containing materials are essential for technology due to their tremendous applicability and robustness [1,2]. This is largely due to the special nature of oxygen, which is able to form both ionic and covalent bonds with a wide range of other elements, which makes oxides tremendously interesting materials in many senses. Molecular oxygen (O_2), the product of photosynthesis, is not only known as the gas of life, but is also an electro-active species that is of use in many ways in chemistry and physics, for example in the field of catalysis [3,4]. Oxygen has two allotropes, O_2 and O_3 (ozone). Both forms can exist in the anionic state, giving the species superoxide (O_2^-), peroxide (O_2^{2-}) and ozonide (O_3^-). However, ionic compounds containing ozonide, superoxide and peroxide have been relatively little explored [5]. Their scientific and technological potential are studied as the main focus of this thesis.

1.1 Molecular oxygen ions and their compounds

The ionic forms of the dioxygen molecule are shown in Fig. 1.1 as molecular orbital diagrams. These ions are formed by adding or removing electrons from the antibonding π^* level of diatomic molecular oxygen (O_2). In other words, the oxidation and reduction of molecular oxygen yields molecules with different oxidation states.

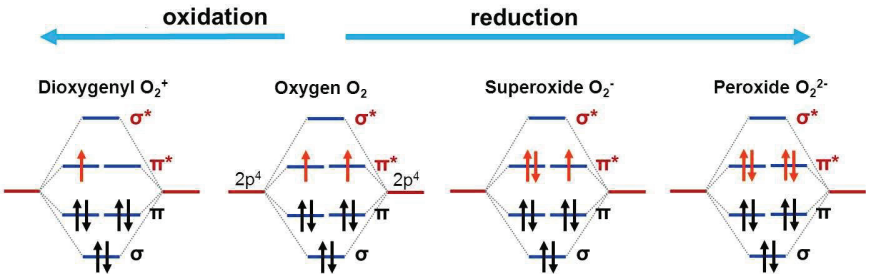

Figure 1.1: Molecular orbital diagrams of diatomic molecular oxygen ions.

The O_2^+ cation can only be stabilized in combination with MF_6^- anions (M = Sb, Pt, Ru, Rh, Au) and will not be discussed further in this thesis. Of interest here are the dioxygen anions superoxide and peroxide, which are stabilized by low valent, non-oxidizable and highly electropositive metallic cations to give ionic salts. Alkali metal cations meet these criteria and pure superoxides AO_2 of only sodium, potassium, rubidium and cesium are known. As is apparent in Fig. 1.1, the superoxide anion has one unpaired electron and is thus magnetic. Alkali superoxides are thus rare examples of magnetic materials where the magnetism is of p-electron origin, an aspect that is discussed further in Section 1.2 of this chapter. Non-magnetic alkali peroxides have composition A_2O_2. Compounds with the composition A_2O_3 are also known for A = Rb, Cs and are known as sesquioxides. These contain a nominal mixture of both magnetic superoxide ions and non-magnetic peroxide ions in the ratio 2:1, but can better be described as mixed-valent

materials, as discussed below. The thermodynamic stability of the alkali superoxides and sequioxides increases with atomic number. Therefore, pure samples of AO_2 and A_2O_3 with A = Rb and Cs are more readily synthesized. Although the synthesis and crystal structures of most of the alkali superoxides and sesquioxides have been reported in the literature, relatively little is known about their physical properties. The known alkali superoxides exhibit antiferromagnetic ordering below ∼15 K [6], but the magnetic exchange interactions involved have not been studied in detail. Even less is known about the properties and potential of mixed-valent alkali oxides. In this thesis the synthesis and physical properties of various mixed-valent alkali oxides are explored, as well as superoxides of the lighter alkali metal Na.

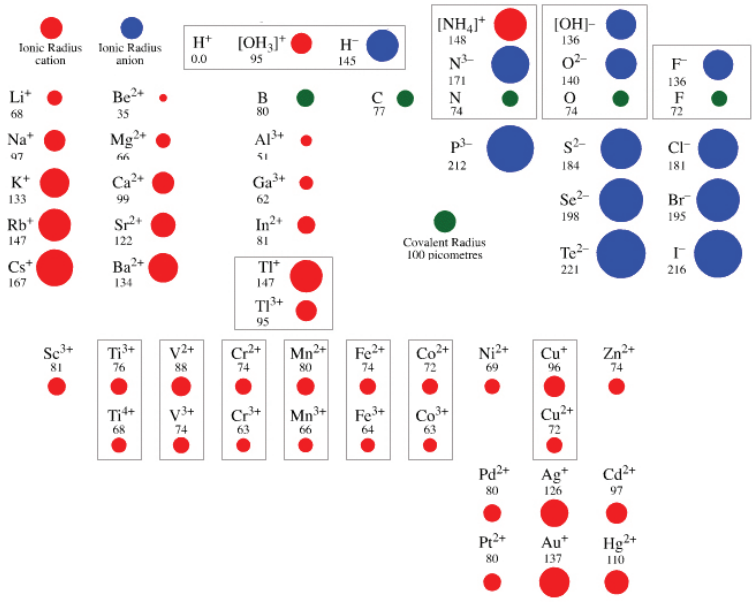

Figure 1.2: Radii of selected elements and ions [7].

1.2 Anionogenic Magnetism in Alkali oxides

In the field of magnetism nature has been inspiring us by revealing new materials with potential scientific and technological applications. The vast majority of magnetic materials that have been explored are based on d or f –electrons associated with elements in either the transition metal or rare earth series of the periodic table [8-10]. The scientific and technological potential of materials in which magnetism arises from p-electrons has been much less explored than those containing magnetic d- or f-block species. This is largely due to the limited number of examples of such materials; p-electrons tend to be paired in covalent bonds. However, the larger degree of delocalization of p-electrons compared to d or f-electrons and the expected low spin orbit coupling in the case of 2p systems may lead to novel physical properties. An increasing number of p-electron-based magnetic materials, often carbon-based, are being reported [11-17]. The larger delocalization of p-electrons compared to d- or f-electrons and the low spin-orbit coupling of 2p systems is likely to yield novel physical properties, evidenced by phenomena such as spin-polarized transport in graphene [18,19].

The magnetism in many carbon-based systems appears to be rather difficult to control and study systematically. Instead, magnetic dioxygen molecules can be used as convenient building blocks to construct model systems that exhibit p-electron magnetism in an ordered, crystalline environment. In a close packed crystal lattice the magnetic ions are in close proximity to each other, maximizing the magnetic exchange interactions. The complex temperature-pressure phase diagram of diatomic molecular oxygen (Fig. 1.3), which contains two unpaired electrons in doubly degenerate antibonding π^* molecular orbitals (Fig. 1.1), has been studied in detail and contains a number of different antiferromagnetic (AFM) phases [20-22]. On cooling under ambient pressure oxygen exhibits three-dimensional AFM ordering below 24 K. The crystal structure of this α-phase, along with that of the high-pressure δ-phase, is shown in Fig. 1.3. At pressures approaching 100 GPa metallic and superconducting phases have been discovered [23-25].

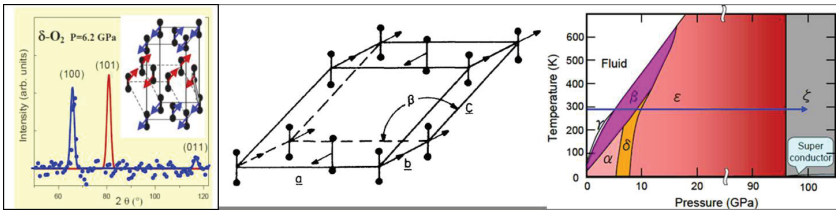

Figure 1.3: Influence of applied external pressure on solid molecular oxygen. (a) Crystal and magnetic structure of α-oxygen at ambient pressure below 24 K. (b) Crystal and magnetic structure of high-pressure δ-oxygen. (c) Temperature-pressure phase diagram. These figures were taken from Refs. [23-25].

1.2.1 Molecular ordering and orbital degeneracy in alkali oxides: structural properties

In order to understand the magnetic properties of alkali oxides, it is first necessary to understand their structural properties because structure and magnetism are closely coupled in these materials. In alkali superoxides (AO_2), peroxides (A_2O_2) and sesquioxides (A_2O_3), the key feature that determines the crystal structure is the relative orientations of the dioxygen anions. Alkali superoxides are stable at room temperature in two different forms depending on the ionic radius of the cations [5] (Fig. 1.4). Both structures are derived from the rocksalt (NaCl) structure, where the halides have been replaced by O_2^- ions, and due to this superoxides have been referred to as pseudo-halides [26]. KO_2, RbO_2 and CsO_2 adopt a body-centered tetragonal structure with space group I4/mmm where the anions are parallel along the *c*-axis [6]. NaO_2 adopts a cubic structure with space group Fm-3m in which there is no long-range rotational order, although it is thought that there is a preference for the body diagonal direction. The stability of LiO_2 is still under debate and it appears that no bulk sample has yet been synthesized. All of the alkali superoxides undergo a series of structural phase transitions on cooling. In NaO_2 the local anion ordering becomes long range below 230 K and a transition to the ordered pyrite

structure with space group Pa-3 occurs. Below 196 K the orthorhombic marcasite structure (Pnnm) is formed, where the parallel oxygen dimers have staggered tilts in alternating planes. Below 43 K there is a possibility that the structure changes further, but details have not been reported [27,28].

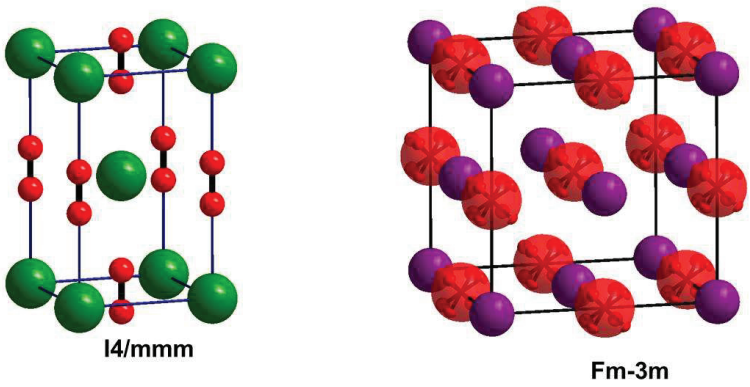

Figure 1.4: The two room temperature crystal structures of AO_2: tetragonal (left) and cubic (right).

Although KO_2 shows a room temperature tetragonal structure, it is thought that this is just an average structure and that small shifts and tilts of the oxygen dumbbells away from the *c*-axis occur, which can correlate to give small orthorhombic domains [5]. Cooling below 196 K leads to a monoclinic structure where the oxygen dumbbells are tilted by $\sim 20^{o}$ away from the *c*-axis and below ∼9 K a triclinic structure is formed. Similarly, RbO_2 and CsO_2 are tetragonal on average at room temperature, but probably consist of orthorhombic domains with short-range correlations of dumbbell tilts and shifts. An orthorhombic structure with small mean tilting of the dumbbells from the *c*-axis forms below ∼150 K and ∼190 K, respectively. For RbO_2 a monoclinic phase forms at 70 K [29]. For CsO_2 the orthorhombic structure remains down to very low temperature [30]. In all three compounds incommensurate reflections have been observed in X-ray diffraction

experiments, but details of the structures are unknown. In alkali superoxides there is orbital degeneracy in the cubic and I4/mmm phases (see Fig. 1.1) with a ground state of ${}^2\pi_g$ [27]. The driving force for the reorientation of the dumbbells and consequent structural phase transitions that occur on cooling is a lowering of the total energy of the system by breaking the degeneracy of the π^* orbitals of the superoxide ion. In KO_2, RbO_2 and CsO_2 it is thought that the orbital degeneracy is already broken at room temperature, where the local structure is probably of lower symmetry than I4/mmm. In NaO_2 the transition from the Pa-3 to Pnnm phases removes the orbital degeneracy. This situation has similarities with the Jahn-Teller effect in transition metal oxides where the energy of an orbitally degenerate system is lowered by structural distortion involving atomic shifts. This has important consequences in many materials, for example being involved in the mechanism that gives rise to colossal magneto resistance in the well-known alkaline-earth-doped rare-earth manganite perovskites $R_{1-x}A_xMnO_3$, where the orbitally active species is Mn^{3+} [31]. The two types of systems (for octahedral coordination) are compared schematically in Fig. 1.5, where the splitting of orbital energy levels is shown. In alkali superoxides the two degenerate π^* antibonding orbitals become split in energy by a lowering of symmetry. Superoxide ions, which are non-spherical, can tilt as well as shift in order to lift the orbital degeneracy, which gives an extra structural degree of freedom compared to Jahn-Teller-active transition metal systems. By way of comparison, Fig. 1.5 shows the distortion that occurs in the well-known alkaline-earth-doped rare-earth manganite perovskites $R_{1-x}A_xMnO_3$ to lift the degeneracy of the t_{2g} and e_g orbitals [32,33].

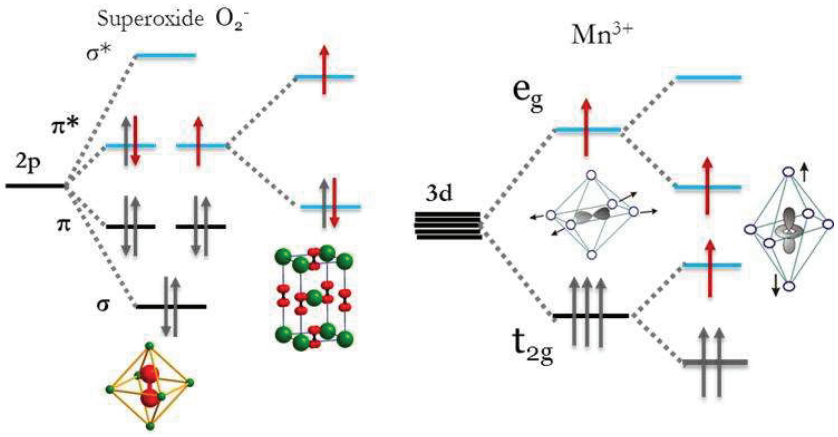

Figure 1.5: Schematic representation of Jahn-Teller distortion in octahedrally coordinated Mn^{3+} and superoxide compounds.

1.2.2 Magnetic properties of alkali oxides

In the alkali superoxides the molecular and magnetic ordering should not be considered separately but are coupled to one other [34]. Due to the different crystal structures, the magnetic interactions vary among different phases in the AO_2 series. However, one common feature is that in O_2^- ions the spins are thought to be always orthogonal to the molecular axis [35]. The lightest member of the AO_2 family is NaO_2, which is paramagnetic in the disordered cubic form at room temperature. When cooled into the ordered pyrite phase (Pa-3) the magnetic susceptibility starts to increase due to strengthening short-range correlations between neighboring dioxygen dumbbells. It is thought that these interactions are ferromagnetic based on Curie-Weiss fitting over the limited temperature range that this phase is stable [36,37]. A decrease in susceptibility occurs on cooling below 190K into the orthorhombic marcasite phase. Here it is thought that AFM short-range ordering sets in. This possibly occurs in one-dimensional fashion due to the parallel arrangement of the dioxygen dumbbells within each *ab*-plane, where direct exchange occurs [37,38]. Such a configuration

would also require orbital ordering where the lobes of half-filled π^* orbitals on adjacent anions point towards each other. Below 44K it is expected that three-dimensional AFM ordering begins, but the magnetic structure has not been reported in the literature. NaO_2 will be discussed in Chapter 5 in detail. KO_2 shows a more complex series of structural transitions on cooling, but remains paramagnetic down to 7 K where three dimensional AFM ordering sets in [39]. A neutron diffraction study suggested that spins within ab planes are coupled ferromagnetically, and adjacent planes are coupled antiferromagnetically along the c-axis. RbO_2 and CsO_2 order in three-dimensional AFM fashion below 15 K and 10 K, respectively, and are thought on the basis of ESR data to have similar magnetic structures to KO_2[6]. The mechanism of the magnetic exchange interactions in these three materials is unknown.

1.2.3 Cooperative phenomena and magnetic exchange interactions

Bulk magnetic behavior depends on the interactions at play between paramagnetic species in the crystal. The nature of these interactions and their length scales have been little studied in the alkali oxides. The possible magnetic interactions that occur in these materials will now be discussed. Long range order is usually three dimensional (3D) in nature, whereas short range order can often be 1D or 2D. In all cases the ordering can be ferromagnetic or antiferromagnetic. By using mean field theory for a 3D Heisenberg system in terms of the molecular field originating from the individual spins, it is often possible to explain ferromagnetic and antiferromagnetic interactions. The molecular field interacts with a number of nearest neighboring spins z. The molecular field constant between two nearest neighboring spins is related to Heisenberg's exchange interaction parameter (J) as follows:

$$\lambda = \frac{2zJ}{N_A g^2 \mu_B^2}$$

Here N_A is Avogadro's number, g is the gyromagnetic ratio and μ_B is the Bohr magneton. Heisenberg's Hamiltonian for magnetic exchange interactions is written as $H = -\sum J_{ab} S_a \cdot S_b$. Here $J_{ab}>0$ for ferromagnetic interactions and $J_{ab}< 0$ for antiferromagnetic interactions. In alkali oxides direct exchange, superexchange and double exchange are all possible. As these magnetic exchange interactions can have different origins, the possible interactions relevant to alkali oxides are discussed in detail below.

Direct Exchange

Direct exchange requires the direct overlap of orbitals on neighboring atoms or molecules, and will tend to occur more often for p-orbitals than for d-orbitals due to their more diffuse nature. Pauli's principle states that the total wave function for two identical fermions is anti-symmetric with respect to exchange of the fermions. Exchange interactions involve electrostatic interactions between overlapping orbitals, and electrons of parallel spin will be kept apart due to Coulomb repulsion whereas antiparallel spins can be coupled within the same orbital. When direct exchange occurs between half-filled orbitals of the same symmetry, the exchange will be antiferromagnetic [40]. In the alkali oxides this is thought to occur, for example, in the marcasite phase of NaO_2[38].

Superexchange

Compared to s and 2p orbitals, 3d orbitals are not as spatially extended, so direct exchange is not as likely in transition metal oxides. Often superexchange interactions between two metal sites are strongest, which occur via nonmagnetic intervening ligands as shown in Fig. 1.6. Energy minimization as a result of exchange forces neighboring spins into a parallel or antiparallel arrangement. For transition metals, the sign of the superexchange depends on the metal–oxygen–metal bond angle and the orbitals that are occupied. The relations between different orbital orientations are expressed in the Goodenough–Kanamori-Anderson rules [40]:

• Two occupied or empty orbitals that extend towards each other in a 180° bond results in antiferromagnetic coupling ($J<0$).

• Interacting filled and empty orbitals in a 180° bond lead to ferromagnetic super exchange.

• A metal-oxygen-metal bond of 90° results in an exchange integral $J>0$ which stabilizes weak ferromagnetic coupling.

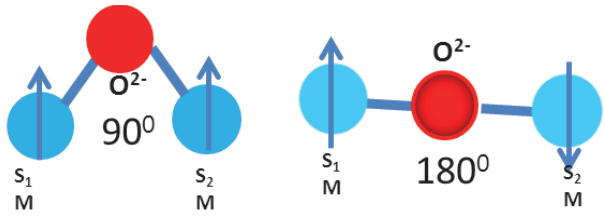

Figure 1.6: Schematic representation of superexchange in transition metals for 90° and 180° bond angles.

Similarly in alkali oxides it appears that superexchange interactions are important, but here the indirect exchange interaction involves the cations as intermediate ligands. Superexchange in AO_2 can probably be of different sign depending on the orientation of the anions and orbitals involved. For example, in KO_2 the spins are aligned ferromagnetically within the pseudo-tetragonal basal plane, but these planes are coupled antiferromagnetically [39]. The highly tilted anions are unfavorably arranged for direct exchange, thus superexchange must be responsible for the coupling. Superexchange in AO_2 has not been treated theoretically in the literature but it is likely that the Goodenough-Kanamori-Anderson rules still apply.

Double exchange

Double exchange is different to direct exchange and superexchange in that it involves the process of electron transfer between two ions with different valences, which leads to ferromagnetic behavior (Fig. 1.7). If the coherence length of the interactions is long then the material will tend to be

metallic. In the alkali superoxides it appears that magnetic interactions are dominated by direct exchange and superexchange. However, the situation is potentially different in mixed-valent alkali oxides such as the alkali sesquioxides where the π^* level contains a non-integral number of electrons. The possibility of double exchange in these materials is discussed in Section 1.3 below and can likely occur in analogous fashion to double exchange in mixed-valent transition metal systems like the alkaline-earth-doped rare-earth manganite perovskites $R_{1-x}A_xMnO_3$. Figure 1.7 shows a schematic representation of double exchange in the well-known alkaline-earth-doped rare-earth manganite perovskites $R_{1-x}A_xMnO_3$.

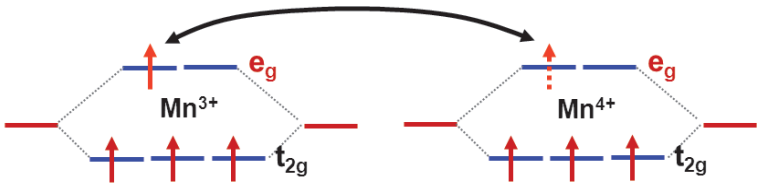

Figure 1.7: Schematic representation of double exchange in the well-known alkaline-earth-doped rare-earth manganite perovskites $R_{1-x}A_xMnO_3$.

Spin Glasses

In terms of structure, a glassy state refers to a frozen-in disordered arrangement of atoms. Similarly, a spin glass refers to a magnetic material with frozen-in disorder, often due to frustrated exchange interactions. Although there is no long-range ordering in a spin glass, there will still be interactions between the spins, which can be strong. Spin frustration is shown schematically for a triangular lattice antiferromagnet in Fig. 1.8. A degree of randomness in the spin arrangement is introduced, which can be either site randomness or bond randomness. These two types of randomness have different origins. Site randomness is normally observed in a dilute magnetic lattice where magnetic ions are doped into a non-magnetic lattice. Bond randomness is mostly due to varying interactions between nearest neighbor atoms or ions. This can arise due to geometrical frustration and competing

antiferromagnetic and ferromagnetic interactions. Frustration is crucial to the formation of this type of spin glass. For example, in Fig. 1.8 one of the spins in an isolated triangle cannot satisfy the condition of antiferromagnetic alignment. The frustration is then extended throughout bonds over the entire lattice.

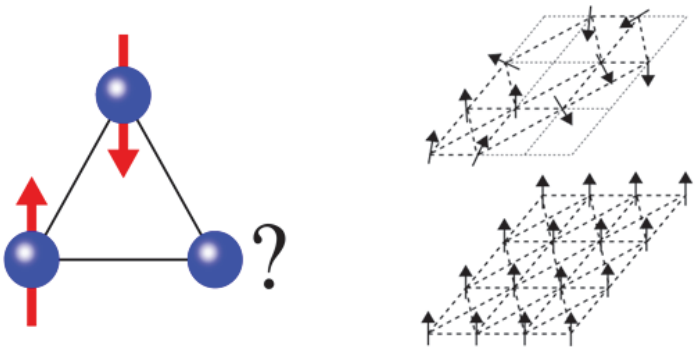

Figure 1.8: Illustration of frustration in spin glass compounds with antiferromagnetic exchange on a triangular lattice.

Many different kinds of systems show spin glass behavior, for example the metallic pyrochlore ruthenate $Ca_2Ru_2O_7$, semiconducting $K_xFe_{2-y}S_2$ and insulating $Rb_2Mn_{1-x}Cr_xCl_4$ [41-43]. Usually spin glass materials exhibit characteristic features in their bulk magnetization. These include splitting of the zero-field-cooled (ZFC) and field-cooled (FC) magnetization curves when measured versus temperature. A peak in the ZFC curve is often apparent at the temperature where the random spins are frozen, known as the freezing temperature (T_f) . However, ferromagnetic materials can also show splitting of the ZFC and FC curves due to the movement of domain walls. Therefore, other measurements such as the dependence of the magnetization on time are necessary to distinguish a spin glass from other magnetic systems. For a spin glass, when the sample is field cooled to below T_f and the field is then removed, the magnetization decays slowly with time and eventually approaches zero. For ferromagnetic materials a finite magnetization should remain on an indefinite time scale. The decay in magnetization

in a spin glass is often exponential [44] but can also follow a power law dependence [45]. A spin glass can also be distinguished by the dynamic probe of AC magnetization measurements, where the real and imaginary susceptibilities are measured. AC magnetization measurements performed at different frequencies show a shift in the peak of the real part at T_f towards higher temperature with increasing frequency. This is an indication of slow spin dynamics which are characteristic of the frozen state. In alkali oxides magnetic frustration has been observed in mixed valent Rb_4O_6 and Cs_4O_6. The glassy behavior in these materials was attributed to the three orthogonal anion orientations in the crystal structure, where it was assumed that the anions are in the form of distinct magnetic superoxide and non-magnetic peroxide [46]. Glassy behavior has also been studied in nonstoichiometric RbO_{2-x} where the random vacancy distribution leads to an inhomogeneous structure with probable nanodomains of different symmetry that lead to competing magnetic interactions of different sign [47]. It appears that the glassy state in alkali oxides can be very complex and more insight is needed for better understanding.

1.2.4 Magnetogyration and field induced magnetic transitions

The interesting phenomenon of magnetogyration is shown by alkali oxides and has been best studied in KO_2. This phenomenon involves the magnetoelastic coupling of localized magnetic moments to the cooperative rotation of oxygen dumbbells (O_2^-), which leads to a phase transition that minimizes the magnetic exchange energy. In KO_2 such a transition occurs on cooling at 7 K and the reverse transition can be induced by an applied magnetic field [10]. The phase diagram of KO_2 is shown in Fig. 1.9. This process can be comparable with magnetostriction in transition metal and rare-earth based compounds, which arises due to the interaction of the magnetic exchange with elastic constants of the crystaline materials, but the additional rotational degree of freedom of the superoxide anions adds more complexity.

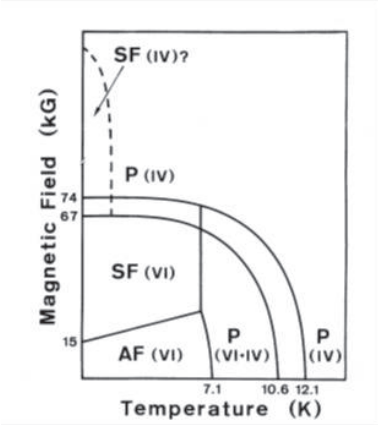

Figure. 1.9: Magnetic field - temperature phase diagram of KO_2 (taken from [10]).

1.3 Mixed Valency in Alkali Oxides

Mixed valency is a well-known and well-established feature of many classes of materials [8,48,49]. The term refers to a material (complex or crystal) that contains at least two chemically equivalent species with different formal oxidation states. In the past such systems containing a species in two different oxidation states were referred to by different, interchangeable names including the terms "mixed valence", "non-integral valence", "mixed oxidation", "oscillating valence" and "controlled valence". In order to avoid confusion the term "mixed valence" is generally used now. In organic molecules the concept of "resonance" is used to refer to degenerate or nearly degenerate electronic structures, and the state that results due to resonance will have properties different to those associated with the individual electronic structures. Similarly in mixed-valent inorganic molecules or crystals, the properties of the mixed valent state are often completely different to those of the same material if the relevant species had a single valence state. Inorganic mixed-valent systems can be categorized in terms of the interaction strength between two redox units, which can vary from low to high with

corresponding insulating to metallic behavior. This will be discussed in detail in Chapters 3 and 4. Mixed-valent compounds show potential for applications in molecular electronics, photocatalysis and solar technology [50-54]. It has been well demonstrated that there is often significant coupling between the electronic states in these compounds, and many mixed-valent systems exhibit electron transfer processes. Electron transfer phenomena in molecular-scale systems can also be induced by external stimuli, an aspect that has attracted considerable attention [52,55,56]. Reversible changes in charge distribution help to extend the applicability of certain mixed-valent systems to information storage technology and integrated molecular sized devices [50]. Mixed-valent systems based on transition metals have been widely studied and are generally well understood [48,57,58]. Among the best explored systems are the alkali earth doped rare-earth manganite and vanadate perovskites [31]. Anion-based mixed valent compounds are also known, mostly based on anions of metal-organic complexes. It is also possible to realize mixed-valent materials based on molecular oxygen. Such materials should have a non-integral filling of the π^* level (Fig. 1.1), which might allow a double-exchange-mediated ferromagnetic metallic state to be formed. If a ferromagnetic half-metallic state could be realized, these materials based on p–electrons would be of interest due to their expected higher degree of spin polarization (due to low spin-orbit coupling) and higher magnetic ordering temperatures (due to the more diffuse nature of p-orbitals) compared to transition-metal based systems [11,59]. Interestingly, an analogy can be drawn between mixed valent materials based on molecular oxygen ions and the well-known alkaline-earth-doped rare-earth manganites ($La_xAE_{1-x}MnO_3$) [31]. These manganites show a very rich phase diagram as a function of doping concentration and temperature, including ferromagnetic and antiferromagnetic, metallic and insulating states [60,61]. It remains to be seen whether mixed-valent alkali oxides show a similarly diverse range of properties, but a recent theoretical study on Rb_4O_6 suggested that the insulating, spin-glass phase observed at ambient pressure can be transformed to a ferromagnetic, half-metallic state under high pressure [62]

(Fig. 1.10).

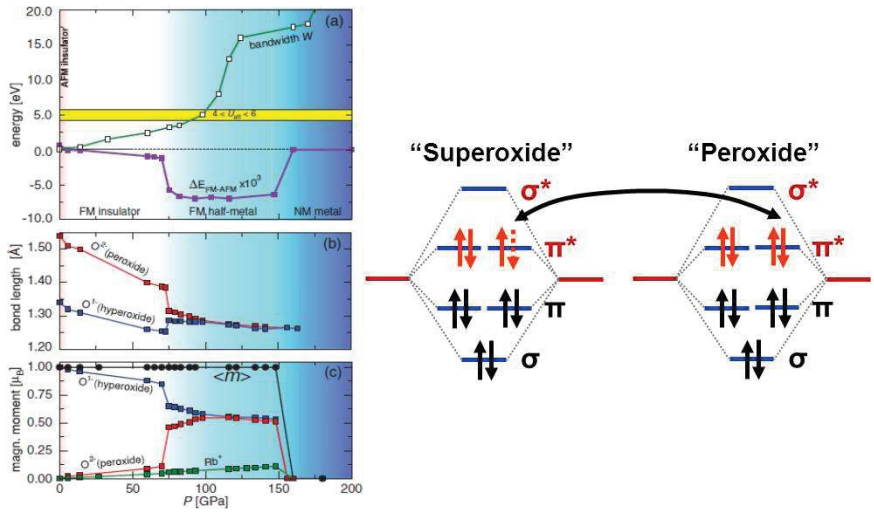

Figure 1.10: Calculated magnetic phase diagram of Rb_4O_6 under pressure (taken from [62])(Left).Schematic representation of double exchange in mixed valent alkali metal oxides (Right).

The only mixed valent alkali oxides that have been studied experimentally thus far are Rb_4O_6, Cs_4O_6, K_2BaO_6 and $RbO_{1.72}$ [47,64]. The magnetic properties of Rb_4O_6, Cs_4O_6 and $RbO_{1.72}$ are discussed briefly in the section on spin glasses above. Before the work presented in Chapters 3 and 4 of this thesis was carried out, only the synthesis of K_2BaO_6 had been reported and its physical properties were unknown. It is likely that many novel mixed valent alkali oxides can be synthesized. Particularly for the heavier alkali metals it is likely that the oxygen stoichiometry can be varied by thermal decomposition of the stoichiometric superoxide, giving nonstoichiometric AO_{2-x} phases. This is especially the case for stoichiometries between the sesquioxide ($AO_{1.5}$) and superoxide (AO_2) in the phase diagram, where it will be shown in this thesis that different crystal structures can be stabilized (Fig. 1.11). These phases, which generally have cubic structures at room temperature in which there is no anion rotational order, will be discussed in detail in Chapter 6.

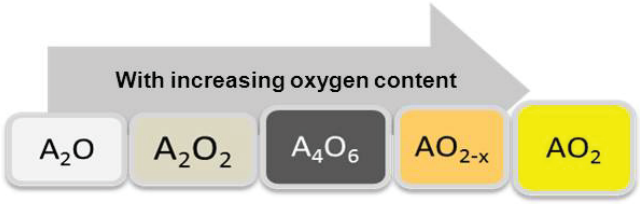

Figure 1.11: Known alkali oxide phases with increasing oxygen stoichiometry.

1.4 Electron transfer (charge transfer) phenomena

Mixed valency, a central theme of this thesis, often involves charge transfer phenomena. Perhaps the majority of studies on mixed valency have been performed on organic and organometallic materials, many of which are electronically very active [51] and show strong charge transfer effects. The transfer of electrons between neighboring ions or redox centers are broadly referred to as charge transfer (CT) transitions. It has been observed that in many cases CT transitions are excited by UV radiation, but absorption edges may extend into the visible region. Electron transfer between adjacent ions that momentarily changes the valence of the ions during the lifetime of the transition is referred to as an inter-valence transition (IVCT) [65]. The charge transfer in a material depends on the redox centers that are present in the system.In mixed valent systems the electron transfer process is often very dynamic and moreover involves coupling with the vibrational degrees of freedom. Significant charge transfer requires several criteria to be fulfilled. These include significant coupling between donor and acceptor states, a low degree of covalence, and in the case of localized electronic structure donor and acceptor orbitals with similar energies. Mixed valent systems are generally classified according to the Robin-Day model which identifies three

categories [48] based on the interaction strength between the neighboring redox units. For example, in Class 2 there is moderate interaction between the two redox units and hence possible electron transfer.

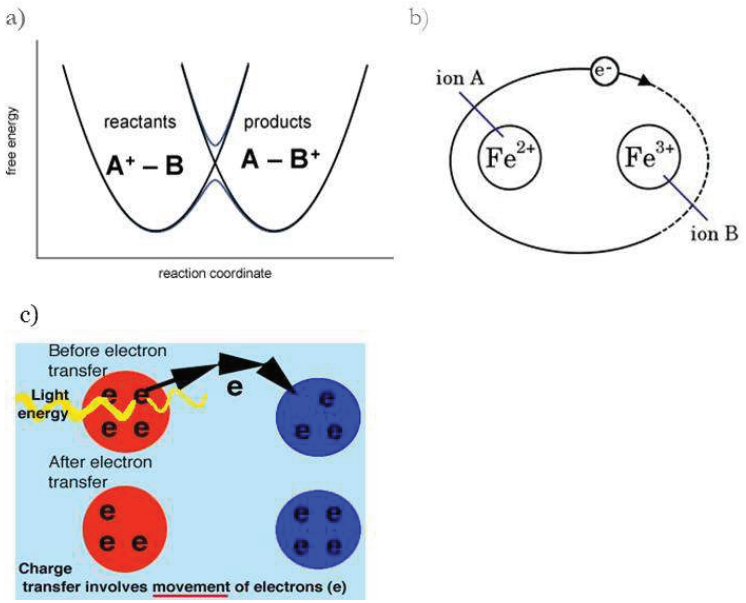

Figure 1.12: Schematic representation of charge transfer processes in mixed valent systems. a) Energy barrier for charge transfer from the A^{+}-B state to the A-B^{+} state for a Class 2 mixed valent system. b) Class 3 mixed valent system in which electrons are delocalized between two redox centers. c) Charge transfer induced by external stimulus (light) for a Class 2 system.

In Chapters 3 and 4 of this thesis it will be shown that $K_xBa_{1-x}O_2$ belongs to this category. The general picture is that electrons are vibrationally localized on one of the redox centers due to the presence of an activation energy barrier (ΔG). This barrier can be overcome by external optical or thermal stimuli to promote an inter-molecular electron or charge transfer process, and will be discussed in detail in Chapter 4. These concepts are illustrated in Fig. 1.12.

1.5 Motivation of this thesis

Despite the concepts of magnetism and mixed valence being well studied in transition metal and rare earth based compounds, they are much less explored for the 2p electrons of alkali metal oxides. Both the physics and chemistry of these materials need further study. In particular, the origin of magnetic exchange interactions in alkali oxides and their dependence on the crystal structure are poorly understood. In many of the alkali oxides the magnetic exchange strengths seem to be rather weak and the ordering temperatures are low. The application of external pressure or chemical pressure could be a way to increase the strength of these interactions. It is thus of particular interest to focus on the lighter alkali metal oxides, where the oxygen anions are brought into closer proximity to each other. This thesis attempts to address some of the open questions in these little known materials, especially concerning the potential of introducing mixed valency.

Outline

In Chapter 2 the synthesis of the alkali oxides and descriptions of the experimental techniques used in this thesis will be given. Chapter 3 addresses the synthesis of mixed valent $K_xBa_{1-x}O_2$ and its magnetic properties. This system is studied further in Chapter 4 using Raman spectroscopy backed up by density functional theory calculations. The observation of charge transfer effects is discussed in detail. The reader is advised that Chapters 3 and 4 are closely connected and are better read together. Chapter 5 focuses on possible mixed valency and polymorphism in the lightest known alkali superoxide, NaO_2. The synthesis, structural and magnetic properties are discussed. In Chapter 6 the introduction of non-stoichiometry and mixed valency in cesium and potassium oxides is discussed. Two novel phases CsO_{2-x} and KO_{2-x} are synthesized and characterized.

Bibliography

[1] Bibes, M.; Barthelemy, A. IEEE Transactions on Electron Devices 2007, 54, 1003.

[2] Ramesh, R.; Spaldin, N. A. Nature Materials 2007, 6, 21.

[3] Bielanski, A.; Haber, J. Catalysis Reviews - Science and Engineering 1979, 19, 1.

[4] Turner, J. Nature Materials 2008, 7, 770.

[5] Hesse, W.; Jansen, M.; Schnick, W. Progress in Solid State Chemistry 1989, 19, 47.

[6] Labhart, M.; Raoux, D.; Kanzig, W.; Bosch, M. A. Physical Review B 1979, 20, 53.

[7] Leach, M. R. The Chemogenesis web book, http://www.meta-synthesis.com/webbook.html.

[8] Chen, G. F.; Sakamoto, I.; Ohara, S.; Takami, T.; Ikuta, H.; Mizutani, U. Physical Review B 2004, 69, 054435.

[9] Fawcett, E. Physical Review B 1970, 2, 3887.

[10] Hayashi, K.; Hotai, K.; Hayakawa, M.; Ochiai, Y.; Matsuda, H.; Uedaira, S.; Aso, K. Journal of Magnetism and Magnetic Materials 1983, 38, 142.

[11] Volnianska, O.; Boguslawski, P. Journal of Physics: Condensed Matter 2010, 22, 073202.

[12] Ciric, L.; Djokic, D. M.; Jacimovic, J.; Sienkiewicz, A.; Magrez, A.; Forro, L.; Sljivancanin, Z.; Lotya, M.; Coleman, J. N. Physical Review B 2012, 85, 205437.

[13] Dutta, A. K. Physica 1958, 24, 343.

[14] Lin, C. Y.; Chen, S. C.; Wu, J. Y.; Lin, M. F. Journal of the Physical Society of Japan 2012, 81, 064719.

[15] Luhavaya, H. M.; Pavlov, M. V.; Ermilov, A. Y.; Stepanov, N. F. Russian Journal of Physical Chemistry A 2011, 86, 1261.

[16] Maghnaoui, A.; Boufelfel, A. Journal of Magnetism and Magnetic Materials 2012, 324, 2753.

[17] Wang, Y.; Zhao, Y.; Bao, T. J.; Li, X.; Su, Y. Q.; Duan, Y. X. Applied Surface Science 2012, 258, 8603.

[18] An, L. P.; Liu, N. H. New Carbon Materials 2012, 27, 181.

[19] Ding, K. H.; Zhu, Z. G.; Berakdar, J. Journal of Physics: Condensed Matter 2012, 24, 349501.

[20] Goncharenko, I. N.; Makarova, O. L.; Ulivi, L. Physical Review Letters 2004, 93, 055502.

[21] Gorelli, F. A.; Ulivi, L.; Santoro, M.; Bini, R. Physical Review B 2000, 62, R3604.

[22] Katsumata, K.; Kimura, S.; Staub, U.; Narumi, Y.; Tanaka, Y.; Shimomura, S.; Nakamura, T.; Lovesey, S. W.; Ishikawa, T.; Kitamura, H. Journal of Physics: Condensed Matter 2005, 17, L235.

[23] Gorelli, F. A.; Santoro, M.; Ulivi, L.; Hanfland, M. Physical Review B 2002, 65, 172106.

[24] Nozawa, K.; Shima, N.; Kenji, M. Journal of Physics: Condensed Matter 2008, 20, 335219.

[25] Shimizu, K.; Suhara, K.; Ikumo, M.; Eremets, M. I.; Amaya, K. Nature 1998, 393, 767.

[26] Bosch, M. A.; Lines, M. E.; Labhart, M. Physical Review Letters 1980, 45, 140.

[27] Kanzig, W.; Labhart, M. Journal de Physique Colloques 1976, 37, C7.

[28] Mahanti, S. D.; Khan, A. U. Solid State Communications 1976, 18, 159.

[29] Ylvisaker, E. R.; Singh, R. R. P.; Pickett, W. E. Physical Review B, 2010, 81, 180405R.

[30] Riyadi, S.; Zhang, B.; de Groot, R. A.; Caretta, A.; van Loosdrecht, P. H. M.; Palstra, T. T. M.; Blake, G. R. Physical Review Letters 2012, 108, 217206.

[31] Shivakumara, C.; Hegde, M. S.; Srinivasa, T.; Vasanthacharya, N. Y.; Subbanna, G. N.; Lalla, N. P. Journal of Materials Chemistry 2001, 11, 2572.

[32] Chu, Y. Y.; Wu, H. H.; Liu, S. C.; Lin, H.-H.; Matsuno, J.; Takagi, H.; Huang, J. H.; van den Brink, J.; Chen, C. T.; Huang, D. J. Applied Physics Letters 2012, 100, 112406.

[33] Teck-Yee, T.; Kennedy, B. J.; Qingdi, Z.; Ling, C. D.; Miller, W.; Howard, C. J.; Carpenter, M. A.; Knight, K. S. Physical Review B 2012, 85, 104107.

[34] Lines, M. E. Physical Review B 1981, 24, 5248.

[35] Zumsteg, A.; Ziegler, M.; Kanzig, W.; Bosch, M. Physics of Condensed Matter 1974, 17, 267.

[36] Stephanou, S. E.; Schechter, W. H.; Argersinger, W. J.; Kleinberg, J. Journal of the American Chemical Society 1949, 71, 1819.

[37] Kemeny, G.; Mahanti, S. D. Physical Review B 1979, 20, 2961.

[38] Mahanti, S. D.; Kemeny, G. Bulletin of the American Physical Society 1979, 24, 430.

[39] Smith, H. G.; Nicklow, R. M.; Raubenheimer, L. J; Wilkinson, M. K. Journal of Applied Physics 1966, 37, 1047.

[40] Kanamori, J.; Journal of Physics and Chemistry of Solids 1958, 10, 87.

[41] Lei, H.; Abeykoon, M.; Bozin, E. S.; Petrovic, C. Physical Review B 2012, 83, 180503.

[42] Taniguchi, T.; Munenaka, T.; Sato, H.; Journal of Physics: Conference Series 2009, 145, 012017.

[43] Cheikhrouhou, A.; Dupas, C.; Renard, J. P. Journal de Physique Lettres 1983, 44, 777.

[44] Phillips, J. C. Reports on Progress in Physics 1996, 59, 1133.

[45] Le Doussal, P.; Muller, M.; Wiese, K. J. Physical Review B 2012, 85, 214402.

[46] Winterlik, J.; Fecher, G. H.; Jenkins, C. A.; Medvedev, S.; Felser, C.; Kuebler, J.; Muehle, C.; Doll, K.; Jansen, M.; Palasyuk, T.; Trojan, I.; Eremets, M. I.; Emmerling, F. Physical Review B 2009, 79, 214.

[47] Riyadi, S.; Giriyapura, S.; de Groot, R. A.; Caretta, A.; van Loosdrecht, P. H. M.; Palstra, T. T. M.; Blake, G. R. Chemistry of Materials 2011, 23, 1578.

[48] Day, P.; Hush, N. S.; Clark, R. J. H. Philosophical Transactions of the Royal Society -Mathematical, Physical and Engineering Sciences 2008, 366, 5.

[49] Batlogg, B.; Ott, H. R.; Wachter, P. Physical Review Letters 1979, 42, 278.

[50] Heckmann, A.; Lambert, C. Angewandte Chemie International Edition 2012, 51, 326.

[51] Dong, T. Y.; Ke, T. J.; Peng, S. M.; Yeh, S. K. Inorganic Chemistry 1989, 28, 2103.

[52] Bosch-Serrano, C.; Clemente-Juan, J. M.; Coronado, E.; Gaita-Ariño, A.; Palii, A.; Tsukerblat, B. European Journal of Chemical Physics and Physical Chemistry 2012, 13, 2662.

[53] Wutkowski, A.; Niefind, F.; Naether, C.; Bensch, W. Zeitschrift fur Anorganische und Allgemeine Chemie 2011, 637, 2198.

[54] Hallier, K.; Hołynska, M.; Rouzieres, M.; Clerac, R.; Dehnen, S. Inorganic Chemistry 2012, 51, 3929.

[55] Brunschwig, B. S.; Creutz, C.; Sutin, N. Chemical Society Reviews 2002, 31, 168.

[56] Lancaster, K.; Odom, S. A.; Jones, S. C.; Thayumanavan, S.; Marder, S. R.; Bredas, J.-L.; Coropceanu, V.; Barlow, S. Journal of the American Chemical Society 2009, 131, 1717.

[57] Day, P. *Physics and Chemistry of Electrons and Ions in Condensed Matter*; Proceedings of the NATO Advanced Study Institute 1984.

[58] Lancaster, K.; Odom, S. A.; Jones, S. C.; Barlow, S.; Marder, S. R.; Coropceanu, V.; Bredas, J.-L. Abstracts of Papers of the American Chemical Society 2009, 237.

[59] Attema, J. J.; de Wijs, G. A.; Blake, G. R.; de Groot, R. A. Journal of the American Chemical Society 2005, 127, 16325.

[60] Helton, J. S.; Stone, M. B.; Shulyatev, D. A.; Mukovskii, Y. M.; Lynn, J. W. Physical Review B 2012, 85, 144401.

[61] Trinckauf, J.; Hanke, T.; Zabolotnyy, V.; Ritschel, T.; Apostu, M. O.; Suryanarayanan, R.; Revcolevschi, A.; Koepernik, K.; Kim, T. K.; von Zimmermann, M.; Borisenko, S. V.; Knupfer, M.; Buchner, B.; Geck, J. Physical Review Letters 2012, 108, 016403.

[62] Naghavi, S.; Chadov, S.; Felser, C.; Fecher, G. H.; Kuebler, J.; Doll, K.; Jansen, M. Physical Review B 2012, 85, 205125.

[63] Jansen, M.; Korber, N. Zeitschrift fur Anorganische und Allgemeine Chemie 1991, 598, 163.

[64] Seyb, E.; Kleinberg, J. Journal of the American Chemical Society 1951, 73, 2308.

[65] Mechouet, M.; Perruchot, C.; Maurel, F.; Aeiyach, S.; Bucher, C.; Chardon, S.; Jouini, M. Journal of Physical Chemistry A 2012, 116, 970.

Chapter 2

Synthesis and Characterization of Alkali Metal Oxides

As described in Chapter 1, alkali metal oxides are extremely interesting but practically challenging to work with due to their air sensitivity. Therefore, a specialized series of synthesis and characterization techniques have been used during this course of work. This chapter is dedicated to a discussion of the experimental methods and techniques involved and also of the principles behind the techniques.

2.1 Synthesis of alkali metal oxides and sample processing

Alkali oxides are known to be highly reactive, in particular towards moisture and CO_2 in the air, so it is essential to handle these materials in a controlled atmosphere. This requirement is based not only on science considerations but also on safety; alkali oxides can be highly flammable if directly exposed to air, so care must be taken at all times. Most of the sample handling and processing was carried out in a nitrogen filled glove box with a continuous circulation of nitrogen gas. The water content inside the glove box

was maintained at less than 0.5 ppm. The following sections discuss the synthesis techniques used for the alkali oxides studied in this thesis.

2.1.1 Synthesis of alkali oxides by solution method

It is well known that alkali metals dissolve in water-free liquid ammonia (NH_3) [1]. This proved to be a good solvent for many of the syntheses carried out in the current work. The reasons behind the choice of liquid NH_3 as a solvent are discussed in detail below.

2.1.1.1. Chemistry of ammonia as a solvent

Ammonia is a colorless gas with an intense odor above its boiling point of -33 C and is solid below -77 C (melting point). Ammonia is a trigonal–pyramidal molecule with the nitrogen atom at the middle of the trigonal pyramid (Fig. 2.1).

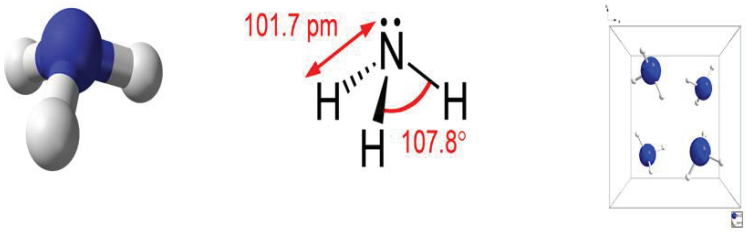

Figure 2.1: Molecular structure of ammonia and its unit cell structure in solid form.

As a solvent, ammonia shows properties that are comparable to water and other polar solvents with respect to the dissociation of electrolytes. However, when it dissolves in water ammonia acts as a base as shown in the reaction below.

$$NH_3(aq) + H_2O(l) \rightleftharpoons NH_4^+(aq) + OH^-(aq)$$

The equilibrium lies to the left in this reaction, thus NH_3 is considered to be a weak base. The equilibrium constant is shown below.

$$K_b = \frac{[NH_4^+][OH^-]}{[NH_3]} = 1.8 \times 10^{-5} \text{ at } 25^\circ C$$

The ammonium cation acts as a weak acid in aqueous solution, because it dissociates to NH_3 and a proton.

$$NH_4^+(aq) \rightleftharpoons NH_3(aq) + H^+(aq)$$

The most relevant property of liquid ammonia in the current work is its sufficient polarity to dissolve many salts of monovalent and divalent cations such as alkali and alkaline earth metals, as well as some transition metals. Secondly, its high basicity as a solvent suppresses the protonation and subsequent instantaneous decomposition of a number of labile anions such as superoxide. When alkali metals are dissolved in liquid ammonia, a dark blue solution appears due to the formation of solvated electrons. Metal-ammonia solutions exhibit high electrical conductivity that is proportional to the concentration of the metal solution. Since alkali-ammonium solutions are known for their electrolytic nature, many studies have been conducted to study their electronic properties [2-5].

2.1.1.2. Working setup for synthesis

In order to carry out the synthesis of alkali oxides in a controlled manner, a vacuum line was specially designed, a schematic picture of which is shown in Fig. 2.2 and a photo of which is shown in Fig. 2.3. All compounds discussed in this thesis were synthesized using this setup.

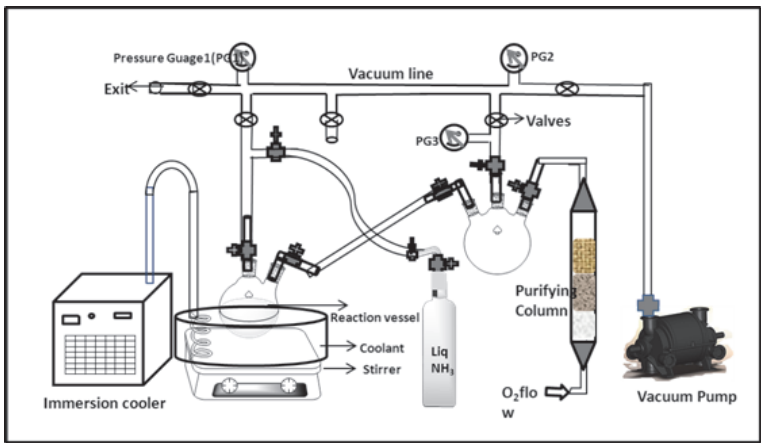

Figure 2.2: Schematic diagram of the vacuum line used for synthesizing alkali metal oxides in this thesis.

The vacuum line in Fig. 2.2 was connected to a vacuum pump that allowed evacuation to a pressure of 10^{-4} mbar. The vacuum line was separated from the pump by a liquid nitrogen trap to avoid corrosion and breakdown of the pump. The reactions were carried out in a 250 ml two-necked borosilicate round bottom flask, labeled as the reaction vessel in the diagram. This flask was connected through one neck to the vacuum line or liquid ammonia supply and through the other to the vacuum line or external O_2 supply via a purification column. In order make the supplied O_2 water free, a drying column consisting of layers of activated alumina (Al_2O_3), sodium peroxide (Na_2O_2) and molecular sieves was used.

There are three pressure gauges (PG) in this setup, which were used at different stages of the synthesis for different purposes. PG1 was used to have control over the flow of NH_3 during condensation in the reaction vessel, whereas PG2 and PG3 were used to maintain the desired oxygen partial pressure during the oxidation of metal-ammonia solutions. Connections between different parts of the vacuum line setup were controlled by a series of valves. Most of the reactions were carried at low temperature, which was achieved using a closed cycle Thermo Scientific Haake EK90 immersion

cooler, where absolute ethanol was used as the coolant in a flat cylindrical container into which the reaction vessel was immersed. The minimum achievable temperature is -90 C, but most experiments carried out in this thesis used temperatures from -50 C to -75 C.

Figure 2.3: Picture of complete set up used for the synthesis of alkali oxides.

2.1.1.3. Oxidation of alkali metal solutions

Ampoules containing alkali metals (purity 99.75%, obtained from Alfa Aesar) were brought into a nitrogen-filled glove box and broken at one end. Pieces of the soft metal were transferred using a spatula to a 250ml two-necked round bottom flask that had been pre-dried in an oven at 200 C. The valves on both necks of the flask were closed, allowing it to be transferred out of the glove box. Both necks were connected to the vacuum line at the positions of the NH_3 and O_2 inlets. Before beginning the condensation of liquid NH_3 in the reaction vessel, it was evacuated to remove the N_2 gas from the glove box. The temperature of the coolant bath was reduced to a sufficiently low temperature (<-33 C) and liquid NH_3 was then condensed in the reaction vessel by closing the valve to the vacuum line. A volume of 100-150 ml of liquid ammonia was condensed. The valve to the oxygen supply (99.99% purity) was then opened and oxygen was passed through the drying column and into the reaction vessel for oxidation of the alkali metal. Before passing into the reaction vessel, the column was flushed 2-3

times with oxygen to make sure that it was dry enough. The initial partial pressure of oxygen supplied to the reaction vessel was varied between 550-750 mbar. The fall in oxygen pressure with time was monitored in order to observe the amount of oxygen absorbed during oxidation. After ∼1h the static oxygen pressure was increased and the procedure repeated two or three times until no more oxygen was absorbed. The solution was constantly stirred during oxidation using a magnetic stirrer. The reaction vessel in the cooling bath is shown in Fig. 2.4. When liquid NH_3 was condensed into the vessel containing the alkali metal, a dark blue solution was formed due to solvated electrons. Exposure to oxygen led to a colorless solution, followed by a white color and finally a thick yellow precipitate, which indicated formation of the alkali superoxide. The intensity of the color changes on going down the alkali metal group from pale greenish yellow to orange yellow. Once the yellow precipitate had formed, the liquid ammonia was removed from the solution by opening the valve to the vacuum line. Due to the partial solubility of some of the alkali oxides (superoxides/sesquioxides) in liquid ammonia, stirring was stopped during the evaporation step. Once evaporation had been completed, the dry powder in the reaction vessel was carefully transferred to the glove box for storage, further analysis and characterization.

2.1.1.4. Oxidation of alkali metal salts

Some of the alkali oxides studied in this thesis were synthesized from metal salts in ammonia solution. In these cases an exchange reaction between an alkaline earth metal nitrate ($AE(NO_3)_2$) and an alkali superoxide (AO_2) in liquid ammonia gave a dark precipitate [6], which was oxidized for some time to complete the reaction. After completion of the reaction the procedure used was similar to that for the metal solution route described above. This procedure will be discussed in detail in Chapter 3.

Figure 2.4: Reaction vessel in coolant bath, set up for oxidation.

2.1.1.5. Possible side reaction and its control

A side reaction involving superoxide anions with ammonia always takes place, which leads to the formation of alkali hydroxide (anhydrous or hydrated) and influences the purity of the alkali oxide samples obtained. The extent to which this side reaction takes place is largely determined by the solubility of the alkali superoxide being synthesized, which increases with decreasing cationic radius. The relatively high solubility of sodium and lithium superoxides (the existence of the latter is still under debate) implies that the side reaction is most significant in attempts to synthesize these materials. The side reaction is shown by the reactions below [7].

Ammonolysis of superoxides:

$$O_2^- + 2NH_3 \longrightarrow 2OH^- + 2\,NH_2^-$$

Molecular O_2 supplied to the reaction vessel can react with the amide ions formed as follows:

$$2\,NH_2^- + 3/2O_2 \longrightarrow OH^- + NO_2^- + NH_3$$

This side reaction occurs generally for all alkali oxides containing the superoxide anion synthesized by the solution route and will be discussed further in the individual chapters that follow. Certain precautions can be

taken to suppress the side reaction. Firstly, in order to minimize the formation of hydrated alkali hydroxides, surface moisture on the glassware was removed by heating all glass vessels overnight at 200 C before connecting to the vacuum line. Secondly, after oxidation the evaporation rate of the solvent was increased by raising the reaction vessel temperature by taking it outside the coolant bath. Stirring was avoided during this step in order to minimize solubility of the superoxide product. Thirdly, the minimum volume of liquid NH_3 necessary to dissolve the alkali metal was condensed. Since it is difficult to control the amount of liquid NH_3 condensed to precisely the minimum volume needed, it is was found to be better to increase the amount of metal in the vessel to obtain a saturated solution. Lastly and importantly, a maximum of 750 mbar oxygen pressure was applied in order to carry out the oxidation of the metal solution as quickly as possible. The oxidation was stopped immediately after the yellow color indicated completion of the reaction. The solubility of the superoxide anions that are formed can also be avoided by using a solvent mixture of methylamine and NH_3 with just enough NH_3 to dissolve the alkali metal; superoxide is much less soluble in methylamine. Collectively, these procedures help to suppress the side reaction and the proportion of hydroxide impurities can be kept low.

2.1.2 Controlled thermal decomposition

The section above discusses the synthesis of alkali superoxides in stoichiometric form (AO_2). However, alkali oxides can in some cases also be stabilized with lower, non-stoichiometric oxygen content (AO_{2-x}). Such compositions can be synthesized by direct oxidation of the solid alkali metal, but samples with poor homogeneity result. A better route is to remove oxygen from AO_2 by heating in an inert atmosphere. This thermal decomposition can be carried in two different ways, one by continuous thermal decomposition of a large amount of AO_2 in an open system and the other by more controlled thermal decomposition of a smaller amount of AO_2 in

a sealed tube. The former route was used to prepare RbO_{2-x} by heating at 150 C for 24h using a tube furnace attached to a vacuum pump [8]. In this thesis the non-stoichiometric samples that are studied were prepared by heating AO_2 contained in a sealed glass tube. Homogeneous products were obtained after regrinding, resealing and reheating 2-3 times. The tube furnace and the box furnace used in these two routes are shown in Fig. 2.5. The temperature required to decompose AO_2 and form an oxygen-deficient cubic phase (see Chapter 6) decreased down the alkali metal group of the periodic table, as shown in Table 2.1.

Figure 2.5: Tube furnace, box furnace and sealed tube used in thermal decomposition of AO_2.

Alkali Superoxide	**Cubic AO_{2-x} formation Temperature**
NaO_2	Unknown
KO_2	>340 ^{0}C
RbO_2	>150 ^{0}C
CsO_2	>105 ^{0}C

Table 2.1: Temperatures required for decomposition of AO_2 to cubic AO_{2-x} for different alkali metals.

2.2 Structural Characterization

2.2.1 X-Ray Powder Diffraction (XRPD)

X-ray diffraction can be used as a fingerprint technique for identifying known crystalline solids, or for providing highly detailed structural infor-

mation about atomic and molecular arrangements and chemical bonding. Diffraction techniques can be used on different types of crystalline samples including powders, single crystals and thin films. The working principle of diffraction techniques varies with the requirements. The samples investigated in this thesis are in powder (polycrystalline) form, thus the working principles of XRPD are described briefly below. Laboratory X-ray beams are often produced in a sealed X-ray tube, inside which high-energy electrons collide with a metal target. Often a tungsten filament is used as the electron source. The electrons are accelerated towards a metal target anode using a high voltage of ∼40kV. The metal target depends on the X-ray wavelength desired. This thesis includes data measured using Mo and Cu targets (X-ray wavelengths of 0.7094 Å (Mo Kα_1) and 1.5406 Å (Cu Kα_1). A germanium or quartz monochromator was used to select the Kα_1 line in the incident beam. In the selection of the source, the absorption of the elements in the samples should be taken into account. For example, the Rb K-edge is close to the wavelength of Mo Kα radiation and thus samples containing Rb are highly absorbing towards a Mo source, and a Cu source is a better choice to obtain nice diffraction patterns with good signal to noise ratio. The X-ray diffraction data of the alkali oxides presented in this thesis were collected using a Huber G670 Guinier camera system operating with Cu Kα radiation, a photo of which is shown in Fig 2.6. This system utilizes flat plate Guinier (transmission) geometry and a linear imaging plate detector covering two-theta angles between 0° and 100°. After exposure for the desired time (a few minutes to a few hours), the imaging plate is scanned using a laser and converted to a one-dimensional diffraction pattern. The advantage of using an imaging plate compared to a point detector is that data covering the entire angular range can be obtained on a much shorter time scale. The samples were mounted in a nitrogen-filled glove box by sandwiching the powder between two sheets of Mylar film that were clamped in place using a metal ring. The sample chamber was evacuated to ∼0.1 mbar throughout the measurements and no signs of decomposition were seen. Temperature control was achieved using a closed-cycle refriger-

ator. With this setup temperatures down to 17 K could be achieved. The temperature at the sample holder was monitored using a Pt100 thermocouple. The Huber G670 system is also able to measure at high temperatures using a resistive heater. Here the samples were mounted in glass /quartz capillaries that were sealed at one end to avoid moisture contamination.

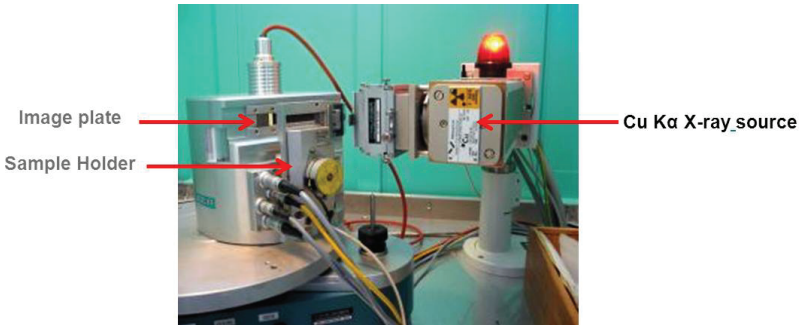

Figure 2.6: Guinier configuration used in Huber G670 diffractometer.

The data obtained were analyzed using the GSAS (General Structure Analysis System) software [9,10]. For the best quality data suitable for Rietveld refinement, data were generally acquired for between 60-120 min. In some instances where the X-ray absorption was strong, it was necessary to expose the imaging plate for 12-15 h. The system of sample mounting and the transmission geometry of the Huber diffractometer (sample sandwiched between Mylar films or in a sealed capillary) is advantageous when working with air sensitive compounds.

2.2.2 Neutron Diffraction

The principles of neutron diffraction are similar to X-ray diffraction but with some important differences. As neutrons do not bear any charge, they can penetrate deeper into the material than X-rays. Neutrons scatter from the nuclei of atoms and thus the scattered intensity does not fall off with increasing diffraction angle like in X-ray diffraction. Furthermore, the neutron scattering factors of the elements show no systematic trend

with atomic number, thus many light atoms like hydrogen scatter neutrons strongly. Since neutrons have a spin, they interact with magnetic moments in solids and can be used to probe both long and short range magnetic ordering, in other words to determine the magnetic structure. Neutrons can also be used to study dynamics in solids such as phonons and magnons which are not easily accessible by X-ray scattering. In this thesis neutron diffraction was carried out on the GEM (General Materials) diffractometer at ISIS, Rutherford Appleton Laboratory, United Kingdom. At ISIS a white beam of neutrons is produced by a spallation source and slowed down by a moderator to speeds useful for diffraction. The GEM detector array covers a total area of 7.27 m^2 at scattering angles ranging from 1.2 to 171.4 degrees grouped in six different banks. The time of flight of the neutrons from the source to the detector, which is a function of the lattice d-spacing, is measured. Samples of roughly 0.75 g were placed in 6 mm diameter vanadium cans inside the glove box and sealed using a soft indium ring and screws. The data obtained were again analyzed using the GSAS software.

2.3 Physical and Chemical Property Measurements

2.3.1 Magnetic property measurements (MPMS)

The magnetic properties of the samples studied in this thesis were probed using a Quantum Design MPMS XL-7 SQUID magnetometer. The working temperature of the MPMS varies from 2 K to 350 K and applied fields of +7 T to -7 T can be used. A picture of the apparatus is shown in Fig. 2.7. A SQUID (superconducting quantum interference device) is used to measure the magnetic dipole moment of a sample as a function of temperature and field. There are three main components to the MPMS: a superconducting magnet, second-order gradiometer pick-up coils to detect the magnetic field of the sample, and a cryostat and sample heating system connected to a temperature controller. The pickup coils are inductively coupled to the SQUID sensor by a superconducting transformer. To create an alter-

nating magnetic flux from the pickup coils, the sample stick is moved up and down by a motor to pass the sample through the coils. The alternating flux signal from the SQUID is detected in terms of an alternating voltage which is further amplified and processed to give the magnetic moment in units of emu. The quantity of sample should occupy the minimum volume possible to obtain a good signal. Moments as low as 10^{-7} emu can be measured in the MPMS. The alkali oxide samples measured in this thesis were in polycrystalline (powder) form. Samples of mass 15-35 mg were placed in 5 mm NMR tubes inside the glove box. The nitrogen-filled NMR tube was connected to a short length of flexible hose which was fitted tightly over a glass quick-fit connector equipped with a valve. This allowed the NMR tube to be isolated from the air while transferring to a vacuum line. Once connected to the vacuum line, the valve was opened and the tube was evacuated by pumping while being sealed using a flame. The sealed tube was fixed tightly inside a plastic straw. The straw was mounted on the end of the MPMS sample stick using thermal conductive tape, and the whole stick with sample was inserted slowly into the MPMS sample chamber after flushing the venting chamber 2-3 times. The sample was centered at 25 K. The magnetic susceptibility of the samples was measured as a function of temperature in zero-field-cooled (ZFC) and field-cooled (FC) mode. For ZFC mode, the sample was cooled down to 2 K in zero applied field, with a short time interval at 25 K where the sample was centered. A magnetic field was then applied and the sample was measured on warming from 2 K to 300 K. In FC mode the sample was cooled down to 2 K in an applied field and measured on warming using the same applied field. Measurements of magnetization versus applied field were also performed by cycling the field between +7 T and -7 T at constant temperature. In order to understand the spin dynamics in the samples, thermoremanent magnetization measurements (TRM) were carried out by cooling the sample down to low temperature in zero field, waiting for some fixed time (T_w) and then measuring the sample as a function of time after applying a small magnetic field. The T_w was varied and the data were fitted using exponential and/or

power law functions.

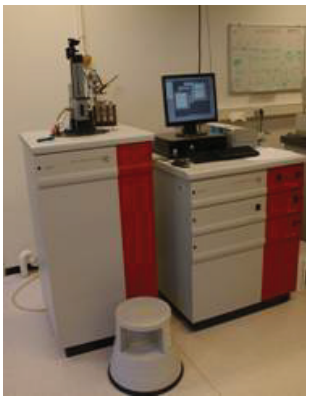

Figure 2.7: Picture of Quantum Design MPMS XL 7.

2.3.2 Capacitance measurements

Capacitance measurements were performed on some of the samples in this thesis using a capacitance bridge (Andeen-Hagerling 2500A) at a frequency of 1 kHz, and using an Agilent LCR meter 4284A for variable frequencies between 20 Hz and 1 MHz. Due to the moisture sensitivity of the samples a sample holder was specially designed and constructed using Teflon containers (Fig. 2.8). Two Teflon containers with screw threads were fabricated and attached to gold coated copper electrode plates with an extension on both ends. The sample was placed in one of the Teflon containers inside the glove box, sandwiched between the two copper plates and the second container was then screwed tight to the first. The holders were sealed by placing Double Bubble epoxy resin in the closings. This sample holder was attached to a home-made probe containing four triax connectors on the flange, connected to stainless steel coaxial wires below the flange. The inner part of the triax connector was connected to the bottom of the sample holder and the shields of the triax connectors were connected to a copper block on the bottom of the sample holder. The probe stick with the sample was then placed inside a Quantum Design PPMS (Physical Property

Measurement System) model 6000 cryostat (Fig. 2.8), which can operate between temperatures of 1.8 K and 375 K, and in magnetic fields of -9 T to 9 T. The measurements were controlled using a Labview program. Capacitance is the ability of a sample to store electrical charge and can be expressed as C=Q/V, where Q is the electrical charge and V is the applied voltage.The Farad is the SI unit of capacitance. Parallel geometry was used such that $C=\varepsilon_0\varepsilon(A/d)$ where ε_0 is the permittivity of vacuum (8.85×10^{-12} F/m), ε is the dielectric constant, A is the area of the capacitor plates and d is the distance between the conductive plates, in other words the thickness of the sample.

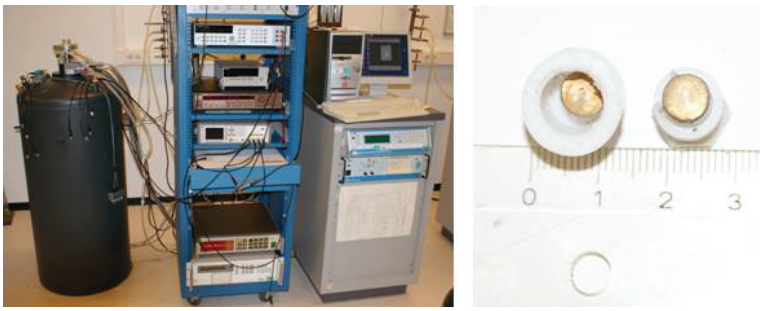

Figure 2.8: Picture of Quantum Design PPMS and specially made Teflon parallel plate sample holder for capacitance measurements.

2.3.3 Thermal Analysis: (Differential Scanning Calorimetry (DSC) – Thermo-Gravimetric Analysis (TGA))

In combination with structural analysis by X-ray diffraction, thermal analysis proved to be an effective tool in identifying phase transitions in the alkali oxides. In DSC the difference between heat flow to the sample and to a reference (an inert material such as alumina (Al_2O_3)) at the same temperature is recorded as a function of temperature. Since DSC is performed at constant pressure, the heat flow is equivalent to changes in enthalpy: $(dq/dt)_p = (dH/dt)$ where $\Delta(dH/dt) = (dH/dt)_{sample} - (dH/dt)_{reference}$. This quantity can be negative or positive depending on whether the transition being

probed is endothermic or exothermic in nature. In TGA the change in weight of the sample is measured as a function of temperature with respect to the reference weight, which is constant with respect to time and temperature. In this thesis data measured using two modes of thermal analysis will be presented, one above room temperature and the other below room temperature. High-temperature DSC-TGA measurements were performed using a SDT 2960 (TA Instruments) machine. As the air sensitivity of the alkali oxides is a main concern, the sample was placed in an alumina crucible that could be loosely closed with a lid (shown in Fig. 2.9), all the handling being done in the glove box. The crucible was transported to the DSC-TGA apparatus inside a closed vessel before being placed quickly inside the sample chamber of the apparatus. For probing the structural transitions of alkali oxides, argon gas was flowed during heating, whereas for the estimation of oxygen content pure and dry oxygen was supplied during heating. Low temperature DSC was carried out using a SDTQ1000 (TA Instruments), which has a working temperature range of -70 C to 120 C. Here the sample was placed inside a pair of platinum pans which were sealed using a hand press inside the glove box (Fig. 2.9). The baseline was corrected for by running a scan with empty pans.

Figure 2.9: Left: alumina crucible with a lid used for high temperature DSC-TGA. Right: open and closed pans used for low temperature DSC.

2.3.4 Raman Spectroscopic analysis

Raman spectroscopy was used as a main tool in characterizing the nature of the molecular oxygen ions in the samples. The frequencies of the O-O

stretching modes are characteristic of the valence state of the anions. As the samples are air sensitive, they were sealed in evacuated 5 mm Pyrex NMR tubes using the same procedure as for the magnetic measurements. Raman spectra were measured in the backscattering configuration using a liquid nitrogen-cooled charged coupled device (CCD) connected to a three-grating micro-Raman spectrometer (T64000 Jobin Yvon). The samples were excited using a 532 nm He-Ne laser focused to an area of 50 μm^2; in some instances a 635 nm red laser was used. The frequency resolution of this setup was $\pm 1 \mu m$. Temperature control down to 7 K was achieved using a cold finger attached to the sample chamber. Samples for low temperature measurements were prepared by pressing powder onto a copper plate (Fig. 2.10) inside the glove box. The copper plate was mounted on the cold finger using airtight stainless steel (SS) couplings. This setup was also used for scans in vacuum, where the pressure was varied between 10^{-5} mbar and 1 bar by pumping and supplying dry argon, nitrogen or oxygen gas through the gas inlet of the cold finger.

Fig 2.10: Copper sample holder and Oxford cold finger used for temperature and pressure (vacuum) dependent Raman spectroscopy.

Bibliography

[1] Shakhashiri, P. http://www.scifun.org (2008).

[2] Arnold, E.; Patterson, J. A. Journal of Chemical Physics 1964, 41, 3089.

[3] Kraus, C. A. Journal of the American Chemical Society 1908, 30, 1323.

[4] Kraus, C. A. Journal of the American Chemical Society 1921, 43, 749.

[5] Ogg, R. A.; Leighton, P. A.; Bergstrom, F. W. Journal of the American Chemical Society 1933, 55, 1754.

[6] Seyb, E.; Kleinberg, J. Journal of the American Chemical Society 1951, 73, 2308.

[7] Watt, G. W. Chemical Reviews 1950, 46, 289.

[8] Riyadi, S.; Giriyapura, S.; de Groot, R. A.; Caretta, A.; van Loosdrecht, P. H. M.; Palstra, T. T. M.; Blake, G. R. Chemistry of Materials 2011, 23, 1578.

[9] Toby, B. H. Journal of Applied Crystallography 2001, 34, 210.

[10] Larson A.C.; von Dreele, R. B. Los Alamos National Laboratory Report LAUR 2004, 867, 48.

Chapter 3

Anionogenic Magnetism in Mixed Valent $K_xBa_{1-x}O_2$

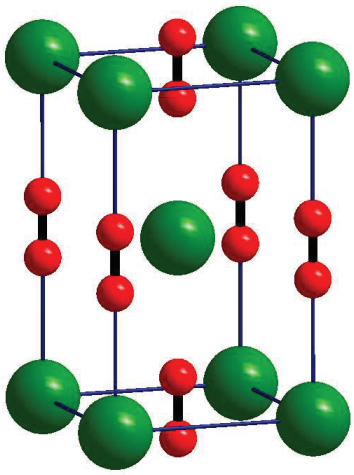

3.1 Introduction

As discussed in Chapter 1 and earlier reports, ionic compounds containing molecular oxygen species like ozonides, superoxides and peroxides have been relatively little explored [1]. Ionic salts containing nominal mixtures of superoxide and peroxide can be considered as mixed-valent compounds and are particularly interesting for further studies. Due to the electronic transfer processes often exhibited by mixed valent compounds, they show potential for applications in molecular electronics, photo-catalysis and solar energy [2-4]. Interestingly, electron transfer phenomena induced by external stimuli such as light, temperature or pressure in molecular-scale systems have attracted considerable attention. Reversible changes in electronic charge distribution in mixed-valent materials like $(PY_5Me_2)_2V_2$(m-5,6-dimethylbenzimidazolate)] $(PF_6)_4$ help to extend their applicability in information storage and integrated molecular-sized devices [3].

In the case of ionic mixed-valent dioxygen-based compounds, an analogy can be drawn with the well-known "colossal magnetoresistance" (CMR) manganites $RE_{1-x}AE_xMnO_3$ (RE = Rare earth, AE = alkaline earth). These compounds contain manganese in both the Mn(III) and Mn(IV) oxidation states and exhibit a rich phase diagram with AE doping that includes electronically insulating and conducting phases, and both antiferromagnetic (AFM) and ferromagnetic (FM) ordering [5-15]. In the FM metallic phase, the magnetism is due to double exchange that involves electrons hopping between the e_g orbitals of Mn(III) and Mn(IV), mediated by the oxide (O_2^-) anions. Similarly, we can expect that double exchange will occur in materials containing dioxygen anions of different valence states, where electrons hop directly between the π^* molecular orbitals of neighboring anions. One approach towards obtaining mixed-valent dioxygen systems is to vary the oxygen content in the A_2O – AO_2 phase diagram; attempts to synthesize new materials by this approach are discussed in detail in Chapter 6. The mixed-valent phases that have been identified and characterized thus far are $RbO_{1.5}$, $CsO_{1.5}$ and $RbO_{1.72}$ [16,17]. All three compounds are insula-

tors despite $RbO_{1.5}$ and $CsO_{1.5}$ being black in color, hinting at a different electronic structure to A_2O and AO_2, which are always white or pale yellow. All three compounds exhibit varying degrees of spin-glass-like behavior at low temperature, with AFM interactions dominant. In $RbO_{1.72}$ FM interactions are also present, probably within small clusters [16]. An alternative approach to mixed valence is suggested by the 1953 paper of Seyb and Kleinberg [18], which reports on the synthesis of a brown polycrystalline material with composition K_2BaO_6. Although not studied further, this compound should also have non-integral filling of the π^* orbitals, induced by the incorporation of monovalent K^+ and divalent Ba^{2+} cations. In this chapter the synthesis, structural and magnetic properties of the solid solution series $K_xBa_{1-x}O_2$ with $x < 0.45$ are described. In Chapter 4 Raman spectroscopy is used to show that the dioxygen anions in these compounds have significant mixed-valent character, in which the occupation of the π^* level on a given atomic site is dynamical.

3.2 Experimental

3.2.1 Synthesis and characterization

It is challenging to synthesize pure samples of mixed-valent alkali oxides due to their high reactivity. One possible approach is the solution method in which alkali metals or metal salts are dissolved in liquid NH_3 in a controlled atmosphere. This is the most suitable method for synthesizing $K_xBa_{1-x}O_2$. An exchange reaction between stoichiometric amounts of $Ba(NO_3)_2$ (Alfa Aesar, 95.5%) and KO_2 (Sigma Aldrich, 99.99%) in ∼100 ml liquid NH_3 gave a brown precipitate of $K_xBa_{1-x}O_2$ with KNO_3 formed as a by-product (see Reaction 3.1). The reaction was carried out in a round bottom flask, as shown in Fig. 3.1a. Because both KO_2 and $K_xBa_{1-x}O_2$ are very sensitive to moisture, it is important that the glassware is dried thoroughly before the start of synthesis. The reaction temperature was held constant at a value between -40 C and -60 C using an immersion cooler in an ethanol bath, and

dry oxygen gas (99.999%) was continually supplied, maintaining a partial pressure of 550 mm Hg. The reaction mixture was then transferred to a U-shaped glass vessel that contained a filter in one arm and was attached to a vacuum line at both ends, as shown in Fig. 3.1b. The soluble KNO_3 by-product was removed by washing three to four times with excess liquid NH_3, which was pulled through the filter by applying a vacuum. The moisture- and CO_2-sensitive products were then sealed in pyrex NMR tubes under dry nitrogen atmosphere for storage. This process is complicated by a side reaction of KO_2 with the NH_3 solvent (see Reaction 3.2), the rate of which appears to be dependent on the synthesis temperature and time. Here the synthesis temperature should be as low as possible and the reaction time should be made as short as possible to minimize the occurrence of the side reaction; it was varied up to 12 h and the optimum reaction time was found to be ∼30 min. However, between 10% and 13% of $KOH.H_2O$ impurity was always present in the samples. The side reaction also limited the proportion of K^+ that could be incorporated in the product. Adding an excess of KO_2 resulted in unreacted KO_2 in the product. The optimum ratio of starting materials for maximizing the value of x in $K_xBa_{1-x}O_2$ while minimizing the occurrence of the side reaction was 3.5 moles of KO_2 to 1 mole of $Ba(NO_3)_2$. Solid solutions were prepared with $0.22 < x < 0.42$, where the highest K-content was obtained at temperatures close to the boiling point of NH_3. However, it was not possible to prepare a sample with the stoichiometry of K_2BaO_6 reported by Seyb and Kleinberg [18]. The synthesis of $K_xBa_{1-x}O_2$ was also tried by an analogous procedure in methylamine solvent instead of liquid ammonia, but only dilute samples of up to $x = 0.25$ were obtained. The composition is likely influenced by the lower solubility of the salts relative to liquid NH_3.

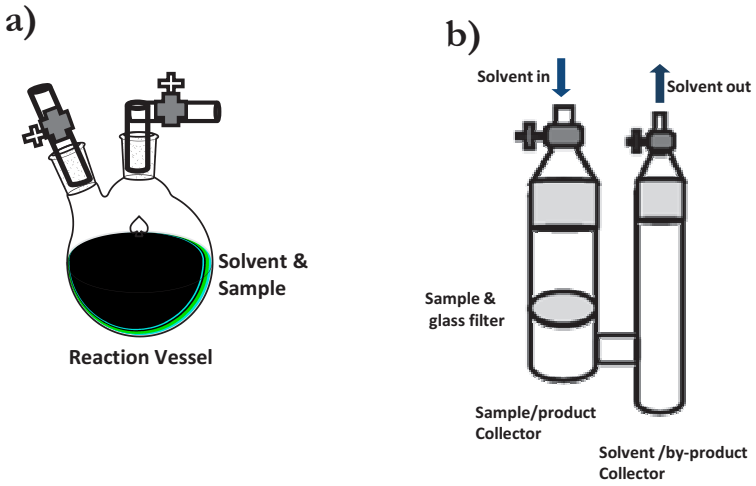

Figure 3.1: Apparatus involved in synthesis of solid solutions $K_xBa_{1-x}O_2$. a) Reaction vessel with valves. b) Washing vessel for separation of by-product KNO_3 from product $K_xBa_{1-x}O_2$.

Reaction 3.1:

$$(2+x)KO_2 + Ba(NO_3)_2 \xrightarrow[\text{Liq } NH_3]{O_2} K_xBa_{1-x}(O_2^-)_x\,(O_2^{2-})_{1-x} + (3.5-x)\,KNO_3$$

Reaction 3.2:

$$K^+O_2^- + 2NH_3 \xrightarrow{\text{Liq } NH_3} KNH_2 + KOH$$

$$2KNH_2 + 3KNO_3 \longrightarrow NH_3 + 4KN0_2 + KOH$$

$$KNH_2 + KNO_2 \longrightarrow N_2 + 2KOH$$

$$3KNH_2 + 3KN0_3 \longrightarrow NH_3 + 3KNO_2 + 3KOH + N_2$$

The overall K:Ba ratio in the samples (including impurities) was determined using inductively coupled plasma (ICP) analysis combined with optical emission spectrometry. The solutions for IPC were prepared by dissolving the compounds in 0.01M aqua regia solution. The ratio of K:Ba in

the $K_xBa_{1-x}O_2$ solid solutions was then calculated by taking into account the percentages of $KOH.H_2O$ and unreacted KO_2 impurities in the samples estimated using X-ray powder diffraction (XRD). Due to the uncertainty in the phase fractions determined by XRD, the K:Ba ratios of the solid solutions have typical experimental uncertainties of a few percent. The results presented in Chapters 3 and 4 were obtained from five samples with compositions x = 0.224, 0.228, 0.269, 0.325, and 0.412.

Laboratory XRD data were collected using a Huber G670 diffractometer as described in Chapter 2. Neutron diffraction data were collected on the GEM diffractometer at the ISIS facility, also described in Chapter 2. Data were collected down to 5 K using a standard helium-cooled cryostat. Structural refinements were carried out using the GSAS [19-20] software suite for all the X-ray and neutron diffraction data. Magnetization data and Raman spectra were collected as described in Chapter 2.

3.3 Results

3.3.1 X-ray and neutron diffraction

Based on the X-ray and neutron powder diffraction data, $K_xBa_{1-x}O_2$ with $0.22 < x < 0.42$ adopts the body-centered tetragonal CaC_2 structure type with space group I4/mmm (Fig. 3.3), which is isostructural with the end members of the series BaO_2 and KO_2. The diffraction data did not reveal any supercell that would be associated with ordering of Ba/K. Rietveld refinements were carried out using fixed Ba/K occupancies determined by ICP analysis. The X-ray diffraction data were not sensitive enough to oxygen to determine the oxygen atomic positions (at Wyckoff position 4e, coordinates 0,0,z) or site occupancies with any precision. However, these parameters could be refined from neutron diffraction data collected on the x=0.224 and x=0.412 samples. The x=0.224 sample had a refined oxygen content of ∼93% (Table 3.1), consistent with the oxygen deficiency previously reported for samples of BaO_2 prepared under ambient pressure [21]. For the

more heavily doped x=0.412 sample the fit between the observed and calculated diffraction profiles did not improve when the oxygen occupancy was refined, and the value remained close to 100%. Therefore, it was concluded that x=0.412 has no oxygen deficiency within experimental uncertainty. As expected, the O-O bond length decreases with K-doping as the bond order increases.

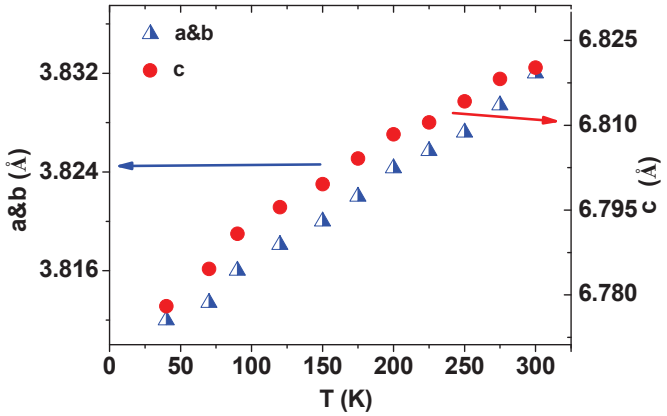

Figure 3.2: Lattice parameters of $K_{0.412}Ba_{0.588}O_2$ extracted from X ray diffraction as a function of temperature.

$K_{0.412}Ba_{0.588}O_2$	a (Å)	c (Å)	O-O (Å)	% oxygen deficiency
290K	3.8319(5)	6.8203(11)	1.439(6)	0
5K	3.8116(7)	6.7968(17)	1.407(10)	0

$K_{0.224}Ba_{0.776}O_2$	a (Å)	c (Å)	O-O (Å)	% oxygen deficiency
290K	3.8260(2)	6.8303(7)	1.467(3)	8(2)
10K	3.8091(2)	6.8075(7)	1.459(3)	6(2)

Table 3.1: Refined structural parameters of $K_{0.224}Ba_{0.776}O_2$ and $K_{0.412}Ba_{0.588}O_2$ extracted from neutron diffraction at room temperature and low temperature.

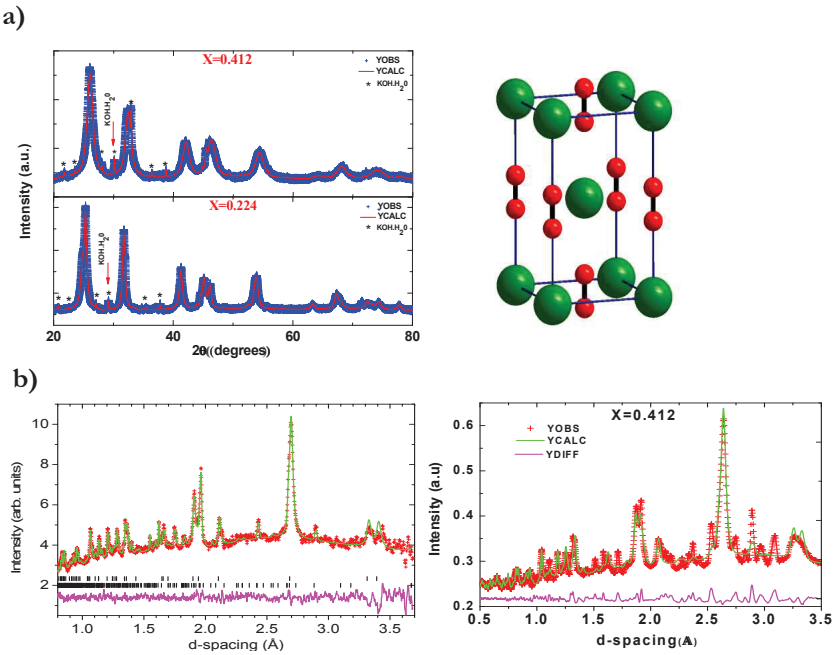

Figure 3.3: a) Crystal structure (right) and typical observed (blue data points) and calculated (red line) X-ray diffraction profiles for $K_xBa_{1-x}O_2$. Peaks corresponding to the $KOH.H_2O$ impurity are marked with asterisks. b) Observed, calculated and difference neutron diffraction profiles of $K_{0.224}Ba_{0.776}O_2$ (left) and $K_{0.412}Ba_{0.588}O_2$ (right) at 10 K and 5 K, respectively. The lower row of tick-marks corresponds to the peak positions of the $KOH.H_2O$ impurity. In the $K_{0.412}Ba_{0.588}O_2$ pattern extra peaks are visible that arise from a contaminated sample can.

Although KO_2 is known to undergo a series of structural phase transitions below room temperature involving tilts and shifts of the dioxygen anions, driven both by Jahn-Teller [22] and magnetogyration effects [23,24] no indication of such transitions was observed in $K_xBa_{1-x}O_2$ down to 5 K, the lowest temperature measured. By way of example, Fig. 3.2 shows the temperature dependence of the lattice parameters for the x = 0.412 sample; no obvious anomalies are visible. The evolution of the lattice parameters

with composition (x) at room temperature is shown in Fig. 3.4. The trend expected to be followed with increasing x is an increase in a towards 4.066 Å and a decrease in c towards 6.093 Å (the reported values for KO_2 [25]), the changes mainly being due to the shorter O-O bond length of the superoxide anion, the axis of which is aligned along c. However, there was a lot of scatter in the relatively small range of x covered by the current $K_xBa_{1-x}O_2$ samples. This might be due to variations in the number of oxygen vacancies in the lattice from sample to sample. Furthermore, deviations in the local structure from the average I4/mmm model cannot be ruled out. Particularly for the x = 0.412 sample, the temperature factor of oxygen determined by neutron diffraction was rather large at low temperature (Uiso = 0.045(4) $Å^2$ at 5 K, Uiso=0.031(3) $Å^2$ at 290 K), which suggests that the anion might not be aligned perfectly parallel to c as imposed by symmetry in I4/mmm.

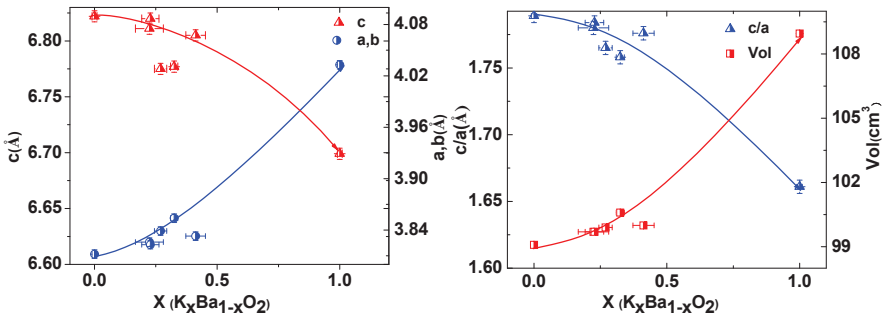

Figure 3.4: Evolution of lattice parameters, c/a ratio, and unit cell volume of $K_xBa_{1-x}O_2$ with composition.

The XRD and neutron diffraction peaks are much broader than the instrumental resolution; furthermore, the peak widths increase with composition. The change in the full width at half maximum (FWHM) of the 112 peak with x (determined from the XRD data and corrected for the instrumental peak width), which is the only isolated peak without a component from the $KOH.H_2O$ impurity, is listed in Table 3.2. The peak broadening

hints either at small particle sizes (coherently diffracting domain sizes) of the order of 15-30 nm, which might be feasible for polycrystalline samples grown at low temperature from solution, or alternatively at a considerable degree of structural disorder or a high density of nano-sized domains. It is likely that there is considerable freedom in the orientations of the dioxygen anions. The axes of anions that are close in nature to superoxide (that is, surrounded by more K than Ba) are expected to tilt away from the c-axis in order to break the orbital degeneracy [26]. However, the nominal concentration of superoxide anions in our samples is at most $\sim$40%, which is likely far too low to give rise to a cooperative structural distortion, and hence the symmetry will remain I4/mmm on average with the anions oriented along c as seen by a standard diffraction experiment. As discussed further in Chapter 4, it is possible that the distribution of K and Ba is not perfectly uniform over the bulk sample. This could give rise to regions with slightly different lattice parameters, which would have the effect of broadening the diffraction peaks. Annealing the samples at 100 C resulted in narrower diffraction peaks, suggesting that the degree of long-range structural order can be improved. However, heating also began to break down the structure, as evidenced by the appearance of extra diffraction peaks that could not be indexed, as shown in Fig. 3.5. Therefore, in order to ensure as high sample quality as possible in terms of purity, the samples discussed in this thesis were not thermally annealed.

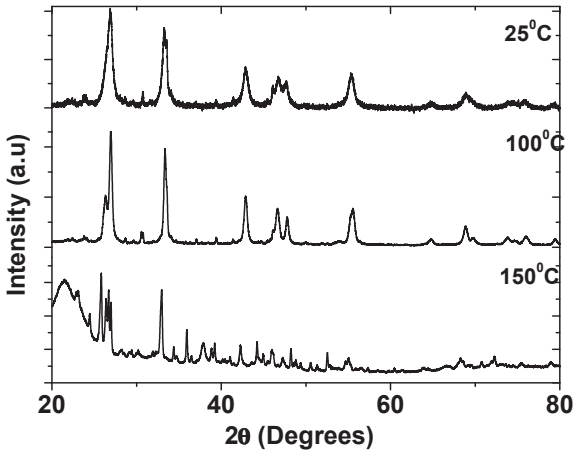

Figure 3.5: XRD patterns of $K_{0.412}Ba_{0.588}O_2$ before and after annealing.

Composition ($K_xBa_{1-x}O_2$) X	**Peak broadening (FWHM) (degrees)**	**Crystallite /domain size (nm)**
0.224	0.33	27
0.228	0.41	21
0.269	0.56	16
0.325	0.56	16
0.412	0.65	14

Table 3.2: Change in width of 112 peak with composition in $K_xBa_{1-x}O_2$ and rough estimate of crystallite size / coherently diffracting domain size from the Scherrer formula.

3.3.2 Magnetic properties

Figure 3.6 shows the dc magnetic susceptibility as a function of temperature for all five $K_xBa_{1-x}O_2$ samples. All follow Curie-Weiss behavior at high temperature:

$$(\mathrm{T}) = (\mathrm{N_A}/3\mathrm{k_B})\ (\mu_{eff}^2/\mathrm{T}\text{-}\theta) + \chi_0 \qquad \text{-(3.1)}$$

The inclusion of a temperature independent χ_0 term was necessary to account for the diamagnetic contribution of the sample holder. The effective magnetic moments (μ_{eff}) and Weiss constants (θ) of the samples, extracted from fits in the region 100 K to 200 K, are listed in Table 3.3. Here the composition given in the first column of the table has been assumed. Although there is a general trend towards higher μ_{eff} with increasing superoxide concentration, there are considerable discrepancies compared to the spin-only values expected for one unpaired spin per nominal superoxide anion.

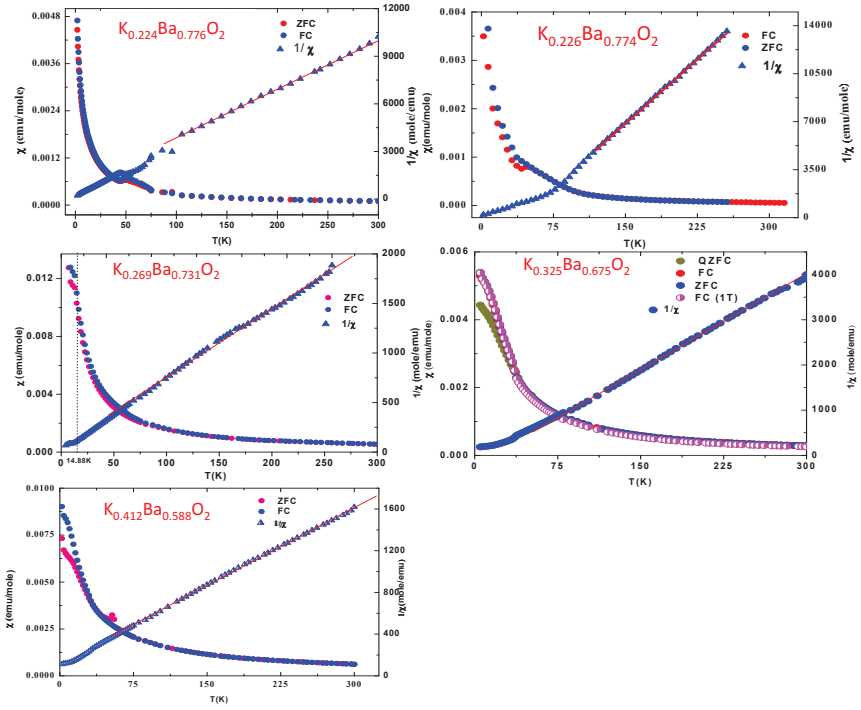

Figure 3.6: Field-cooled (FC) and zero-field-cooled (ZFC) magnetic susceptibility versus temperature for all five $K_xBa_{1-x}O_2$ solid solutions. The inverse susceptibilities are also shown together with Curie-Weiss fits.

It should be noted that uncertainties of up to ±5% are associated with the K:Ba ratios in the samples. Furthermore, the neutron diffraction data suggested that up to 7% of the anion sites are vacant for the lower doped samples, consistent with previous reports on BaO_{2-x} [21,27]. The inverse susceptibility at high temperatures deviates slightly from linearity for most of the samples.

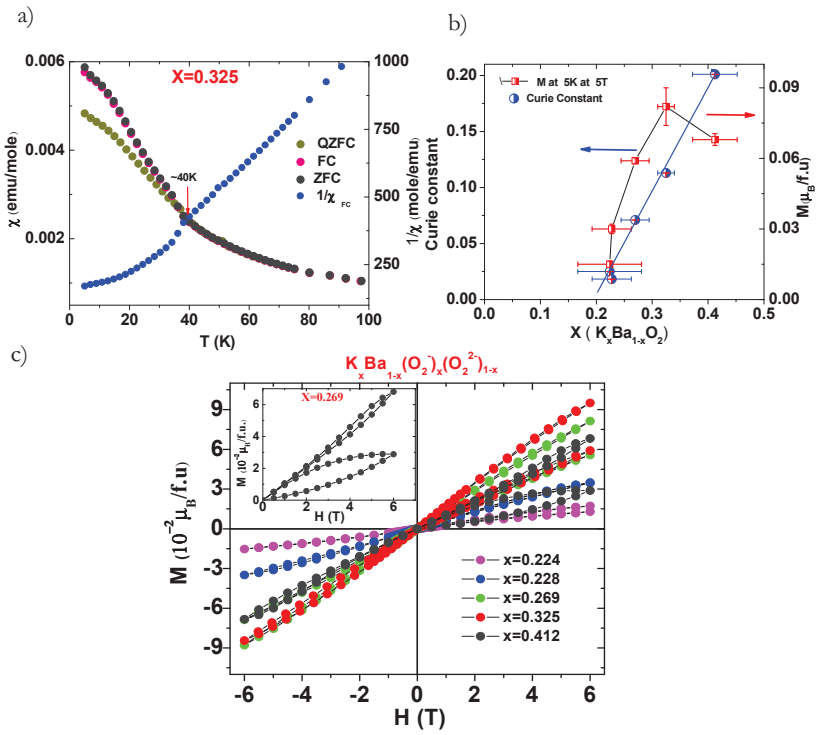

Figure 3.7: a) Magnetic susceptibility of $K_{0.325}Ba_{0.675}O_2$ versus temperature, measured after field cooling (FC), zero-field cooling (ZFC) and zero-field quenching (QZFC). b) Curie constant in paramagnetic region (blue data points) and magnetization at 5 K and 5 T (red data points) as a function of doping. c) Magnetization of all five $K_xBa_{1-x}O_2$ samples versus applied field, measured at 5 K. The inset shows two successive magnetization-field cycles for $x = 0.269$.

For the x = 0.412 sample the effective magnetic moment is considerably higher than the expected value, indicating considerable deviation from Curie-Weiss behavior. This might indicate that significant magnetic correlations remain at high temperature, perhaps due to double exchange. This aspect is discussed in detail in Chapter 4. The absence of good Curie-Weiss behavior is also evidenced by the unexpectedly scattered nature of the extracted Weiss constants between different samples (Table 3.3), which even vary from positive to negative.

Deviations from Curie-Weiss behavior occur for all samples below ∼70 K, although no signature of long-range magnetic ordering is observed. However, the low-temperature susceptibility is dependent on the rate at which the sample is cooled, as shown Fig. 3.7a for x = 0.325. Three curves are shown. The sample was first quenched in zero field to 25 K by inserting the sample stick straight into the cold cryostat of the magnetometer before cooling at ∼10 K / min to 5 K, applying a magnetic field of 1000 Oe and collecting data on warming (QZFC). The field was then removed at room temperature, the sample was cooled at 10 K / min to 5 K, a field of 1000 Oe was applied and data were again collected on warming (ZFC). Finally, the sample was cooled from room temperature to 5 K at 10 K / min in 1000 Oe and data were collected on warming (FC). Although the ZFC and FC curves overlie each other at all temperatures, the QZFC curve is lower than the ZFC curve below ∼40 K. This suggests that the spins respond slowly to an applied magnetic field. More evidence for slow spin dynamics is found in measurements of magnetization versus applied field, which were performed as follows. The sample was cooled from room temperature by inserting the sample directly in the magnetometer cryostat at 25 K and then cooling to 5 K at a rate of 10 K/min in zero field, before a field was applied and ramped up to 6 T. The field was next decreased in small steps to -6 T, before being increased to 6 T again. A second M-H cycle was then performed. Data for all five samples are shown in Fig. 3.7b. The trend of M versus H is generally linear, indicating predominantly AFM interactions, supported by the rather low maximum value of M ∼0.1 μ_B per formula unit at 6 T for

the highest doped sample.

However, as can be seen most clearly in the inset for the x = 0.269 sample, pinched hysteresis loops were displayed, suggesting that weaker FM interactions were also present. These loops became much narrower for the second M-H cycle, whereas the magnetization at 6 T became significantly larger. It appears that there is a small field induced ferromagnetic (FM) moment. Furthermore, the FM moments become better aligned with cycling, implying that the spins respond to the field slowly, or "with difficulty". This is consistent with the fact that the anions must be rotated by the applied field because the spin direction is rigidly fixed perpendicular to the anions; there will be an energy barrier to this process. Significant anisotropy is expected in the magnetization, but single crystals would be required to study this. Data from these measurements are summarized in Table 3.3.

The slow response of the spins to an applied magnetic field suggested in Fig. 3.7b was studied in more detail by carrying out thermo-remanent magnetization (TRM) measurements on the x = 0.325 sample. The sample was quenched from room temperature to 25 K in zero field (QZFC), then cooled at 10 K / min to 5 K, and held for different "waiting times" (t_w)

Sample	μ_{eff} (μ_B / f.u)	M at 5T and 5K (μ_B / f.u.)	θ (K)
$K_{0.224}Ba_{0.776}O_2$	0.47	0.015	-2.2(1.1)
$K_{0.228}Ba_{0.772}O_2$	0.38	0.030	43.2(6)
$K_{0.269}Ba_{0.731}O_2$	0.75	0.059	-24.2(1.5)
$K_{0.325}Ba_{0.675}O_2$	0.95	0.082	16.2(6)
$K_{0.412}Ba_{0.588}O_2$	1.27	0.068	15.9(8)

Table 3.3: Magnetization at 5K and 5T, effective paramagnetic moment and Weiss constant for all five samples.

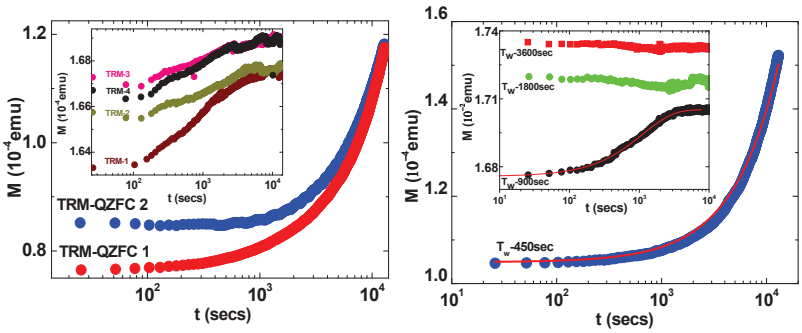

Figure 3.8: Thermoremanent magnetization of $x = 0.325$ sample as a function of time for (a) different and (b) constant (300 s) waiting times. The red lines show fits to Eq. (2).

. A field of 100 Oe was then applied and the magnetization was measured as a function of time. The data are shown in Fig. 3.8a. The longer the t_w, the greater is the initial value of M. For $t_w < 30$ min, M increases in response to the applied field according to a stretched exponential function:

$$M(t) = m_1(t^{-\alpha}) + m_2(1 - exp(\frac{-t}{\tau}))\text{.....(3.2)}$$

For $t_w = 450$ s, M is still increasing after more than 3 h. For $t_w = 900$ s, an equilibrium value of M is reached after ∼1 h. For longer t_w, M immediately reaches its equilibrium value after the field is switched on, suggesting that the spins are already in their equilibrium configuration. The fit parameters for Eq. (3.2) are listed in Table 3.4.

t_w (s)	m_1 (emu)	m_2 (emu)	τ (s)	α
450	1.0×10^{-4}	3.058×10^{-6}	1126	0.0
900	1.7×10^{-4}	0.00001	9685	-0.00015

Table 3.4: Fitted parameters for TRM data shown in Fig. 3.8a (see Eq. 3.2).

A second set of TRM measurements was carried out with the following protocol. The first set of data (labeled TRM-QZFC 1 in Fig. 3.8 b) was collected in analogous fashion to the $t_w = 450$ s data in Fig. 3.8a, stopping data collection after 4 h. The sample was then heated to room temperature before "slow cooling" back to 5 K at 10 K / min and collecting another data set with respect to time (TRM-1 in Fig. 3.8b). This procedure was repeated three times (TRM-2, TRM-3 and TRM-4). Finally, the sample was quenched to 25 K and "slow cooled" to 5 K (TRM-QZFC 2). This thermal cycling demonstrates that the sample displays a magnetic memory effect that persists to room temperature when "slow cooled"; the initial magnetization is higher on each subsequent TRM measurement and saturates after three or four cycles. Quenched cooling also gives rise to a small memory effect.A memory effect was also exhibited in the measurements shown in Fig. 3.9 for the x = 0.325 sample. The sample was cooled to 5 K using the QZFC procedure, a field of 100 Oe was immediately applied and M was measured as a function of time, exhibiting a slow increase. After ∼8000 s the field was switched off and the sample was simultaneously cooled to 2 K.

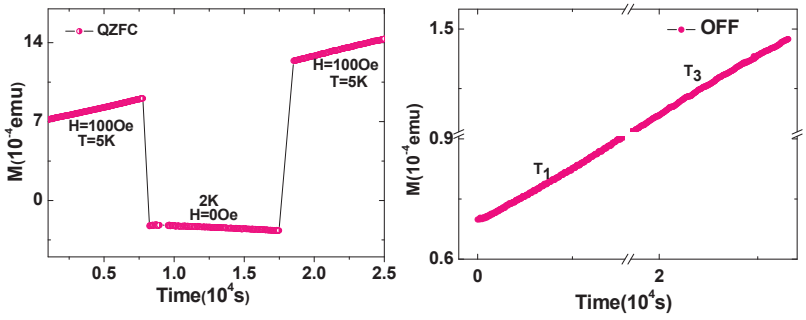

Figure 3.9: Magnetic memory effect for x = 0.325 sample with respect to changing field and temperature.

The sample now exhibited only a weak diamagnetic response, consistent with the lack of remanence in the magnetization versus field measurements in Fig. 3.7b. After holding for ∼10000 s in zero field, the sample was warmed

back to 5 K and the field of 100 Oe was simultaneously switched back on. The increase in magnetization continued exactly from the point at which the field was switched off; the sample "remembered" its previous magnetic state despite being held for ∼10000 s at lower temperature in zero field. This might be a consequence of the difficulty in rotating the anions, which within a particular FM domain or cluster are locked into their field-induced orientations.

3.4 Discussion

It has been shown that a range of mixed valent $K_xBa_{1-x}O_2$ solid solutions can be synthesized by the solution method in liquid ammonia solvent. This is helped by the fact that the crystal structure (at least on average) is body centered tetragonal (I4/mmm) for all members of the series at room temperature, including the end members. The maximum amount of superoxide anions that could be incorporated using this method was $x = 0.412$, which is less than the percolation limit, the concentration of Jahn-Teller-active ions necessary to give a coherent structural distortion (ie., the cooperative Jahn-Teller effect), thus samples with $x < 0.412$ show no change in structure with temperature. The lack of any visible superstructure in the XRD data implies that the K and Ba cations are probably disordered on the length scale of an XRD experiment, although better data are required to discount this possibility for sure. If there is no cation ordering, the local environment of the molecular oxygen anions will also be random on the diffraction length scale, giving an average structure in which there is an essentially random distribution of anions with characters intermediate between that of superoxide and peroxide. However, this might not be true on the nanoscale. Due to the difference in charge between K^+/Ba^{2+} and O_2^-/O_2^{2-}, it is quite probable that $K_xBa_{1-x}O_2$ can form small domains in which the cation distribution is more ordered. This hypothesis is supported by the considerable peak broadening in the XRD patterns. Although such broadening can be attributed to small crystallite size due to the low-temperature solution growth, the

change in width with composition strongly supports an increasing density of nanodomains with increasing x. As the Jahn-Teller active superoxide concentration increases, the material might segregate into chemically inhomogeneous domains with rich superoxide (potassium) content (Jahn-Teller distorted) and poor superoxide (potassium) content (non-distorted). Such behavior has previously been observed in $Zn(Ga,Mn)_2O_4$ spinels [28,29].

One of the end members of the $K_xBa_{1-x}O_2$ series, KO_2, is known to be an AFM insulator with $T_N = 7$ K. The $K_xBa_{1-x}O_2$ samples studied here showed inverse magnetic susceptibilities that deviate from Curie-Weiss behavior below ∼40 K (Fig. 3.6), which suggests that short-range magnetic ordering sets in. Neutron diffraction did not show any additional peaks at low temperature that would be characteristic of long-range AFM order. FM interactions are present at low temperatures, particularly when an external field is applied (Fig. 3.7). These samples show glassy behavior below 40 K, which is characteristic of competing AFM / FM interactions. This competition might arise from different chemical environments around nearest neighbor anions or from chemically distinct nanodomains with ordering of different types. For example, if two neighboring anions are superoxide-like (with a K-rich coordination) then the dominant interaction (depending on the local geometry and type of available exchange pathway) might be AFM, whereas if the nearest neighbors are superoxide-like and peroxide-like (with a Ba-rich coordination) then the interaction might be FM due to double exchange. Therefore, the degree of local cationic ordering will directly influence the type of exchange interaction by determining the character of the nearest neighbor anions. In order for FM double exchange to propagate over significant length scales, cation ordering would be required to ensure that every peroxide-like anion has six superoxide-like nearest neighbors. Such a lattice could be considered as charge-ordered. A completely disordered lattice with a random distribution of Ba and K would give rise to competing interactions, as observed. FM order would then be confined to extremely small clusters. In an analogous mixed-valent system $RbO_{1.72}$, short-range ferromagnetism appears to be more robust [16]. However, this material is

much more superoxide-rich than the $K_xBa_{1-x}O_2$ compounds studied here, it has a different crystal structure, and double exchange is less likely. Instead, the FM interactions are most likely due to superexchange that is driven by orbital ordering in small domains. In $K_xBa_{1-x}O_2$ the possible presence of chemically or electronically segregated domains can only be inferred from the magnetic properties and is not visible in diffraction patterns.

The cooling rate effect observed in the magnetic susceptibility (Fig. 3.7a) and the waiting time and thermal cycling effects observed in measurements of thermoremanent magnetization (Fig. 3.8) all indicate slow spin dynamics, most likely related to the difficulty in orienting the dioxygen dumbbells in an applied field. In the reverse process, after removal of a magnetic field the anions within a particular FM domain or cluster cannot easily return to their original zero-field orientations, as illustrated by the thermal cycling effect shown in Fig. 3.8b and the magnetic memory effect in Fig. 3.9.

3.5 Conclusion

It has been shown that a range of mixed valent $K_xBa_{1-x}O_2$ compounds can be stabilized by synthesis in liquid ammonia with varying magnetic superoxide content up to a maximum of $x = 0.412$. There is probably no cationic or charge ordering on the length scales probed by X-ray and neutron diffraction. The electronic structure of a particular dioxygen anion depends on its local cation environment and the magnetic exchange interactions it is involved in depend on the cation coordination of its nearest neighbors. Magnetic measurements provide evidence of inhomogeneous samples comprised of nanodomains or clusters with locally different magnetic exchange interactions. Below ∼40 K the samples exhibit signatures of competing magnetic interactions, and ferromagnetic interactions become more prominent in applied fields below ∼5 K. The magnetic susceptibility shows a weak cooling rate dependence and thermoremanent magnetization measurements indicate slow spin dynamics. This feature of $K_xBa_{1-x}O_2$ arises both from

the glassy behavior due to competing magnetic interactions and from the difficulty of reorienting spins in an applied field, which requires reorientation of the dioxygen anions themselves, involving an energy barrier. $K_xBa_{1-x}O_2$ exhibits a delicate balance between collective elastic interactions due to dumbell reorientation and corresponding magnetic interactions.

Bibliography

[1] Hesse, W.; Jansen, M.; Schnick, W. Progress in Solid State Chemstry 1989, 19, 47.

[2] Barnes, J. C.; Fahrenbach, A. C.; Dyar, S. M.; Frasconi, M.; Giesener, M. A.; Zhu, Z.; Liu, Z.; Hartlieb, K. J.; Carmieli, R.; Wasielewski, M. R.; Stoddart, J. F. Proceedings of the National Academy of Sciences of the United States of America 2012, 109, 11546.

[3] Bosch-Serrano, C.; Clemente-Juan, J. M.; Coronado, E.; Gaita-Ariño, A.; Palii, A.; Tsukerblat, B. ChemPhysChem 2012, 13, 2662.

[4] Heckmann, A.; Lambert, C. Angewandte Chemie International Edition 2012, 51, 326.

[5] Brunschwig, B. S.; Creutz, C.; Sutin, N. Chemical Society Reviews 2002, 31, 168.

[6] Dong, T. Y.; Ke, T. J.; Peng, S. M.; Yeh, S. K. Inorganic Chemistry 1989, 28, 2103.

[7] Hallier, K.; Hołyńska, M.; Rouzières, M.; Clérac, R.; Dehnen, S. Inorganic Chemistry 2012, 51, 3929.

[8] Lancaster, K.; Odom, S. A.; Jones, S. C.; Barlow, S.; Marder, S. R.; Coropceanu, V.; Bredas, J.-L. Abstracts of Papers of the American Chemical Society 2009, 237.

[9] Lancaster, K.; Odom, S. A.; Jones, S. C.; Thayumanavan, S.; Marder, S. R.; Bredas, J.-L.; Coropceanu, V.; Barlow, S. Journal of the American Chemical Society 2009, 131, 1717.

[10] Mechouet, M.; Perruchot, C.; Maurel, F.; Aeiyach, S.; Bucher, C.; Chardon, S.; Jouini, M. Journal of Physical Chemistry A 2012, 116, 970.

[11] Wutkowski, A.; Niefind, F.; Naether, C.; Bensch, W. Zeitschrift fur Anorganische und Allgemeine Chemie 2011, 637, 2198.

[12] Chu, Y. Y.; Wu, H. H.; Liu, S. C.; Lin, H.-H.; Matsuno, J.; Takagi, H.; Huang, J. H.; van den Brink, J.; Chen, C. T.; Huang, D. J. Applied Physics Letters 2012, 100, 112406.

[13] Shivakumara, C.; Hegde, M. S.; Srinivasa, T.; Vasanthacharya, N. Y.; Subbanna, G. N.; Lalla, N. P. Journal of Materials Chemistry 2001, 11, 2572.

[14] Teck-Yee, T.; Kennedy, B. J.; Qingdi, Z.; Ling, C. D.; Miller, W.; Howard, C. J.; Carpenter, M. A.; Knight, K. S. Physical Review B 2012, 85, 104107.

[15] Trinckauf, J.; Hanke, T.; Zabolotnyy, V.; Ritschel, T.; Apostu, M. O.; Suryanarayanan, R.; Revcolevschi, A.; Koepernik, K.; Kim, T. K.; von Zimmermann, M.; Borisenko, S. V.; Knupfer, M.; Buchner, B.; Geck, J. Physical Review Letters 2012, 108, 016403.

[16] Riyadi, S.; Giriyapura, S.; de Groot, R. A.; Caretta, A.; van Loosdrecht, P. H. M.; Palstra, T. T. M.; Blake, G. R. Chemistry of Materials 2011, 23, 1578.

[17] Winterlik, J.; Fecher, G. H.; Jenkins, C. A.; Medvedev, S.; Felser, C.; Kuebler, J.; Muehle, C.; Doll, K.; Jansen, M.; Palasyuk, T.; Trojan, I.; Eremets, M. I.; Emmerling, F. Physical Review B 2009, 79, 214.

[18] Seyb, E.; Kleinberg, J. Journal of the American Chemical Society 1951, 73, 2308.

[19] Toby, B. H. Journal of Applied Crystallography 2001, 34, 210.

[20] Larson A.C.; von Dreele, R. B. Los Alamos National Laboratory Report LAUR 2004, 867, 48

[21] Königstein, M.; Catlow, C. R. A. Journal of Solid State Chemistry 1998, 140, 103.

[22] Kemeny, G.; Kaplan, T. A.; Mahanti, S. D.; Sahu, D. Physical Review B 1981, 24, 5222.

[23] Bosch, M. A.; Lines, M. E.; Labhart, M. Physical Review Letters 1980, 45, 140.

[24] Lines, M. E.; Bosch, M. A. Physical Review B 1981, 23, 263.

[25] Smith, H. G.; Nicklow, R. M.; Raubenheimer, L. J.; Wilkinson, M. K. Journal of Applied Physics 1966, 37, 1047.

[26] Labhart, M.; Raoux, D.; Kanzig, W.; Bosch, M. A. Physical Review B 1979, 20, 53.

[27] Königstein, M. Journal of Solid State Chemistry 1999, 147, 478.

[28] Zhang, C. L.; Tseng, C. M.; Chen, C. H.; Yeo, S.; Choi, Y. J.; Cheong, S. W. Applied Physics Letters 2007, 91, 233110.

[29] Yeo, S.; Horibe, Y.; Mori, S.; Tseng, C. M.; Chen, C. H.; Khachaturyan, A. G.; Zhang, C. L.; Cheong, S. W. Applied Physics Letters 2006, 89, 233120.

Chapter 4

Charge Transfer in Mixed-Valent $K_xBa_{1-x}O_2$

An early charge transfer experiment by the illustrious American statesman Benjamin Franklin, ca 1752. Had a complete transfer of charge occurred, geopolitical history would surely have been written differently [1].

4.1 Introduction

Compounds that show mixed valence or mixed oxidation states have been the topic of fascinating research for many years, with respect to both their rich applicability and exciting fundamental chemistry and physics [2-11]. One little explored group of potentially mixed valent materials are the alkali oxides with chemical compositions between A_2O_2 (peroxide) and AO_2 (superoxide) where the oxygen content is non-stoichiometric [12]. An alternative way of realizing dioxygen mixed valence is to combine alkali and alkaline earth cations, as in the $K_xBa_{1-x}O_2$ system [13]. The detailed magnetic properties of $K_xBa_{1-x}O_2$ are presented in Chapter 3 and suggest that this is indeed a mixed valent system. In the current chapter, Raman spectroscopy is used to show that electronic charge transfer takes place between the dioxygen anions of $K_xBa_{1-x}O_2$ and that this charge transfer can be tuned by external stimuli such as light. In general, a mixed valent compound should contain components with at least two different oxidation states or valences, which can be considered as redox units. These units have nearly degenerate electronic states, which in the case of a molecule can be associated with different local structures that depend on the charge distribution. The charge distribution in such species is very sensitive to external stimuli such as pressure, temperature and light. Earlier studies by Robin and Day [2,3,14,15] identified three types of mixed-valent compounds that are classified according to the interaction strength between redox units. Schematic potential energy diagrams for this classification are shown in Fig. 4.1. If the interaction between the redox units is negligible, the compound is referred to as Class 1 and exhibits the property of isolated individual redox units. Compounds with strong interactions between the redox units are referred to as Class 3. In this case, the electron involved in the redox units is completely delocalized between the two species and the properties of the system are completely distinct from those of the individual units. Thirdly, compounds categorized as Class 2 exhibit moderate interactions.

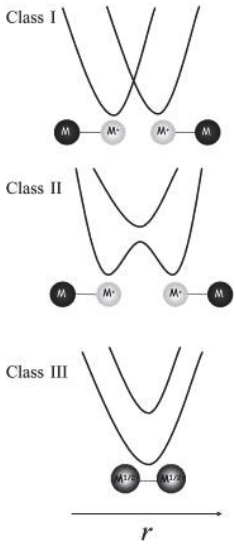

Fig 4.1: Potential energy curves for mixed valent compounds in the Robin and Day classification. Each unit shown is a redox center. This figure is taken from Ref. [16].

Here electrons are vibrationally localized at one of the redox centers and an activation energy (ΔG) is associated with charge transfer. This energy barrier can be overcome by external stimuli such as light, temperature and pressure. The charge transfer is referred to as an inter-valence electron transfer process (IET).

It is common practice in the field of chemistry and related areas to make a distinction between systems that exhibit mixed valence, spin crossover and valence tautomerism, even though it is clear that all these types of compounds can be described as electronically labile systems with two or more electronic states lying close in energy. All these systems are consequently controlled by vibronic interactions, which are sensitive to the external environment [16]. In mixed valent systems the excitation of electrons takes place between adjacent ions in a crystal and not within the individual cations/anions. These electronic transitions between neighboring ions fall within the broad definition of charge transfer (CT) transitions. In many cases CT tran-

sitions are excited by UV radiation. However, absorption edges may extend into the visible region and be manifested by coloration, or even beyond the visible region and into the short-wave infrared region (wavelengths in the range 400-2000 nm or wavenumbers 25,000-4000 cm^{-1}) [3]. An electron transfer between adjacent ions that momentarily changes the valence during the lifetime of the transition is referred to as an inter-valence transition. In mixed valent compounds the electron transfer process is dynamic and it also involves a change in the nuclear configuration due to coupling of the electronic and vibrational motion. In order for mixed-valent behavior to be shown in a sample, the following two conditions should be satisfied. 1) The degree of covalence in the interaction between two mixed valent species, here dioxygen ions, should be low. 2) The energy of their frontier orbitals must be similar. In other words, it is necessary that the species exhibit localized electronic structures, a low degree of orbital mixing and a small energy difference.

4.1.1 Mixed valence: Robin–Day model

The description first formulated by Robin and Day [14] is the commonly accepted classification of mixed valent systems and is discussed below. Examining mixed valent compounds more closely, they can be represented by electron donor and acceptor sites separated by a bridge (some distance) as shown in Fig. 4.2. When the redox sites are far apart the electronic interaction of the sites will be very weak [15].

Figure 4.2: Schematic representation of the donor and acceptor connected by a coupling distance referred to as the bridge. The figure is taken from Ref [15].

The intermolecular electron transfer reaction for sites that are relatively close can be described in terms of the motion of the system on an energy surface from the initial to final state. Due to the non-equivalent nature of the redox sites, an energy barrier is likely for charge transfer and site inter-conversion. When two states of a weakly coupled mixed valence system are interconverted, a charge transfer reaction (CT) takes place:

$$CBA \Leftrightarrow C^{+}BA^{-} = ABC$$

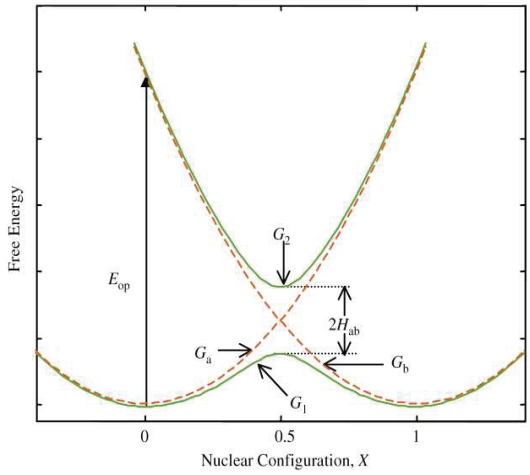

Figure 4.3: Free energies of the initial (G_a) and final diabatic states (G_b) and the lower (G_1) and upper (G_2) adiabatic states of a symmetric mixed valent system plotted with respect to the reaction coordinate. The energy E_{op} represents the electron donor-acceptor (IVCT) charge transfer transition. The energy H_{ab} represents the electronic coupling matrix element between two diabatic states. The figure is taken from Ref. [15].

Here for simplicity CBA and ABC are the notations used to represent the initial and final charge transfer states of a mixed valent system. Charge transfer in a mixed valent system results in distortions of the initial and final states, which can be described in terms of displacements on harmonic free-energy curves, both with identical force constants. This concept is depicted in Fig. 4.3 for a symmetric system. The free energy of the initial

state (CBA), together with its surrounding medium (curve G_a), and the free energy of the final state (ABC) with its surrounding medium (curve G_b) are plotted with respect to the reaction coordinate X.

Here G_a and G_b are the energies of the zero order states and can be expressed in terms of λ (the free energy difference between states CBA and ABC) and the reaction coordinate X:

$$G_a = \lambda X^2$$

$$G_b = \lambda(X-1)^2$$

The interaction between these two zero-order states results in two linear combinations that can be expressed as

$$\psi_1 = C_a\psi_a + C_b\psi_b$$

$$\psi_2 = C_a\psi_a - C_b\psi_b$$

These two expressions represent the adiabatic states, where ψ_1 and ψ_2 are the wave functions of the lower (ground) and upper (excited) adiabatic states respectively, and the mixing coefficients are $C_a^2 + C_b^2 = 1$. It can be shown that the energies of the adiabatic states are given by

$$G_1 = 1/2\{(G_a + G_b) - [(G_b - G_a)^2 + 4H_{ab}{}^2]^{1/2}$$

$$\mathrm{G_2} = 1/2\{(G_a + G_b) + [(G_b - G_a)^2 + 4H_{ab}{}^2]^{1/2}$$

The difference between these adiabatic energies is

$$(G_2 - G_1) = [(G_b - G_a)^2 + 4H_{ab}{}^2]^{1/2}$$

$$= [\lambda\ (1-2X)]^2 + 4H_{ab}{}^2]^{1/2}$$

It can then be shown [15] that the free energy of activation associated with interconversion of the redox sites is

$$\Delta G^* = [\lambda\text{-}2H_{ab}{}^2]/\ 4\lambda$$

This has a corresponding rate constant given by

$$k_{et} = A\exp[\text{-}[\lambda\text{-}2H_{ab}{}^2]/\ 4\lambda RT]$$

Here the prefactor A depends on the electronic coupling. For weak coupling the prefactor is the electron hopping frequency and for strong coupling the prefactor is determined by the nuclear vibration frequency. Normally, the properties of Class I mixed-valent systems are those of the individual redox sites, whereas in the case of Class II systems new properties are exhibited together with those of their constituent sites, in which the valence is trapped or the charge is localized. For Class III, completely new properties are exhibited relative to the constituent sites. Strong delocalization occurs. It is necessary to state that the systems under discussion here are restricted to two-state (ground and excited) symmetrical systems. Therefore, one can expect experimentally different scenarios when the system is more complex (for example asymmetric) than that assumed here. Most mixed-valent systems are found to lie on the border between Class II and III [15]. Here it will be shown that the electron transfer process in $K_xBa_{1-x}O_2$ takes place between two adjacent anions that have degenerate electronic structures. This electronic transfer is sensible to the chemical environment of the anions and is affected by external stimuli such as light. $K_xBa_{1-x}O_2$ can be designated as a borderline Class II /Class III type system.

4.2 Experimental

The synthesis and initial characterization of the samples used here were performed using the procedure described in Chapter 3. Micro-Raman spectra were measured using different setups for different conditions and requirements, which are described in detail in Chapter 2. X-ray diffraction in vacuum was performed using a Huber G670 Guinier camera system operating with CuK_α radiation on a sample contained in a glass capillary of 0.01

mm diameter. The capillary was loaded in a nitrogen-filled glove box and then sealed after pumping to 10^{-5} mbar pressure by attaching to a vacuum pump.

4.3 Results and discussion

A range of iso-structural solid solutions with varied K (i.e. superoxide) content were synthesized and characterized as described in Chapter 3 and studied further here by Raman spectroscopy. Raman spectroscopy is able to probe local structure and it provides valuable information on the mixed-valent nature of $K_xBa_{1-x}O_2$.

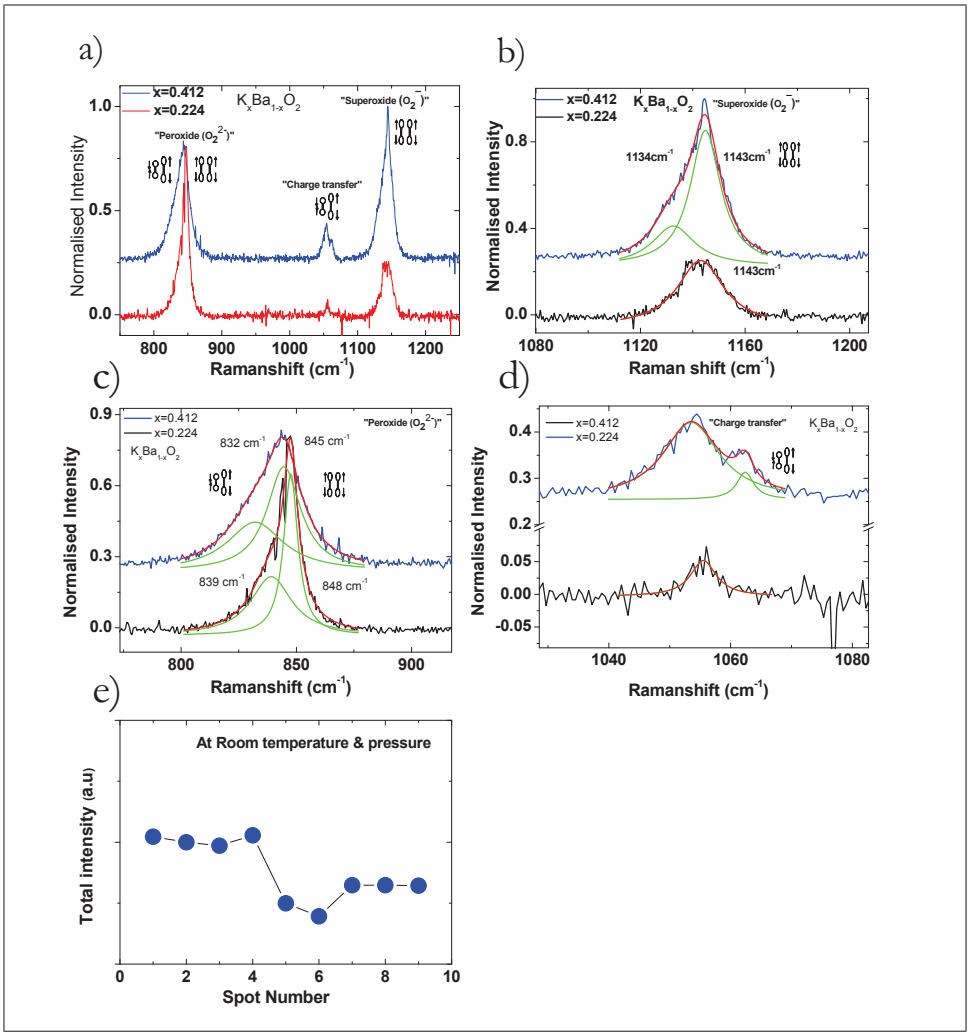

Figure 4.4: (a) Raman spectra of $K_xBa_{1-x}O_2$ (x= 0.224 and 0.412) at room temperature. (b)-(d) Lorentzian fits to the three O-O stretching mode peaks in (a), indicated by red and green lines. (e) Total integrated intensity of the three peaks in (a) measured by illuminating nine different spots of the sample with the laser.

4.3.1 Raman spectroscopy analysis

First, a group theoretical analysis of the Raman active modes for I4/mmm symmetry will be considered. The K/Ba atoms are found at Wyckoff position 2a with site symmetry 4/mmm and oxygen is at Wyckoff position 4e with site symmetry 4mm. The expected optical modes for $K_xBa_{1-x}O_2$ are

$$\Gamma_{op}(4/mmm) = A_{2u} + E_u$$

$$\Gamma_{op}(4mm) = A_{1g} + A_{2u} + E_g + E_u$$

Sample Name	Superoxide content (x)	Stretching mode position				Stretching mode width			
		Symmetric Stretching mode		Asymmetric stretching mode		Symmetric Stretching mode		Asymmetric stretching mode	
		$(O\text{-}O)^{2-}$ (cm^{-1})	$(O\text{-}O)^{-}$ (cm^{-1})	$(O\text{-}O)^{2-}$ (cm^{-1})	$(O\text{-}O)^{-}$ (cm^{-1})	$(O\text{-}O)^{2-}$ (cm^{-1})	$(O\text{-}O)^{-}$ (cm^{-1})	$(O\text{-}O)^{2-}$ (cm^{-1})	$(O\text{-}O)^{-}$ (cm^{-1})
BaO_2	0.0	842.6(8)	- -	- -	- -	4.9(5)	- -	- -	- -
KO_2	1.0	- -	1142.8(6)	- -	- -	- -	4.3(4)	- -	- -
$K_xBa_{1-x}O_2$	0.224	847.58(10)	1142.94(18)	839.1(1.4)	1054.23(11)	7.5(6)	21.7(1.1)	21(3)	8.82(6)
$K_xBa_{1-x}O_2$	0.412	844.8(9)	1144.82(18) 1132.6(10)	833(2)	1056.52(12)	13(2)	13.9(9) 20(3)	15(6)	13.256(8)

Table 4.1: Peak positions and widths of O-O stretching modes of BaO_2, KO_2 and $K_xBa_{1-x}O_2$ (x=0.224 and 0.412).

Only two of these modes, $A_{1g} + E_g$, are Raman active. The A_{1g} component is the normal (stretching) mode Σ_g^+ of the dioxygen anions, which appears in the range 750 to 1150 cm^{-1} depending on the electronic configuration and chemical environment of the anions. The E_g component is the anion librational mode and is normally found below 200 cm^{-1} [17]. In $K_xBa_{1-x}O_2$ it appears as broad feature around 200 cm^{-1}.

Figure 4.4a shows the room temperature Raman spectra of $K_xBa_{1-x}O_2$ where x=0.224 and 0.412. Three peaks are observed in the region between 700 and 1200 cm^{-1}, the range in which O-O stretching modes are expected to appear. The peaks at ∼840cm^{-1} and ∼1140 cm^{-1} are close to the positions of the previously reported O-O stretching modes for the O_2^{2-} and O_2^{-} species, respectively (843-851 cm^{-1} for BaO_2 depending on the oxygen stoichiometry

[18-20] and 1146 cm^{-1} for KO_2 [18,21,22]). Close inspection showed that both peaks were doublets and could be fitted using pairs of Lorentzian functions, except for the 1143 cm^{-1} peak of x = 0.224, which required only one Lorenztian (Fig. 4.4b). A third mode at 1053 cm^{-1} is also apparent in Fig. 4.4a; no O-O stretching mode close to this frequency has been reported in the literature.

Although the C-O stretching frequency of the carbonate anion is expected here, no evidence for the presence of carbonates was found in any of the X-ray diffraction patterns. The origin of this peak will be discussed below. The fitted peak parameters, together with those for Raman spectra of BaO_2 and KO_2, are summarized in Table 4.1. Although X-ray diffraction (Chapter 3) suggested that the alkali metals K/Ba are distributed randomly over the lattice, the Raman spectra suggest that the sample is inhomogeneous, perhaps with regions of different chemical composition. This is suggested by the variation in the total integrated intensity of all three modes when the laser spot was incident on different parts of the sample (Fig. 4.4e). The broad distribution of anion chemical environments is reflected by the broadness of the stretching modes compared to BaO_2 and KO_2. Although the peaks have been fitted with one or two Lorentzians, they should probably be envisaged as the sum of many narrower peaks covering a range of frequencies, arising from a range of different local chemical environments.

4.3.2 Theoretical implications

In an effort to better understand the Raman spectra in Fig. 4.4, density functional theory (DFT) calculations were performed by B. Zhang and R. de Groot. Only a brief summary is given here; details can be found in Ref. [23]. Oxygen dimers with an octahedral first coordination sphere of six mixed Ba and K neighbors were considered, where the molecular axis of the dimers is along the z-direction. In total, there are sixteen possible combinations of nearest neighbors for a given dimer when axial and equatorial sites are distinguished, excluding coordinations of six Ba or six K

cations. It was found that the calculated stretching mode frequency increases with the number of K nearest neighbors, as the character of the anion becomes more superoxide-like. Furthermore, a pair of Raman peaks was obtained when coupling between nearest neighbor anions was taken into account, where the higher frequency peak in each pair corresponded to the stretching motion of dimers coupled in phase, whereas the lower frequency peak corresponded to anti-phase motion. However, the calculated Raman frequencies associated with isolated dimers could not account for the observed Raman spectra. Therefore, a phonon calculation was performed on a compound with composition $K_2Ba_2O_8$ by doubling the tetragonal cell in the *c*-direction where the magnetic moments of dimers on adjacent layers were coupled antiferromagnetically, as reported in the literature for KO_2. In this model an ordered distribution of Ba and K was used: two K-O layers were followed by two Ba-O layers. A total of four Raman-active modes were calculated, at 1134 cm^{-1} (resulting from the in-phase stretching of two dimers coordinated by five K and one Ba), 1068 cm^{-1} (from the anti-phase coupling of two dimers coordinated by five K and one Ba), 887 cm^{-1} (from the in-phase coupling of two dimers coordinated by one K and five Ba), and 868 cm^{-1} (from the anti-phase coupling of two dimers coordinated by one K and five Ba). The calculated frequency of 1134 cm^{-1} is close to the experimental value of ∼1140 cm^{-1}. The corresponding anti-phase peak at 1068 cm^{-1} is also in reasonable agreement with the experimentally observed 1053 cm^{-1}. Due to the mixed valence of $K_xBa_{1-x}O_2$, charge transfer likely takes place during the anti-phase stretching motion of two adjacent dimers in a K-rich environment and this peak can hence be seen as a signature of charge transfer. The "Ba-rich" peaks calculated at 887 cm^{-1} and 868 cm^{-1} might contribute to the extremely broad experimental peak centered at ∼840 cm^{-1}. The two lower frequency peaks in the experimental spectrum likely contain contributions from neighboring dimers with different K/Ba surroundings to those in the simple model above. It should be noted that the X-ray diffraction data gave no indication of cation ordering as assumed in this model, but modeling disorder is computationally expensive in DFT

calculations and the ordered model reproduces the essential features of the observed Raman spectra.

4.3.3 Photo-induced charge transfer

4.3.3.1. Laser power induced charge transfer

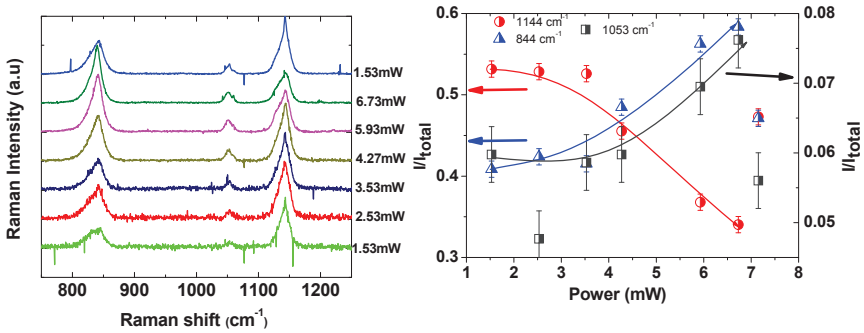

Figure 4.5: a) Raman spectra of $K_{0.412}Ba_{0.588}O_2$ at different laser powers. b) Integrated intensities of the three stretching modes as a function of laser power (normalized to the total integrated intensity of the three peaks).

Figure 4.5 shows the evolution of the three stretching modes as a function of laser power for $K_{0.412}Ba_{0.588}O_2$. The spectra were taken under the same conditions, with an integration time of 300 s and a laser spot size of 3 μm. In order to exclude the influence of time and possible cumulative laser heating effects, the scans were taken at different spots of the sample each time the power was changed. The peak intensities plotted in Fig. 4.5b were normalized to the total integrated intensity of the three peaks combined. To avoid any influence from fluorescent emission during analysis of the spectra, the background was subtracted before the total integrated intensity of the peaks was calculated. The distribution of spectral intensity between the three modes changes with increasing laser power from 1.43 mW to 6.73 mW (from the bottom spectrum to the second-top spectrum in Fig. 4.5a). Both the out of phase peak at 1053 cm^{-1} and the broad double peak centered at

840 cm^{-1} increase in intensity with increasing power. When the laser power on the same sample spot is decreased back to 1.53 mW (top spectrum in Fig. 4.5a), the spectral weight of the peaks returns to the original low-power distribution. The change in intensity of the 1053 cm^{-1} and 843 cm^{-1} modes with increasing power is perhaps due to light-induced charge transfer between neighboring anions which would also involve cationic reordering in order to maintain local charge balance. DFT calculations [23] suggested that the O-O stretching modes of anions with coordinations ranging from 6Ba+0K to 3Ba+3K are found in the 800-900 cm^{-1} range (neglecting any anion coupling). Thus, if light induces a more homogeneous distribution of K^{+} and Ba^{2+} cations in a nearly half-doped sample then there would be a significant shift in spectral weight to the region $<$900 cm^{-1}. The air sensitivity of these materials makes it difficult to set up an experiment to probe any changes in crystal structure with laser power, for example with a pump-probe XRD experiment. It should also be noted that the reversibility of this effect that occurs on decreasing the laser power is difficult to explain within this scenario. The thermal effect of the laser might induce cation reordering by thermal annealing but this would also likely be an irreversible process. Another explanation for the shift in spectral weight with laser power could involve the excitation of electrons to the π^* antibonding level from a lower energy level. It is known from earlier studies of the electronic spectra of alkali superoxides that an intramolecular transition within the superoxide anion is allowed between the $^2\Pi_g$ ground state ($3\sigma_g^2\ 1\pi_u^4\ 1\pi_g^3$) and the $^2\Pi_u(3\sigma_g^2\ 1\pi_u^3\ 1\pi_g^4)$ excited state for light of Π-polarization; the energy gap is $\sim$5eV. The transition from $^2\Pi_g$ to $^2\Delta_u$ ($3\sigma_g^2\ 1\pi_u^4\ 1\pi_g^2\ 3\sigma_u^1$) is also allowed for Σ-polarization, with an energy gap of $\sim$3eV. It is known that the yellow color of the superoxides is due to the $^2\Pi_g$-$^2\Delta_u$ transition [24]. The 514 nm (2.4 eV) laser light used has insufficient energy to induce one of these excited states, but in mixed valent $K_{0.412}Ba_{0.588}O_2$ the anions are not of superoxide character, as shown by the greyish brown color of the compounds in this solid solution series, thus excited states might be accessible. It is therefore possible that illumination with light induces excitations

from the filled π^* to empty σ^* level of the same anion. The extra hole that is created in the π^* level of the excited anion might then promote electron transfer to it from the π^* level of an adjacent anion, which could contribute significantly to the intensity redistribution in the Raman spectrum as the $^2\Delta_u$ excited state becomes more populated with increasing power. This scenario would also explain the reversibility of the spectral weight shift when the laser power is reduced. However, absorption spectroscopy should be carried out in order to probe the excited states of the mixed valent anions in $K_{0.412}Ba_{0.588}O_2$ and thus to check how feasible this picture is.

4.3.3.2. Enhancement of light-induced CT with time: photoannealing

Figure 4.6 shows the changes in relative intensity and width of the peaks that occurred when $K_{0.412}Ba_{0.588}O_2$ was irradiated with a 514 nm laser beam for 24 h at a constant power of 5.93 mW. The stretching mode with a peak at 1144 cm^{-1} became better resolved into two components centered at 1132 cm^{-1} and 1144 cm^{-1}, with a consequent decrease in total intensity. The 1132 cm^{-1} component became sharper with time. This narrowing is likely due to cationic ordering leading to a better defined local anion environment, which would correspond to an irreversible change in the local structure. The modes near ∼843 cm^{-1} did not show any significant change in width with time, but the in-phase stretching mode increased in intensity relative to the out-of-phase component. Overall, the intensity redistribution that occurred with time was similar to that induced by increasing laser power discussed in the previous section. Under the conditions of constant power possibly both the π^* to σ^* excitation and permanent cationic reordering (photoannealing) occurred with time. It should be noted that the heating effect from the laser is considerable and unavoidable. By considering the thermal conductivity of BaO from the literature [25] and using the formula given below, the maximum temperature increase induced by the 5.93 mW laser is ∼50 C.

$$\text{Spot temperature} = I_a/(2rk)$$

Here I_a is the absorbed light energy, k is the thermal conductivity of the sample and r is the radius of the laser spot.

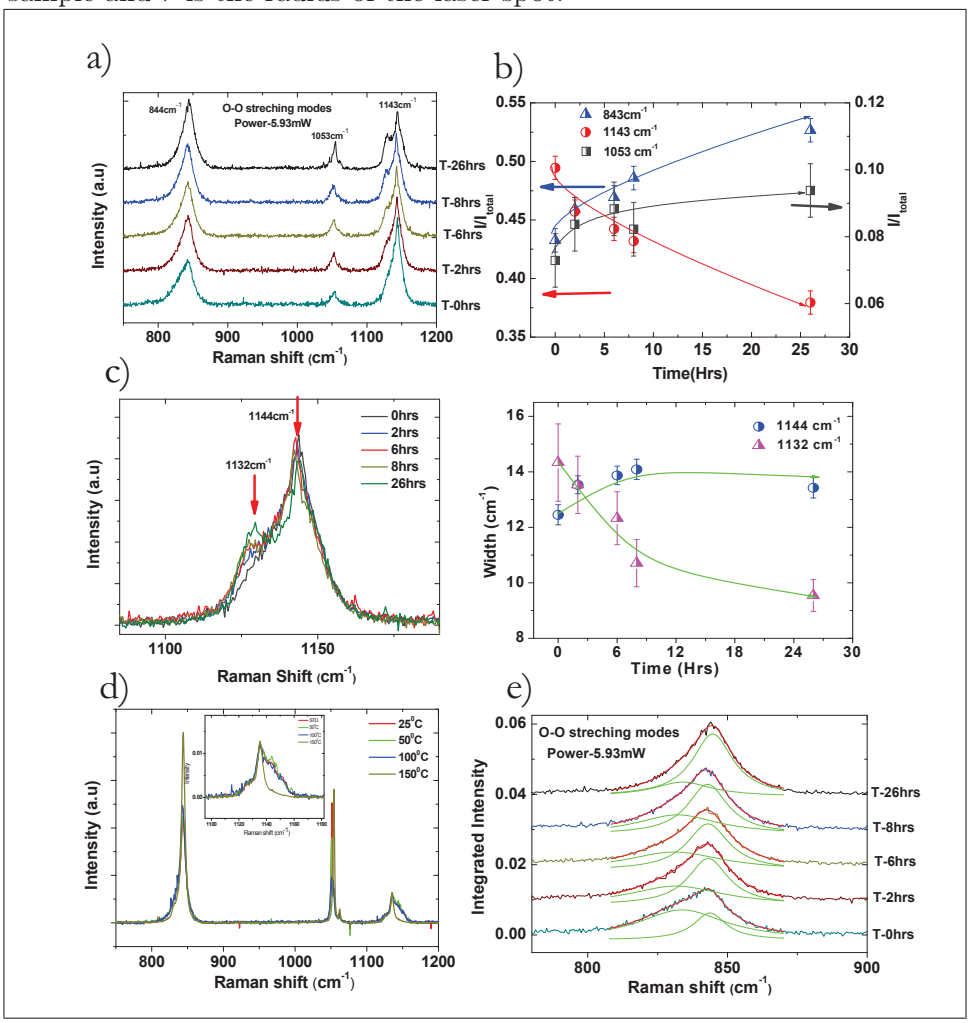

Figure 4.6: a) Raman spectra of $K_{0.412}Ba_{0.588}O_2$ at a laser power of 5.93 mW, measured after different times of laser illumination. b) Intensities of the three O-O stretching peaks at a constant laser power of 5.93 mW with respect to time; intensities have been normalized by the total integrated intensity. c) Evolution with time of the two components comprising the doublet at ~1140 cm^{-1}. d) Influence of thermal annealing on the O-O stretching modes. e) Evolution of the 843 cm^{-1} peak with time.

From the X-ray diffraction measurements described in Chapter 3 it can be concluded that $K_xBa_{1-x}O_2$ decomposes at ∼150 C. Therefore, laser-induced heating is never strong enough to break down the sample.

4.3.3.3. Vacuum enhanced charge transfer

Figure 4.7 shows Raman spectra of $K_{0.412}Ba_{0.588}O_2$ measured at room temperature between 1 bar and 10^{-5} mbar. In the setup used it was very difficult to control the pressure, so intermediate pressures could not be quantitatively measured. Raman spectra were also collected after argon was introduced to increase the pressure back to 1 bar from vacuum. The effect of several of these pressure cycles was al so studied.

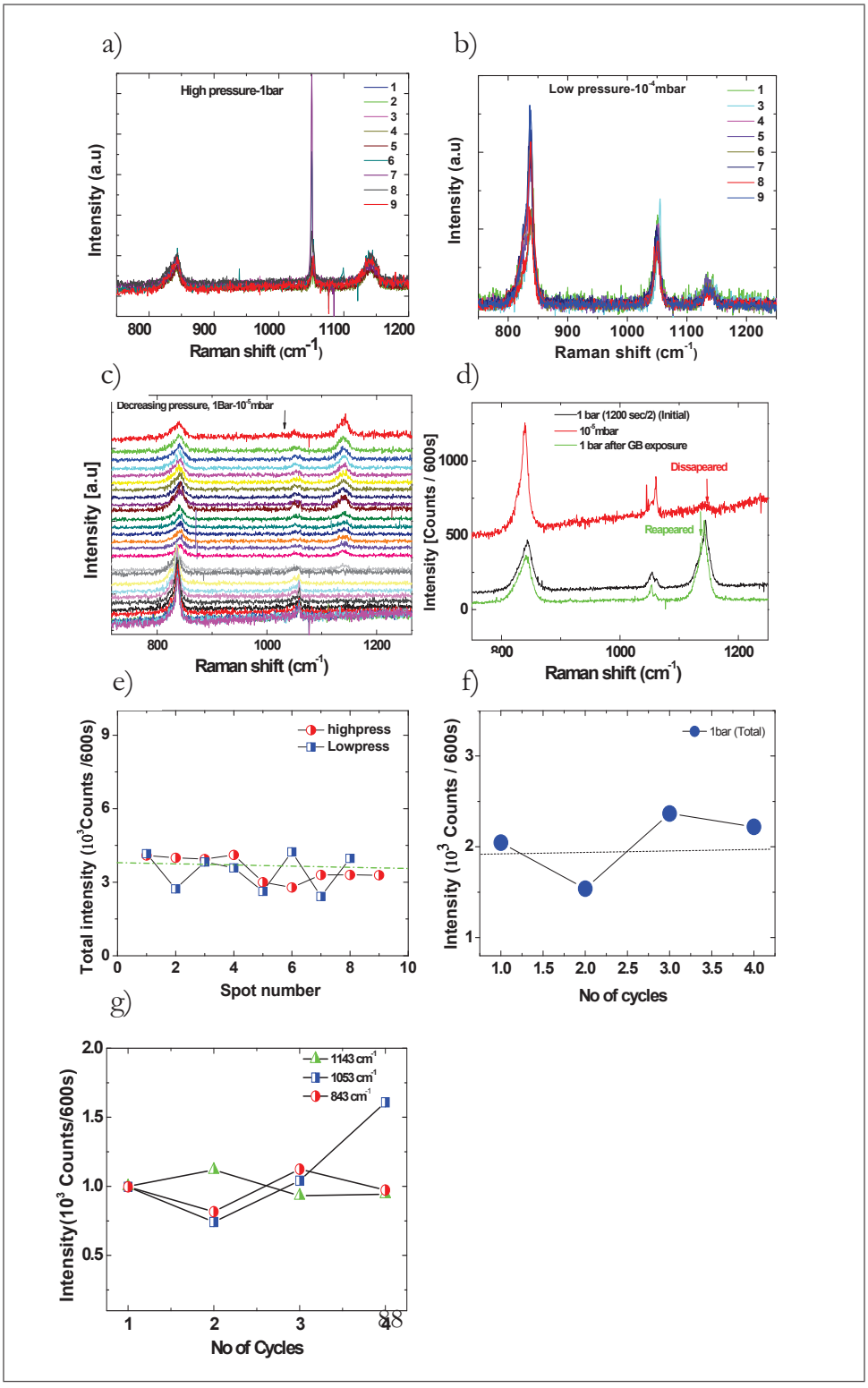
a)
High pressure-1bar
Intensity (a.u)
Raman shift (cm-1)
b)
Low pressure-10-4mbar
Intensity (a.u)
Raman shift (cm-1)
c)
Decreasing pressure, 1Bar-10-5mbar
Intensity [a.u]
Raman shift (cm-1)
d)
1 bar (1200 sec/2) (Initial)
10-5mbar
1 bar after GB exposure
Dissapeared
Reapeared
Intensity [Counts / 600s]
Raman shift (cm-1)
e)
highpress
Lowpress
Total intensity (10³Counts /600s)
Spot number
f)
1bar (Total)
Intensity (10³ Counts / 600s)
No of cycles
g)
1143 cm-1
1053 cm-1
843 cm-1
Intensity(10³ Counts/600s)
No of Cycles

Figure 4.7: a), b) Raman spectra of $K_{0.412}Ba_{0.588}O_2$ measured at 1 bar and under vacuum (10^{-5} mbar), each at 9 different sample spots. c) Evolution of Raman spectra on lowering pressure from 1 bar to 10^{-5} mbar (intermediate pressures could not be quantitatively measured). d) Raman spectra for one pressure cycle: the sample was first measured at 1 bar, then the pressure was lowered to 10^{-5} mbar, then argon was reintroduced to 1 bar. e) Total integrated intensity summed over nine different sample spots at 1 bar ("high pressure") and 10^{-5} mbar ("low pressure"). f) Total integrated intensity of all three peaks during four evacuation cycles. g) Individual integrated intensities of the three O-O stretching mode peaks during four evacuation cycles.

Figures 4.7a and b show the Raman spectra of $K_{0.412}Ba_{0.588}O_2$ measured under pressures of 1 bar and 10^{-5} mbar, each at nine different spots of the sample. Figure 4.7c shows Raman spectra measured on the same spot while lowering the pressure. Figure 4.7d shows Raman spectra measured at 1 bar, then after evacuating to 10^{-5} mbar, and finally after reintroducing argon gas to 1 bar (one pressure cycle). Figures 4.7e and f show the total integrated intensity of the O-O streching mode peaks at high and low pressure for nine different spots of the sample, and for a single spot after performing four pressure cycles, respectively. Figure 4.7g shows the changes in intensity of the three induvidual peaks over four pressure cycles. First, it should be noted that spectra measured on different spots of the same sample show significant differences in spectral weight distribution (Figs. 4.7a and b), suggesting that the local chemical environment and hence chemical composition are inhomogeneous on a macroscopic scale. However, the overall trend of the spectral weight redistribution that occurs on evacuation (Figs. 4.7a – d) is the same as that with laser power and light exposure time as earlier discussed. Indeed, in vacuum this feature is even more pronounced; the ∼1140 cm^{-1} peak decreases in intensity to almost zero whereas the ∼840 cm^{-1} and 1053 cm^{-1} peaks both show a strong increase. The shift in spectral weight is completely reversible when the inert gas pressure is brought

back to 1 bar (Fig. 4.7d). This suggests that a new metastable state is formed under vacuum, where light-induced charge transfer has taken place. DFT calculations [23] showed that neighboring anions with a K-rich environment are more strongly coupled than those with a Ba-rich environment. This might explain why the relative changes in intensity of the peaks in the ∼840 cm^{-1} doublet are less significant than those of the ∼1140 cm^{-1} and 1053 cm^{-1} peaks. It should be noted that under vacuum one may expect a fraction of oxygen to be removed from the surface of the sample, probably in the form of oxygen molecules. However, departing O_2 molecules would each need to donate a π^* electron and it is unclear how charge balance in $K_xBa_{1-x}O_2$ could be maintained. Furthermore, the observation that both the integrated intensities of the individual peaks and the total integrated intensity of all three peaks stay the same within experimental uncertainty over at least four evacuation cycles (Figs. 4.7e - g) rules out this possibility. This conclusion is also supported by the scanning electron micrographs shown in Fig. 4.9. Although these images were taken in air on a decomposed sample, the biggest particles are only a few hundred nm in size, with many being much smaller. This implies that if the effect of vacuum is mainly to remove oxygen from the surface, the particles would very quickly become oxygen depleted, which Raman spectroscopy shows not to be the case. The same pressure cycling experiment was performed in nitrogen as well as argon. No change in behavior was observed, which rules out surface chemistry involving gases being involved in the spectral changes. This evidence all suggests that the changes in the spectra involve an intrinsic electronic process.

In order to study whether structural changes take place on evacuation, XRD patterns were measured on two samples of $K_{0.324}Ba_{0.676}O_2$ contained in glass capillaries containing nitrogen gas at 1 bar and evacuated to 10^{-4} mbar (Fig. 4.8 and Table 4.2).

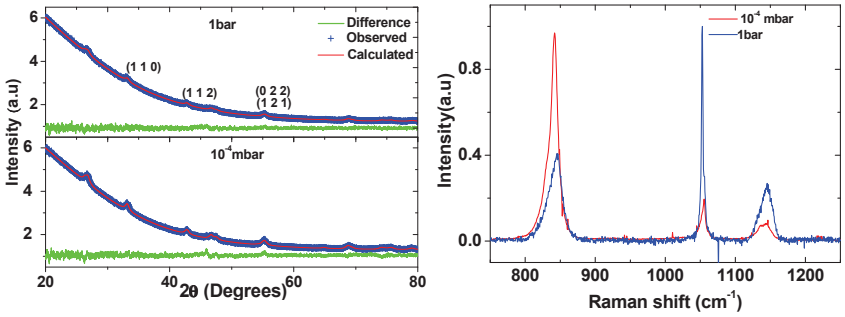

Figure 4.8: X-ray diffraction patterns (left) and Raman spectra (right) for $K_{0.324}Ba_{0.676}O_2$ at atmospheric pressure and under vacuum.

Pressure	**Lattice parameter (Å)**		**Peak width at half-maximum (degrees two-theta)**		
	a&b	c	110	112	022/121
1 bar	3.8299(7)	6.7869(14)	0.63	0.53	0.87
10^{-5} mbar	3.8326(4)	6.7916(8)	0.66	0.61	0.89

Table 4.2: Structural parameters for $K_{0.324}Ba_{0.676}O_2$ at atmospheric pressure and 10^{-4} mbar.

Despite similar changes in the Raman spectrum to those observed for $K_{0.412}Ba_{0.588}O_2$, no significant changes were observed in the lattice parameters or peak widths; the small differences in Table 4.2 are within experimental uncertainty because the XRD peaks were very broad with poor signal-to-background ratio and thus difficult to fit accurately.

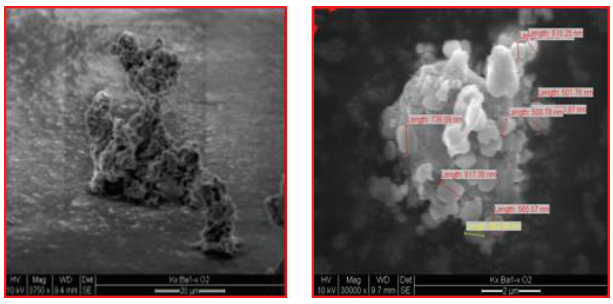

Figure 4.9: Scanning electron microscope images of decomposed $K_{0.412}Ba_{0.588}O_2$ sample with measurements of particle size.

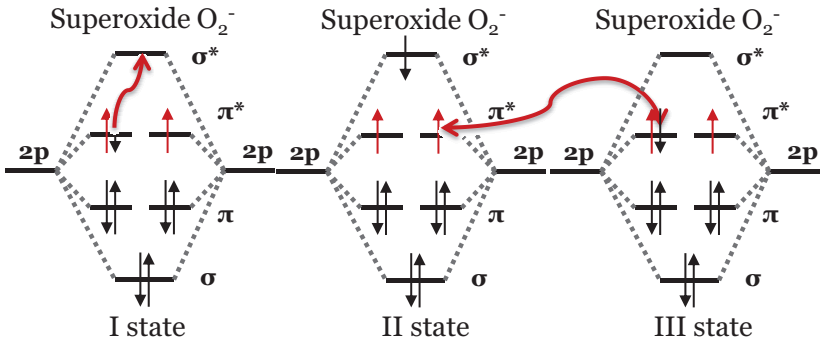

Figure 4.10: Illustration of possible mechanism of light-induced electron transfer in $K_xBa_{1-x}O_2$.

4.4 Summary and conclusion

Raman spectroscopy combined with DFT calculations suggests that there is considerable coupling between neighboring anions in $K_xBa_{1-x}O_2$ that is significantly influenced by the local cation coordination. This coupling involves charge transfer between anions, an effect that is enhanced by both light and vacuum. Based on the classification of mixed-valent systems by Robin and Day, $K_xBa_{1-x}O_2$ lies at the border between Class II and Class III where the coupling is moderate. In such compounds the redox centers

are separated by an energy barrier ΔG that can be overcome by external stimuli. In $K_xBa_{1-x}O_2$ it appears that such stimuli include light and lowering of pressure. The light-induced charge transfer is manifested in Raman spectra by a redistribution of spectral weight from the in-phase 1140 cm^{-1} stretching mode to the out-of-phase stretching mode at 1053 cm^{-1} and the in-phase mode at 843 cm^{-1}. The reversible nature of the light-induced shift in spectral weight on short time scales suggests that a purely electronic transition is taking place. A possible scenario is summarized in Fig. 4.10. Light of sufficient energy populates the $^2\Delta_u$ excited state in which an electron in the π^* level is promoted to the σ^* level. The hole in the π^* level that is generated by this excitation increases the probability of electron transfer from a π^* orbital of a nearest-neighbor oxygen dimer. This process appears to be enhanced in vacuum, and further studies will be required to understand why. With longer exposure times to the laser light, the broad peak at $\sim$1140 cm^{-1} becomes better resolved into its two components, which might be due to cationic reordering. The light-induced charge transfer probably induces the diffusion of cations in order to maintain local charge balance, which is a much slower process on the timescale of several hours and leads to an irreversible photo-annealed state. In both KO_2 and BaO_2, where no charge transfer takes place between dimers, the in-phase stretching mode is Raman active (the polarizability is not changing) while the anti-phase mode is Raman inactive (the polarizability is changing). On the contrary, in mixed valent $K_xBa_{1-x}O_2$, the π^* level on each dimer is dynamically occupied, which renders charge transfer available there, and both the in-phase and anti-phase stretching modes are Raman active. Another important difference is that in KO_2, light of at least $\sim$3 eV (less than 415 nm) is needed to induce the $^2\Pi_g$ to $^2\Delta_u$ excitation [24] (corresponding to the yellow color). The excited state in KO_2 would not be populated using the laser wavelengths in the current study and hence no change in the spectra with laser power or time would be expected. In summary, materials in which magnetic superoxide and nonmagnetic peroxide anions nominally coexist can be better thought of as mixed valent systems. The appearance of more than

two O-O stretching modes in Raman spectra is a signature of mixed valency. Additional fine structure can be observed on some of these modes as a consequence of differing local chemical environments. In $K_xBa_{1-x}O_2$ it has been shown here that the electronic coupling between neighboring dimers is moderate and can be enhanced by exposure to the external stimuli of light and evacuation. This coupling involves local charge transfer between anions that is comparable with double exchange in transition metal compounds. It would be interesting to search for novel mixed valent alkali oxides in which electrons become fully delocalized over the lattice where a metallic, ferromagnetic state is realized.

Bibliography

[1] Kite Experiment, Benjamin Franklin, copied from http://resenv.media.mit.edu/classes/MAS836/QPROX-white_paper.pdf

[2] Day, P. *Physics and Chemistry of Electrons and Ions in Condensed Matter*. Proceedings of the NATO Advanced Study Institute 1984.

[3] Day, P.; Hush, N. S.; Clark, R. J. H. Philosophical Transactions of the Royal Society A - Mathematical, Physical and Engineering Sciences 2008, 366, 5.

[4] Heckmann, A.; Lambert, C. Angewandte Chemie International Edition 2012, 51, 326.

[5] *Mixed Valency Systems: Applications in Chemistry, Physics, and Biology* (Edited by K. Prassides), Kluwer Academic Publishers, Dordrecht, Netherlands, 1991.

[6] Batlogg, B.; Ott, H. R.; Wachter, P. Physical Review Letters 1979, 42, 278.

[7] Dong, T. Y.; Ke, T. J.; Peng, S. M.; Yeh, S. K. Inorganic Chemistry 1989, 28, 2103.

[8] Lancaster, K.; Odom, S. A.; Jones, S. C.; Thayumanavan, S.; Marder, S. R.; Bredas, J.-L.; Coropceanu, V.; Barlow, S. Journal of the American Chemical Society 2009, 131, 1717.

[9] Mooibroek, T. J.; Aromi, G.; Quesada, M.; Roubeau, O.; Gamez, P.; DeBeer George, S.; van Slageren, J.; Yasin, S.; Ruiz, E.; Reedijk, J. Inorganic Chemistry 2009, 48, 10643.

[10] Peng, Y.; Tian, C.-B.; Zhang, H.-B.; Li, Z.-H.; Lin, P.; Du, S.-W. Dalton Transactions 2011 41, 4740.

[11] Wutkowski, A.; Niefind, F.; Naether, C.; Bensch, W. Zeitschrift fur Anorganische und Allgemeine Chemie 2011, 637, 2198.

[12] Hesse, W.; Jansen, M.; Schnick, W. Progress in Solid State Chemistry 1989, 19, 47.

[13] Seyb, E.; Kleinberg, J. Journal of the American Chemical Society 1951, 73, 2308.

[14] Robin, M. B.; Day, P. Advances in Inorganic Chemistry and Radiochemistry 1967, 10, 247.

[15] Brunschwig, B. S.; Creutz, C.; Sutin, N. Chemical Society Reviews 2002, 31, 168.

[16] Evangelio, E.; Ruiz-Molina, D. European Journal of Inorganic Chemistry 2005 (15), 2957.

[17] Singh, P.; Gaur, N. K. Physics Letters A 2007, 371, 349.

[18] Bates, J. B.; Brooker, M. H.; Boyd, G. E. Chemical Physics Letters 1972, 16, 391.

[19] Eysel, H. H.; Thym, S. Zeitschrift für Anorganische und Allgemeine Chemie 1975, 411, 97.

[20] Königstein, M.; Catlow, C. R. A. Journal of Solid State Chemistry 1998, 140, 103.

[21] Hunter-Saphir, S. A.; Creighton, J. A. Journal of Raman Spectroscopy 1998, 29, 417.

[22] Brame Jr., E. G.; Cohen, S.; Margrave, J. L.; Meloche, V. W. Journal of Inorganic and Nuclear Chemistry 1957, 4, 90.

[23] Zhang, B. PhD Thesis under preparation 2012.

[24] Bosch, M.; Kanzig, W. Helvetica Physica Acta 1975, 48, 622.

[25] Surplice, N. A.; Jones, R. P. British Journal of Applied Physics 1963, 14, 720.

Chapter 5

Sodium Superoxide (NaO_2) -Mixed valency and polymorphism

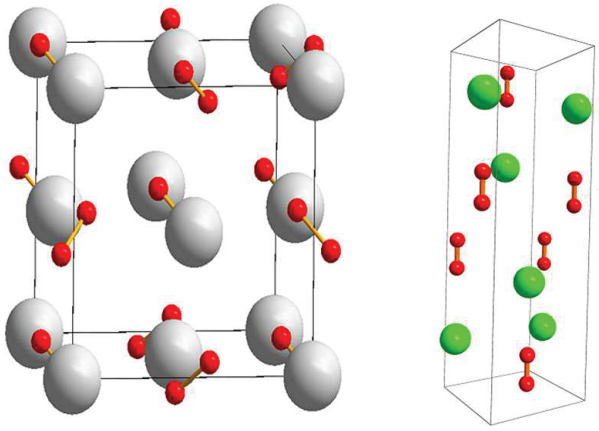

5.1 Introduction

Ionic salts containing the diatomic superoxide anion can be formed in combination with alkali metals and alkaline earth metals. These compounds are known to exist with the compositions AO_2, A_2O_3, A_2O_2 and A_2O (A=Na, K, Rb and Cs) [1-5]. However, alkali superoxides have been the main focus of research thus far, where the molecular ion O_2^- determines the physical properties. The chemical stability of alkali superoxides increases down the group. There are also structural differences, as discussed below. With a decrease in the ionic radii one can expect shorter interatomic/intermolecular distances, hence stronger magnetic exchange interactions and perhaps higher ordering temperatures. In this respect NaO_2 is a good candidate for further study, especially because the analysis and characterization of its structural and magnetic properties is not completely clear in the literature [6-9]. It is important to remember that cooperative phenomena occur in alkali superoxides where magnetic and molecular order is coupled to one another.

Sodium superoxide undergoes a series of structural phase transitions on cooling, which are summarized in Table 5.1 (taken from Ref. [5]). In common with the other alkali superoxides, NaO_2 adopts structures derived from rocksalt (NaCl). However, in contrast to KO_2, RbO_2 and CsO_2, which stabilize in the body centered tetragonal I4/mmm form at room temperature, NaO_2 adopts a cubic Fm-3m structure in which the superoxide anions are on average rotationally disordered (Fig. 5.1b) [3,5,10-12]. However, the anion orientations were found to have a tendency to align parallel to the [111] set of unit cell body diagonals, suggesting hindered rotation. At 230 K NaO_2 undergoes a disordered to ordered transition that is first order in nature [7,13]. The resulting structure is known as pyrite in analogy with FeS_2 and has the space group Pa-3 (Fig. 5.1a).

Table IV: Distinct structural phases of sodium hyperoxide - NaO_2

phase	temperature [K]	lattice constants [pm]	space group	structure	remarks*
I-NaO_2	223 <T	a = 551.2 [106, 114]	$Fm\bar{3}m$	NaCl; (disordered pyrite-type)	diffuse scattering on single-crystal X-ray-photographs [106]. X-P; X-SC; N-P
II-NaO_2	196<T<223	a = 546 [114, 115]	$Pa\bar{3}$	ordered pyrite-type	forbidden reflections due to formation of twin domains [3]. X-P; X-SC.
III-NaO_2	43<T<196	a = 433.2 b = 554.0 c = 336.4 [106]	Pnnm	marcasite-type [106, 116]	twinning-law established distinct domains resolved [106], antiferromagnetic short range order [106] X-P; X-SC N-P; N-SC.
IV-NaO_2	T<43	a = 433.5 b = 553.7 c = 335.3 [106]	Pnnm	marcasite-type	supposed antiferromagnetic long range order [109] could not be proved [106]. N-P.

*: X-P, X-SC: X-ray powder, single crystal (resp.) diffraction data
N-P, N-SC: neutron powder, single crystal (resp.) diffraction data

Table 5.1: Structural phase transitions of NaO_2 on cooling (taken from Ref [5]).

The anions are still directed along the [111] directions but in an ordered fashion. Twin domains are formed at this transition. On cooling further, transformation to the orthorhombic marcasite structure (Pnnm) takes place at 196 K (Fig. 5.1a). The orbital degeneracy of the O_2^- anions in alkali superoxides is generally lifted by a Jahn-Teller-type phase transition where the orientations of the dimers changes. Such a transition occurs in NaO_2 at the transition from the ordered pyrite to marcasite phases. Looking at the comparison of the two structures in Fig. 5.1a, in the marcasite phase the dimers within a layer are parallel, but staggered between adjacent layers. This transformation is discontinuous (first order) and results in 12 different twin domains. It has been suggested that this transition also results in a change from paramagnetic to short-range antiferromagnetic behavior and that a one-dimensional antiferromagnetic spin chain might be formed in the

marcasite phase [14]. It is thought but not proven that long-range antiferromagnetic ordering sets in below 43 K. Furthermore, neutron diffraction showed indications of a structural phase transition below 43 K, but the nature of the ground-state structure has not been reported. Thus, several questions need to be addressed in NaO_2. In addition to clarifying the ground-state crystal and magnetic structures, the correlation between magnetic and molecular order in the marcasite phase between 43 K and 196 K has not been studied in detail. Furthermore, the possibility of forming mixed-valent sodium oxide phases, for example by varying the oxygen content, has not been explored at all and the physical properties that such materials might have are unknown. This chapter reports on attempts to address these aspects of sodium oxides.

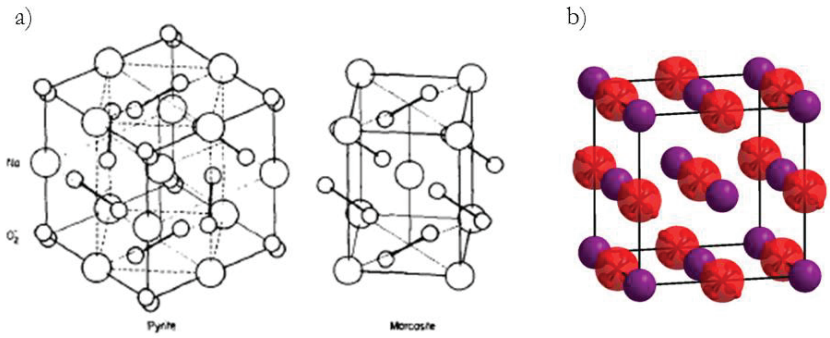

Figure 5.1: a) Relation between the ordered pyrite (left, Pa-3) and marcasite (right, Pnnm) structures of NaO_2 (taken from [5]). b) Crystal structure of room temperature disordered pyrite phase of NaO_2 (Fm-3m).

5.2 Experiments and techniques

5.2.1 Synthesis

Reports in the literature have suggested that it is rather difficult to synthesize NaO_2 with high purity [8]. NaO_2 can be synthesized by a solid-state method where Na_2O_2 is oxidized at elevated temperature and pressure (475

C and 280 bar) [5]. It would be useful to develop a simpler method to synthesize bulk samples that avoids the need for high pressure. Therefore, this chapter reports on the synthesis of polycrystalline sodium oxides by a solution method in liquid ammonia and methylamine solvent. Here the dissociation of $Na_2O_2.xH_2O$ is also investigated, which yields a material comprising a nominal mixture of superoxide and peroxide together with hydroxide ions.

5.2.1.1. Synthesis of mixed valent sodium oxide hydroxide

The synthesis of mixed valent sodium oxide hydroxide can be carried out by two different routes. One is by the disproportionation of $Na_2O_2.H_2O$ by heating followed by further oxidation in liquid NH_3 solvent and the second is by oxidation of Na metal in liquid NH_3. Both will be discussed in detail below.

Route 1: $Na_2O_2.H_2O$ disproportionation and further oxidation:

$$Na_2O_2.H_2O \xrightarrow[\Delta + \text{Evacuation}]{O_2} Na(O_2)_{1-x}OH_x \quad \text{.....1}$$

In Route 1, $Na_2O_2.xH_2O$ was heated to 200 C under vacuum to remove H_2O from the peroxide moiety and then the dehydrated compound was dissolved in liquid NH_3 solvent in a 100 ml reaction vessel and oxidized at -65 C by passing dry oxygen through the solution for two hours. The O_2 atmosphere of the reaction vessel was maintained at a pressure of 700 mbar. The temperature was stabilized using a PID temperature controller. After oxidation for one hour in liquid ammonia solution, a yellowish white precipitate was formed. Evaporation of the solvent yielded a lighter yellowish white powder. Characterization of the product is discussed in detail later in this chapter.

Route 2: Na metal oxidation in liquid NH_3:

$$\text{Na (Metal)} \xrightarrow[\text{Liq } NH_3]{[O_2]} NaO_2 \text{ (Cubic)} + Na(O_2)_{1-x}OH_x + NaNO_2 \quad \text{.....2}$$

The oxidation of Na metal in liquid ammonia (NH_3) at -65 C and at a static oxygen pressure of 750 mbar for 1 h also gave $Na(O_2)_{1-x}(OH)_x$, together with a smaller amount of hydroxide-free NaO_2 which was mainly formed on the walls of the reaction vessel near the surface of the solution. During oxidation a reddish yellow precipitate formed, which turned light whitish yellow after evaporation of the solvent. A small amount of $NaNO_2$ was produced by a side reaction with the solvent, discussed below.

5.2.1.2. Synthesis of sodium superoxide (NaO_2) by solution route

NaO_2 was synthesized according to Reaction 3, which differs from Reaction 2 in that Na metal was directly oxidised in a solvent consisting of mixed liquid ammonia and methylamine (CH_3NH_2). The reaction temperature was maintained between -70 C and -80 C and an O_2 pressure of 800 mbar was used. Increasing the proportion of methylamine systematically increased the fraction of NaO_2 in the product compared to undesired $Na(O_2)_{1-x}(OH)_x$ and the side products $NaNO_2$ and $NaNH_2$, as shown by the X-ray diffraction patterns in Fig. 5.2a and summarized in Table 5.2. However, pure methylamine could not be used because Na metal will not dissolve- a small amount of ammonia is always necessary. Minimizing the reaction time to ∼60 min with a high static oxygen pressure of 800 mbar in a 100 ml round bottom flask decreased the quantities of $NaNO_2$ and $NaNH_2$ in the product while still allowing the oxidation of sodium. The reaction time can be shortened by using a higher oxygen partial pressure. This is because it appears that there is a competing side-reaction in liquid ammonia solution, as depicted in Reactions 4-5 below [15]. The newly formed superoxide anions can react with ammonia to give amide and hydroxide anions. The amide anions can then react further with molecular oxygen, forming OH^-, NO_2^- and ammonia. The OH^- ions are responsible for the formation of $Na(O_2)_{1-x}(OH)_x$. This side reaction does not occur so readily in methylamine, thus higher yields of NaO_2 can be obtained. The solubility of the AO_2 product in liquid ammonia is the most important factor that determines the extent to which

the side reaction takes place. The relative difficulty in synthesizing pure superoxides of the lighter alkali metals relative to the heavier alkalis is thus due to the higher solubility of lighter alkali superoxides. The control of this reaction is discussed in detail in Chapter 2.

$$\text{Na (Metal)} \xrightarrow[\text{Liq } NH_3 + CH_3NH_2]{[O_2]} NaO_2 + Na(O_2)_{1-x}OH_x \quad \text{.....(3)}$$

Side reaction:

Ammonolysis of superoxide

$$O_2^- + 2NH_3 \longrightarrow 2OH^- + 2\,NH_2^- \quad \text{.....(4)}$$

Molecular O_2 can then react with the amide intermediate:

$$2\,NH_2^- + 3/2O_2 \longrightarrow OH^- + NO_2^- + NH_3 \quad \text{.....(5)}$$

The synthesis of pure NaO_2 in a solvent mixture that contains liquid ammonia is therefore difficult. It can be noted that the side reaction becomes even more important when considering the stability of an even lighter superoxide, LiO_2.

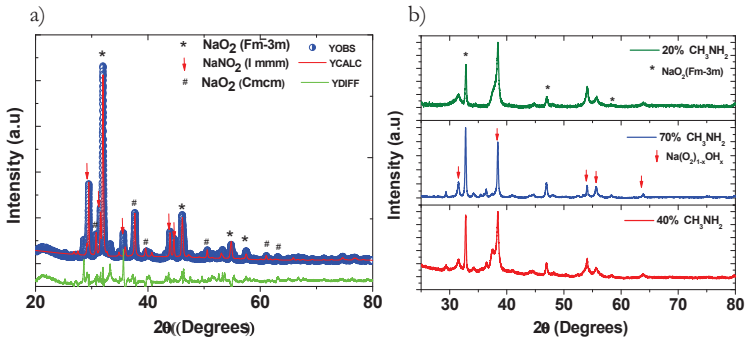

Figure 5.2: a) X-ray diffraction pattern of NaO_2 synthesized in liquid ammonia, showing presence of $Na(O_2)_{1-x}(OH)_x$ and $NaNO_2$ side reaction products. b) XRD patterns of samples synthesized in different proportions of liquid methylamine and ammonia.

Phase fraction	20% CH_3NH_2	40% CH_3NH_2	60% CH_3NH_2	70% CH_3NH_2
$Na(O_2)_{1-x}(OH)_x$	72.8	58.2	31.2	16.2
NaO_2	28.2	41.8	69.8	83.8

Table 5.2: Phase fractions determined by X-ray diffraction for solvent solutions with different amounts of methylamine (solvent compositions have uncertainty of 10-15%).

5.3 Results

5.3.1 $Na(O_2)_{1-x}(OH)_x$

5.3.1.1. Crystal structure of $Na(O_2)_{1-x}(OH)_x$

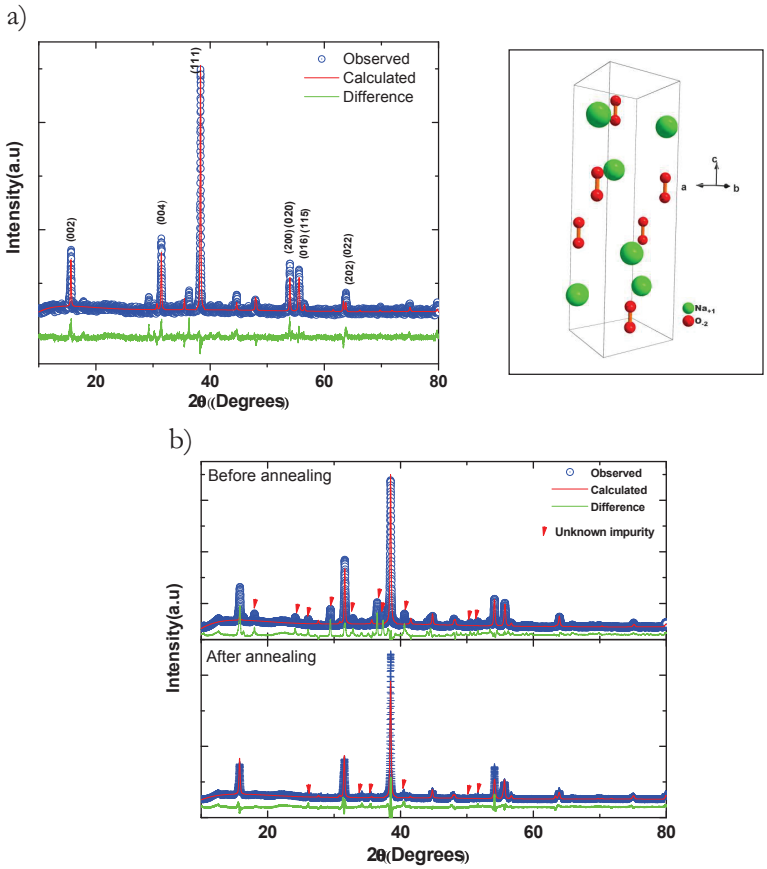

Figure 5.3: a) X-ray diffraction pattern of sample 1 and crystal structure of Na $(O_2)_{1-x}(OH)_x$. b) X-ray diffraction patterns of $Na(O_2)_{1-x}(OH)_x$ (sample 2) before and after annealing in oxygen atmosphere.

Two samples of $Na(O_2)_{1-x}(OH)_x$ were prepared. The first was synthesized by the dehydration of $Na_2O_2.xH_2O$ at high temperature followed by

oxidation in liquid NH_3 and the second was synthesized by the oxidation of Na metal in liquid ammonia. Figure 5.3 shows the crystal structure and X-ray diffraction pattern of sample 1. A good fit to the XRD pattern was obtained using an orthorhombic model with space group Bmmb, isostructural to the room temperature crystal structure of NaOH [16].

	Wyck	X	Y	Z	U_{11}	U_{22}	U_{33}
Na	4c	0.25	0.25	-0.087(1)	0.020(5)	0.020(5)	0.015(6)
O	4c	0.25	0.25	0.117(1)	0.013(5)	0.013(5)	0.017(6)
O(H)	4c	0.25	0.25	0.197(1)	0.07(2)	0.07(2)	0.016(6)

Table 5.3: Refined structural data for orthorhombic $Na(O_2)_{1-x}(OH)_x$ (sample 1) in space group Bmmb [16].

The refined structural parameters are given in Table 5.3. It is noted here that Raman spectroscopy data (Fig. 5.4, described in detail later in this chapter) show the presence of OH^-, O_2^- and O_2^{2-} ions, thus the refined atomic coordinates of O should be treated as average positions of O(H). Because hydroxide (OH^-) ions (O-H bond length ∼0.95 Å) are much smaller than those reported for superoxide and peroxide (∼1.33 Å/1.54 Å), one might expect a significantly different crystal structure to that of the host lattice NaOH [16]. However, the space group symmetry is the same and the lattice parameters of $Na(O_2)_{1-x}(OH)_x$ are only slightly larger, the biggest difference being a longer value of c, to which the anion axis is parallel (Table 5.4). Taking into account that the halide ions in alkali halides can be replaced by O_2^- while maintaining the rocksalt structure, the isostructural nature of NaOH and $Na(O_2)_{1-x}(OH)_x$ is similar in that hydroxide ions can be replaced by diatomic oxygen ions (O_2^-/O_2^{2-}). The structural data for NaOH in Table 5.4 are taken from the literature [16]. Soft constraints were placed on the O-O bond lengths shown in Table 5.4 for $Na(O_2)_{1-x}(OH)_x$ because they tended to refine to unrealistically short (∼1.0 Å) values. This is

probably due to the fact that the OH bond length is shorter than O_2^-(∼0.95 Å) and the distribution of OH^- and O_2^- is probably disordered. The oxidation of Na metal in liquid NH_3 gave an isostructural phase with possible different oxygen content. Sample 2 was annealed after the solution synthesisThe AO_2 sample prepared in Step 1 is sealed in a glass tube and heated in a box furnace (Fig. 2.5). The decomposition temperature can be determined by TGA-DSC analysis performed in a dry argon atmosphere, as shown in Fig 6.2. The heating of AO_2 leads to successive transformations involving the loss of oxygen, apparent as weight loss in the TGA curves and as peaks in the DSC plots. The multiple DSC peaks observed in the temperature range studied in Fig. 6.2 suggest that it might be possible to stabilize a range of oxygen deficient phases. The oxygen stoichiometry of the product is thus very sensitive to the temperature at which the sample is held. Furthermore, the decomposition reaction relies on the diffusion of oxygen out of the sample, hence the product obtained after a single heating cycle is inhomogeneous. in an O_2 atmosphere for 2 h at 100 C to remove unknown impurities (Fig. 5.3b).

Sample	**a**	**b**	**c**	**O-H/O-O bond length**	**Cell volume**
NaOH	**3.401(1)**	**3.401(1)**	**11.382(5)**	**0.9542(8)**	**131.65(10)A^3**
Na $(O_2)_{1-x}(OH)_x$	**3.399 (1)**	**3.4031(1)**	**11.4034(3)**	**1.3284(11)**	**131.9124(12)A^3**

Table 5.4: Refined crystallographic parameters for $Na(O_2)_{1-x}(OH)_x$ and NaOH at room temperature [16].

5.2.1.2. Raman spectroscopic analysis

Raman spectra of orthorhombic $Na(O_2)_{1-x}(OH)_x$ (sample 1 synthesized by the oxidation of Na_2O_2 route) are shown in Fig 5.4. Stretching modes at the wavenumbers expected for O_2^{2-} and O_2^- are observed at 808 cm^{-1} and 1136 cm^{-1}. Due to the presence of a trace amount of disordered pyrite NaO_2 in the sample, a weaker mode corresponding to O_2^- is observed at

1156cm^{-1}. The frequencies of O-O stretching modes are known to be very sensitive towards the type of cations or vacancies that surround the anions. A third mode at 1079 cm^{-1} is also observed. This can be assigned to the out-of-phase stretching mode of O-O dimers of superoxide-like character, which appears when there is charge transfer between adjacent anions in a mixed-valent system, as described in detail for $K_xBa_{1-x}O_2$ in Chapter 4. The presence of three O-O stretching modes identifies $Na(O_2)_{1-x}(OH)_x$ as a mixed valent sodium oxide phase.The AO_2 sample prepared in Step 1 is sealed in a glass tube and heated in a box furnace (Fig. 2.5). The decomposition temperature can be determined by TGA-DSC analysis performed in a dry argon atmosphere, as shown in Fig 6.2. The heating of AO_2 leads to successive transformations involving the loss of oxygen, apparent as weight loss in the TGA curves and as peaks in the DSC plots. The multiple DSC peaks observed in the temperature range studied in Fig. 6.2 suggest that it might be possible to stabilize a range of oxygen deficient phases. The oxygen stoichiometry of the product is thus very sensitive to the temperature at which the sample is held. Furthermore, the decomposition reaction relies on the diffusion of oxygen out of the sample, hence the product obtained after a single heating cycle is inhomogeneous.

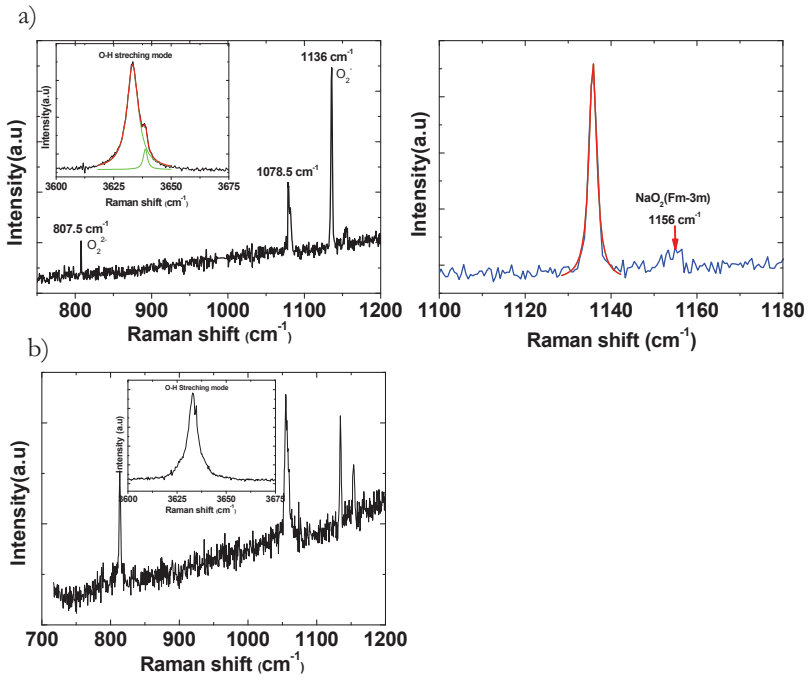

Fig 5.4: a) Raman spectroscopic analysis of orthorhombic $Na(O_2)_{1-x}(OH)_x$ (sample 1) showing peak fit using a Lorentzian function. b) Raman spectroscopic analysis of orthorhombic $Na(O_2)_{1-x}(OH)_x$ (sample 2).

An out-of-phase stretching mode for peroxide-like anions would also be expected, and might be responsible for the broad raised background at ∼790 cm^{-1}. The presence of peroxide-like modes implies that there must be dioxygen and/or hydroxide vacancies in order to maintain charge balance. The presence of a random distribution of vacancies thus allows local charge transfer to take place between adjacent dioxygen anions, manifested by in-phase and out-of-phase stretching modes. All these features were also observed for sample 2 , synthesized by the oxidation of Na metal in liquid ammonia and shown in Fig. 5.4b. The difference in intensity distribution relative to

sample 1, with more spectral weight on the peroxide-like 808 cm^{-1} peak, can be attributed to a difference in composition, most likely involving a higher average negative charge on the dioxygen anions and thus different oxygen content. In these compounds the presence of a small fraction of disordered cubic NaO_2 is unavoidable. An accurate estimation of the oxygen content in $Na(O_2)_{1-x}(OH)_x$ is very difficult, but can be inferred very approximately from the Raman spectra. Several assumptions are necessary. First, it is assumed that the sample is homogeneous on a macroscopic scale, so that the Raman spectra do not differ from spot to spot. Then, it is necessary to assume that the hydroxide to dioxygen ratio corresponds to the ratio between the integrated intensity of the O-H stretching mode peak and the sum of the intensities of the O-O stretching mode peaks. The integrated intensity ratio of the "superoxide" to "peroxide" O-O stretching modes in the Raman spectra then gives a rough estimate of the "superoxide" to "peroxide" ratio and thus the average charge per dioxygen anion. From charge balance considerations, the percentage of anion vacancies can then be calculated by assuming that there are equal proportions of hydroxide and dioxygen vacancies. These estimations yielded compositions of $Na(OH)_{0.655}(O_2)_{0.255}$ for sample 1 and $Na(OH)_{0.72}(O_2)_{0.18}$ for sample 2. It should be emphasized that these estimations are very approximate, and in particular the relative spectral weights of the O-H and O-O stretching modes should be checked using suitable reference samples.

5.3.1.3. Magnetic properties

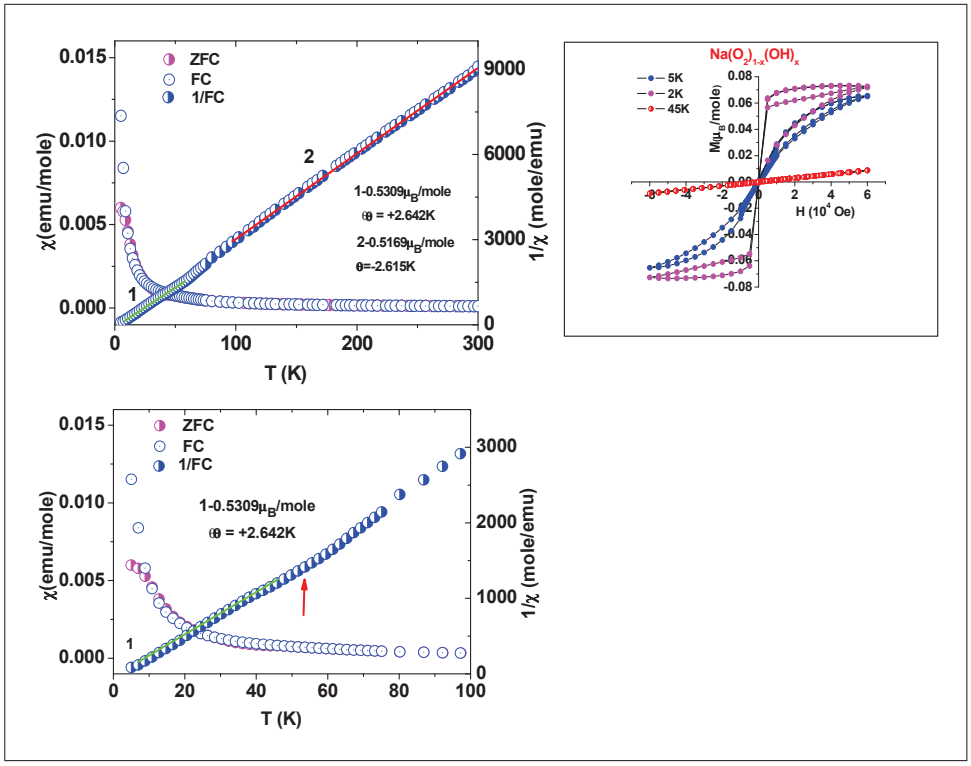

Figure 5.5: a) Temperature dependent magnetic susceptibility (left) and field dependent magnetization (right) of sample 1. b) Zoomed part of (a) in the low temperature region. The susceptibility data were measured on warming in a field of 1000 Oe after field cooling (FC) in the same field or zero-field cooling (ZFC).

Figure 5.5 shows a plot of magnetic susceptibility versus temperature for sample 1. The susceptibility is expressed in units of emu/mole by using the molar weight extracted from the Raman spectra, so there may be significant errors in the magnitude of the susceptibility and in subsequent fitted parameters. The susceptibility increases with decreasing temperature and a change in slope at ∼40 K suggests a possible magnetic phase transition, where it is likely that short-range antiferromagnetic order sets in (there is no

maximum as would be expected for long-range ordering). From the magnetization versus applied magnetic field data in Fig. 5.5b it is clear that at low temperature weak ferromagnetic interactions are induced in applied field, as shown by the opening of a hysteresis loop. The low saturation magnetization of ∼0.07 μ_B / f.u. at 2 K shows that the ferromagnetic component is small. The saturation magnetization varied between 0.07 μ_B/mole and 0.03 μ_B/mole from sample to sample. From a Curie-Weiss fit to the inverse susceptibility of sample 1, the effective paramagnetic moment of 0.52 μ_B / f.u. suggests that ∼1/3 of the anion sites are occupied by magnetic ions, assuming a simplified picture of distinct superoxide and peroxide ions. In this case the magnetic sublattice would be too dilute to give any long range magnetic ordering. The Weiss temperature of -3 K implies that weak antiferromagnetic interactions are dominant. The low temperature field-induced ferromagnetic component might be a signature of localized double exchange interactions between superoxide-like and peroxide-like anions. The closure of the hysteresis loop at zero field indicates that the ferromagnetic component is very soft. Because the spins of superoxide anions are known to be fixed perpendicular to the molecular axis, it might be necessary to apply a magnetic field to reorient the anions slightly to facilitate the hopping of electrons from one site to another.

5.3.2 Sodium superoxide (NaO_2)

5.3.2.1. X-ray diffraction – structural analysis

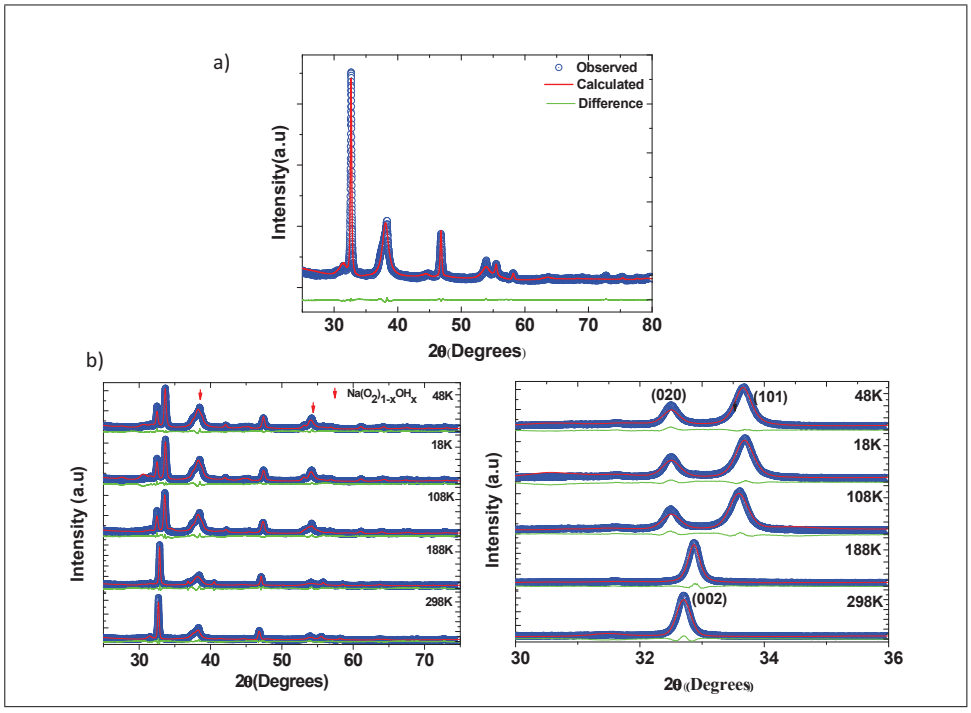

Figure 5.6: (a) Room temperature X-ray diffraction pattern of cubic sodium superoxide. (b) Evolution of XRD patterns on cooling. Arrows show peaks corresponding to the secondary $Na(O_2)_{1-x}(OH)_x$ phase.

Figure 5.6a shows the room temperature X-ray diffraction (XRD) pattern of the NaO_2 sample synthesized in 70% methylamine / 30% ammonia. The evolution of the XRD patterns on cooling is shown in Fig. 5.6b. The expected phase transition from the ordered pyrite (cubic) to marcasite (orthorhombic) phase was observed at 170 K, as shown by the changes in lattice parameters in Fig. 5.7 and apparent in the XRD patterns in Fig. 5.6b. Although the disordered-ordered pyrite transition is not immediately apparent from the XRD patterns, this phase transition is confirmed by a sharp peak at 228 K (cooling) in the DSC measurement shown in Fig 5.7c.

This feature is consistent with the expected first order transition. A weaker anomaly is visible at the pyrite-marcasite transition (200 K). There is thus a difference of ∼30 K between the transition temperatures observed by XRD and DSC. Because the DSC peak differs by at most 3 K on cooling and heating showing that temperature lag on the sample is minimal, the sample temperature in the XRD cooling chamber might have been higher than the thermocouple measured.

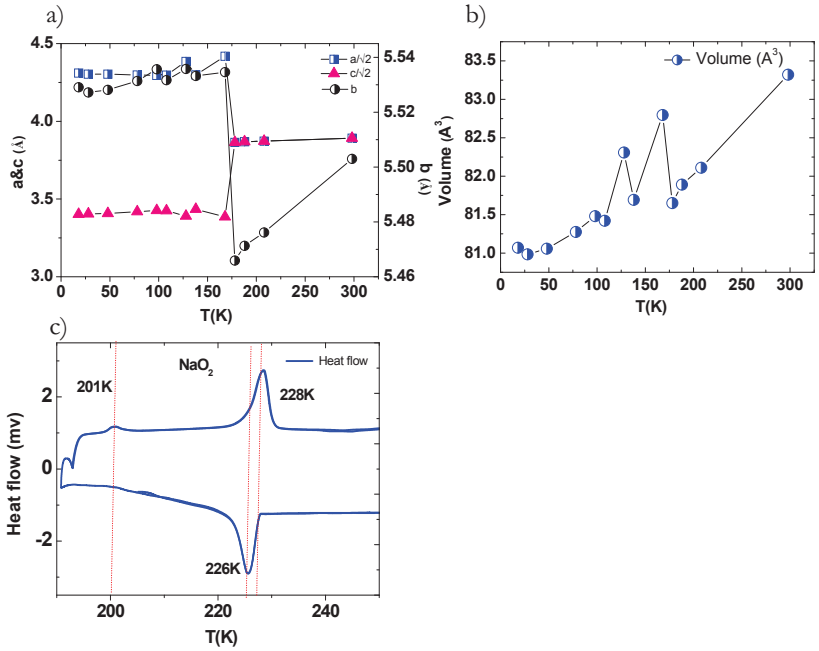

Figure 5.7: a) Lattice parameter evolution of NaO_2 with temperature. The cubic a and c lattice parameters have been divided by $\sqrt{2}$. b) Change in unit cell volume of NaO_2 with temperature. c) Low temperature differential scanning calorimetry (DSC) curve of NaO_2 on cooling (upper line) and heating (lower line).

The above structural and thermal analysis is consistent with the structural data in the literature. However, no phase transition or change in the

orientation of the anions was detected below 40 K from the diffraction data. Better diffraction data using a different technique are still needed to look for the structural response to the expected magnetic ordering. NaO_2 was thus studied further using Raman spectroscopy and magnetization measurements.

Temperature (K)	**Space group**	**a (Å)**	**b (Å)**	**c (Å)**	**O-O Bond length (Å)**	**Cell volume (Å^3)**
18	Pnnm	4.310(1)	5.5291 (1)	3.4018 (2)	1.395(7)	81.06(10)
300	Fm-3m	5.5097 (4)	5.5097 (4)	5.5097 (4)	1.3847(8)	167.2568

At 18K

Atoms	**Wyck**	**Site**	**x**	**y**	**z**	**Uiso**
Na	2a	..2/m	0	0	0	0.04892(6)
O	4g	..m	0.1255(8)	0.4203(5)	0	0.04892 (6)

Table 5.5: Refined structural parameters of NaO_2 at 18K and room temperature, and refined atomic coordinates at 18 K.

5.3.2.2. Raman spectroscopic analysis

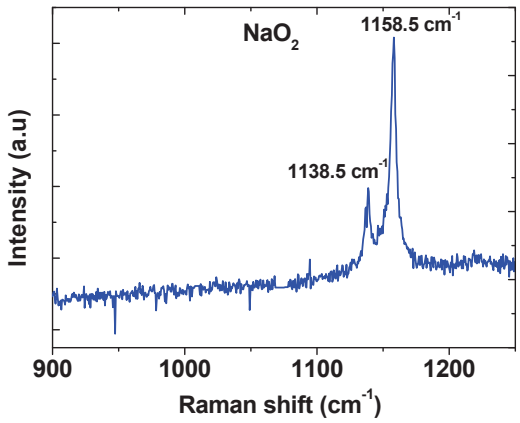

Figure 5.8: Room temperature Raman spectrum of disordered pyrite NaO_2.

Figure 5.8 shows the room temperature Raman spectrum of NaO_2 in the disordered pyrite (Fm-3m) phase. Consistent with the reported O-O stretching mode in alkali superoxides at ∼1150 cm^{-1} [17,18], the current sample showed this mode at 1155 cm^{-1}. A group theoretical analysis of the disordered pyrite phase gives the following expected oxygen-derived modes for the room temperature structure [7]:

$$\Gamma_{op} = A_g + E_g + 3F_g + 2A_u + 2E_u + 5F_u$$

Of these, 5 modes are Raman active, two of which are internal modes (A_g and F_g) and three of which are external modes (E_g and F_g), the latter being libration modes of dioxygen. The weaker peak at 1135 cm^{-1} is the in-phase O-O stretching mode for superoxide-like oxygen dimers in the secondary $Na(O_2)_{1-x}(OH)_x$ (Bmmb) phase. The presence of vacancies and/or OH^- ions in the coordination sphere of the dioxygen anions in the secondary phase leads to a weaker crystal field and a softening of the stretching mode by ∼20 cm^{-1} compared to NaO_2.

5.3.2.3. Magnetic properties

Figure 5.9 shows the magnetic susceptibility versus temperature for NaO_2. The magnetic behavior in both the disordered and ordered pyrite phases is paramagnetic. However, there is a sharp change in slope at the first order transition from the disordered to ordered pyrite structures. Both the disordered pyrite and ordered pyrite regimes were fitted using Curie Weiss functions, from which effective magnetic moments of 2.013 μ_B /f.u and 1.63 μ_B /f.u were extracted, respectively. These values are close to those expected for the spin-only moment of superoxide ions.

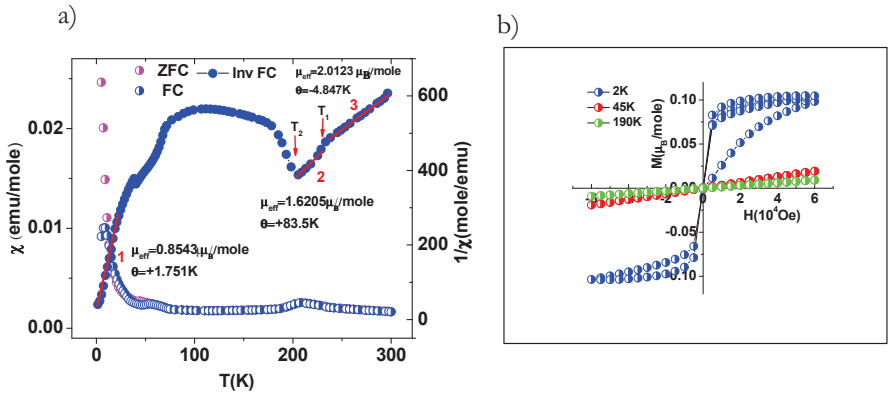

Figure 5.9: a) Plot of magnetic susceptibility and inverse susceptibility versus temperature for NaO_2. The data were measured on warming in a field of 1000 Oe after field cooling (FC) in the same field or zero-field cooling (ZFC). The Curie and Weiss constants are indicated for several regimes. T_1 and T_2 in the plot indicate transitions from the disorderd pyrite to ordered pyrite and from ordered pyrite to marcasite, respectively. b) Magnetization versus applied magnetic field at different temperatures.

The slightly lower effective magnetic moment and positive θ in the ordered pyrite region indicates possible short range ferromagnetic interactions, as previously suggested [14]. Below 190K the susceptibility decreases with decreasing temperature; the marcasite NaO_2 phase is thought to exhibit

possible one dimensional short range antiferromagnetic ordering due the overlap of magnetic orbitals along the *c*-axis (Fig. 5.10b). Such short range magnetic ordering in the form of a spin chain should be manifested by a broad maximum in the susceptibility data.However, in NaO_2 the susceptibility does not reach the broad maximum, which is calculated to be found at a temperature corresponding to 1.3 times the magnetic exchange constant *J*. Nevertheless, the susceptibility data below the maximum in the range 75 K to 190 K are consistent with the Heisenberg spin-1/2 chain model reported by Feyerherm et al. [20], as shown in Fig. 5.10a.

The value of *J* for marcasite was previously calculated to be 370 K [14], well above the marcasite-ordered pyrite transition. The model fits the data and values of $C = 0.425$ and J/k_{B} = -375 K were extracted, which agrees well with the previously reported value of J/k_{B} = -370 K. Below ∼75 K there is an increase in the susceptibility and there is another anomaly at ∼45 K. It is possible that these indicate transitions to different types of 3D antiferromagnetic ordering. However, the inverse susceptibility is still almost linear and a Curie-Weiss fit below 40 K yielded values of $\mu_{eff} = 0.854$ μ_B/f.u and a Weiss constant of $\theta = 1.75$ K, which suggests many of the spins are not long-range ordered. The magnetization versus applied field plot in Fig. 5.9b shows that NaO_2 exhibits a field induced ferromagnetic response at 2 K with a saturation magnetization of ∼0.1 μ_B/f.u. The curve looks similar to the response for $Na(O_2)_{1\text{-}x}(OH)_x$ (Fig. 5.9), but this secondary phase comprises only 14% of the sample thus can only be responsible for a small part of the ferromagnetism. It is possible that the application of field rotates the anions slightly, enough for a ferromagnetic superexchange pathway to become accessible. This could also explain the difference between the FC and ZFC magnetic susceptibility curves in Fig. 5.10a. The small value of the saturation magnetization shows that antiferromagnetic exchange remains dominant at low temperature, probably via a competing superexchange pathway.

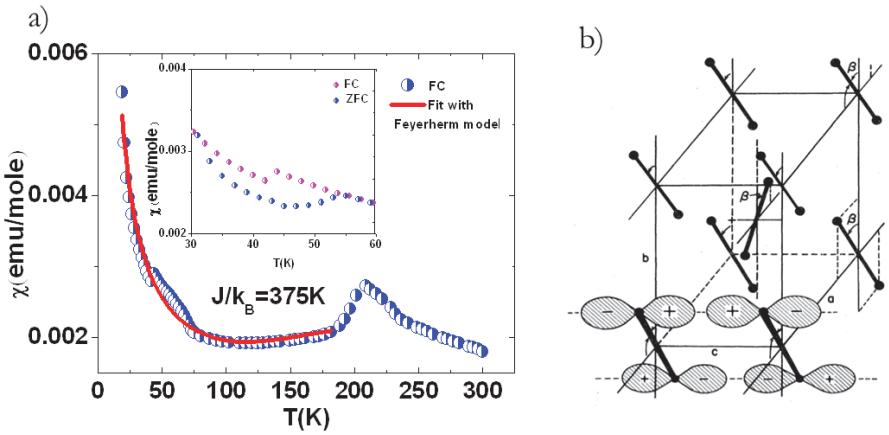

Figure 5.10: a) Low dimensional part of the magnetic susceptibility of polycrystalline NaO_2 fitted using an S=1/2 Heisenberg antiferromagnetic spin chain model [20]. The inset shows a zoomed view of the zero-field-cooled and field-cooled magnetic susceptibilities between 30 and 60 K. b) Proposed arrangement of singly occupied molecular orbitals in marcasite NaO_2, overlapping along the c-axis to form a spin chain (taken from [14]).

5.4 Summary and Conclusion

A new solution route to the synthesis of NaO_2 has been found, using a solvent mixture of 70% methylamine and 30% ammonia. The presence of ammonia in the mixture is required to dissolve Na metal, whereas methylamine suppresses the further side reaction of superoxide anions with the solvent. Using an ammonia-rich solution results in a novel superoxide-containing phase of composition $Na(O_2)_{1-x}(OH)_x$. It is expected that these conditions can be applied to the synthesis of other light alkali superoxides including lithium superoxide (LiO_2). Raman spectroscopy shows that $Na(O_2)_{1-x}(OH)_x$ is a mixed valent compound with the characteristic signature of four O-O stretching modes, as also observed for $K_xBa_{1-x}O_2$ in

Chapter 4. Similar to that system, the interaction strength between adjacent molecular oxygen ions in $Na(O_2)_{1-x}(OH)_x$ is moderate, allowing electron transfer to take place on a local level. A weak field-induced ferromagnetic component is observed in $Na(O_2)_{1-x}(OH)_x$ at low temperature and it is possible that double exchange occurs on local length scales. Sodium superoxide obtained in polycrystalline form by the solution method has been characterized and attempts have been made to address some of the unresolved issues regarding magnetism and structure. The magnetic ordering in the marcasite phase appears to be of short-range antiferromagnetic nature and the data are consistent with a one-dimensional spin chain model with exchange parameter J/k_B = -375K. This suggests strong orbital overlap and demonstrates that high magnetic ordering temperatures are in principle possible in the alkali oxides. It is still unclear from the current data whether long-range magnetic ordering sets in at low temperature, but two anomalies at 45 K and 60 K were observed and can be attributed to magnetic phase transitions. No crystallographic changes were observed in this temperature region. There appears to be a competing exchange pathway that favors ferromagnetic interactions, which become apparent in a small applied field at 2 K. It is likely that field can induce a partial reorientation of the dioxygen dumbbells, allowing the ferromagnetic exchange pathway to become more favorable.

Bibliography

[1] Zumsteg, A.; Ziegler, M.; Känzig, W.; Bosch, M. Physics of Condensed Matter 1974, 17, 267.

[2] Winterlik, J.; Fecher, G. H.; Jenkins, C. A.; Medvedev, S.; Felser, C.; Kuebler, J.; Muehle, C.; Doll, K.; Jansen, M.; Palasyuk, T.; Trojan, I.; Eremets, M. I.; Emmerling, F. Physical Review B 2009, 79, 214.

[3] Labhart, M.; Raoux, D.; Känzig, W.; Bosch, M. A. Physical Review B 1979, 20, 53.

[4] Kemeny, G.; Kaplan, T. A.; Mahanti, S. D.; Sahu, D. Physical Review B 1981, 24, 5222.

[5] Hesse, W.; Jansen, M.; Schnick, W. Progress in Solid State Chemistry 1989, 19, 47.

[6] Mahanti, S. D.; Khan, A. U. Solid State Communications 1976, 18, 159.

[7] Singh, P.; Gaur, N. K. Physics Letters A 2007, 371, 349.

[8] Stephanou, S. E.; Schechter, W. H.; Argersinger, W. J.; Kleinberg, J. Journal of the American Chemical Society 1949, 71, 1819.

[9] Andrews, L. Journal of Physical Chemistry 1969, 73, 3922.

[10] Känzig, W.; Labhart, M. Journal de Physique Colloques 1976, 37, C7.

[11] Ylvisaker, E. R.; Singh, R. R. P.; Pickett, W. E. Physical Review B 2010, 81, 180405R

[12] Riyadi, S.; Zhang, B.; de Groot, R. A.; Caretta, A.; van Loosdrecht, P. H. M.; Palstra, T. T. M.; Blake, G. R. Physical Review Letters 2012, 108, 217206.

[13] Kemeny, G.; Mahanti, S. D. Physical Review B 1979, 20, 2961.

[14] Mahanti, S. D.; Kemeny, G. Physical Review B 1979, 20, 2105.

[15] Watt, G. W. Chemical Reviews 1950, 46, 289.

[16] Bleif, H. -J.; Dachs, H. Acta Crystallographica Section A 1982, 38, 470.

[17] Hunter-Saphir, S. A.; Creighton, J. A. Journal of Raman Spectroscopy 1998, 29, 417.

[18] Bates, J. B.; Brooker, M. H.; Boyd, G. E. Chemical Physics Letters 1972, 16, 391.

[19] Keith, B. C.; Landee, C. P.; Valleau, T.; Turnbull, M. M.; Harrison, N. Physical Review B 2011, 84, 104442.

[20] Feyerherm, R.; Abens, S.; Günther, D.; Ishida, T.; Meißner, M.; Meschke, M.; Nogami, T.; Steiner, M. Journal of Physics: Condensed Matter 2000, 12, 8495.

Chapter 6

Non-stoichiometry and Anionogenic Magnetism in AO_{2-x} (A=Cs, K)

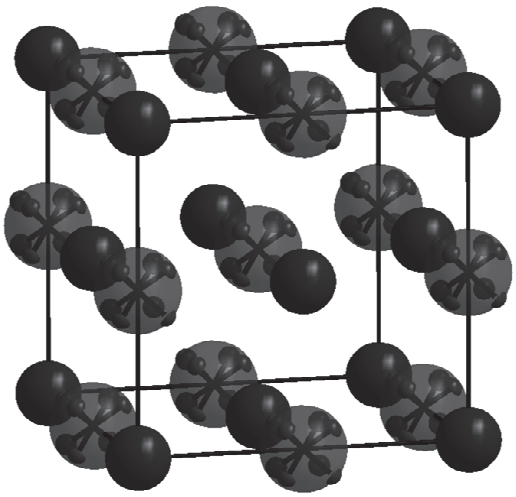

6.1 Introduction

Ionic solids comprising molecular oxygen ions, which contain unpaired electrons in the π^* antibonding level, are of interest because rather unusually, the anions are responsible for the physical properties [1-4]. As discussed in earlier chapters of this thesis, dioxygen anions can be stabilized by alkali metal cations giving ionic solids with compositions AO_2, A_2O_3 and A_2O_2 reported in the literature. In Chapters 3-5 it is discussed that mixing peroxide and superoxide anions can lead to a mixed valent state. Mixed valent phases in a series with non-integer number of valence electrons often express distinct physical properties that are different to the end members of the series. There are very few known alkali oxide mixed valent compounds. The best studied are Rb_4O_6 and Cs_4O_6, which show glassy magnetic behavior at low temperature explained in terms of spin frustration [5]. Mixed valency in alkali oxides can also be introduced by varying the oxygen content to make non-stoichiometric phases. The schematic phase diagram shown in Fig. 6.1 shows the possible stable forms of alkali oxides and their colors with increasing oxygen content.

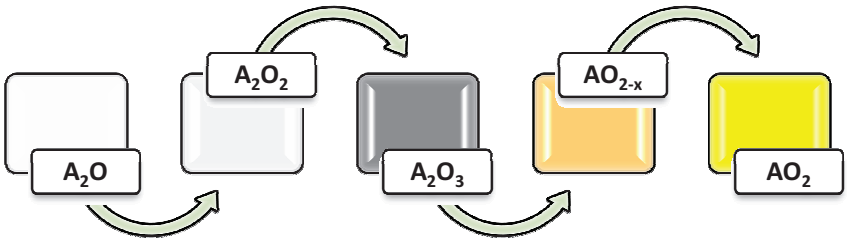

Figure 6.1: Possible stable forms of alkali oxides with increasing oxygen content.

The mixed valent alkali oxides in the series above can be represented as A_2O_3 and AO_{2-x}. The former are known for A = Rb, Cs. It is still unclear from the literature whether it is possible to synthesize K, Na and Li analogs. The deliberate introduction of non-stoichiometry is an alternative and perhaps more straightforward approach towards realizing novel

mixed valent alkali oxides. Thus far, the only reported non-stoichiometric AO_{2-x} phase is $RbO_{1.72}$ [6], which was prepared by the controlled heating of stoichiometric RbO_2 in vacuum. This thermal decomposition method might allow a range of AO_{2-x} compounds to be stabilized with oxygen stoichiometries lying between those of A_2O_3 and AO_2. It is well known from earlier reports that AO_2 can stabilize in two different structural forms (both based on rocksalt) at room temperature. RbO_2, CsO_2 and KO_2 adopt a body centered tetragonal form with space group I4/mmm in which the superoxide anions are aligned along the tetragonal axis. NaO_2 and possibly LiO_2 (whose existence is still under debate) adopt a cubic structure with space group Fm-3m in which the anion orientations are disordered. This disordered structure is found at high temperature in RbO_2, CsO_2 and KO_2 [1,4,7]. It is also adopted by $RbO_{1.72}$ at room temperature. Thus, it appears that the removal of oxygen from the rocksalt lattice to create vacancies leads to greater disorder in the orientation of the dioxygen dumbbells. The anions in $RbO_{1.72}$ become confined to a plane on cooling, involving a cubic to orthorhombic transition that should lift the degeneracy of the superoxide π^* orbitals (a Jahn-Teller (JT) transition). However, it appears that inhomogeneous domains can be formed during this process, depending on the cooling rate [14], which might involve separation of JT-distorted areas from non-JT-distorted regions. The magnetic properties of $RbO_{1.72}$ also depend on the cooling rate; ferromagnetic clusters are stabilized below 50 K for fast cooling [6]. This behavior is significantly different to either RbO_2 (antiferromagnetic below 15 K) or Rb_2O_3 (spin glass below $\sim$8 K) [5,8]. It is thus interesting to investigate the possibility of forming nonstoichiometric AO_{2-x} phases for the other alkali oxides, the synthesis of which is unclear form earlier reports [1].This chapter explores the above aspect of alkali oxides with the aim of better understanding the influence of mixed valency on magnetic properties.

6.2 Experimental

6.2.1 Synthesis

The synthesis of non-stoichiometric alkali oxides was unsuccessful by oxidation of the metal dissolved in liquid ammonia; AO_2 is in general directly obtained. The synthesis of AO_{2-x} was thus attempted using a two-part procedure involving the synthesis of stoichiometric AO_2 followed by controlled thermal decomposition. Although the solution synthesis of AO_2 has been discussed in some detail in earlier reports, the understanding of this process is incomplete. The thermal decomposition of AO_2 has been little studied. It is thus relevant here to look at both these reactions in detail to optimize the parameters involved. The procedures studied here are applicable to KO_{2-x}, RbO_{2-x} and CsO_{2-x}.

Step 1: Synthesis of alkali superoxides in liquid NH_3

The synthesis of alkali superoxides is best done by oxidation of the respective alkali metal in liquid ammonia solution. A certain quantity of metal is placed in a round bottom flask which is then attached to a vacuum line. Enough liquid ammonia is condensed into the flask to dissolve the metal. Oxygen gas is then supplied to the flask for oxidation of the metal solution, with continual stirring. A reaction temperature of -60 C to -80 C and an oxygen partial pressure of 750 mbar are maintained during the reaction process. A side reaction (Reaction 1) occurs in which the superoxide anions that are formed react with the ammonia solvent, and in a following step hydroxide and nitrite anions are formed. It is very important to minimize the occurrence of the side reaction in order to obtain samples of alkali superoxide that contain as little alkali hydroxide and nitrite as possible. The minimum amount of liquid NH_3 necessary to dissolve the metal completely should be condensed, and the reaction time should be as short as possible. The oxidation is essentially complete when a dark yellow colored solution is observed. The solvent is then evaporated by pumping. After complete evaporation of the solvent the precipitate left over in the flask will be dry

and can be used for further processing in Step 2 below. The reaction vessel and reaction set up is shown in Chapter 2 (Fig. 2.4).

Side reaction (ammonolysis of superoxide):

$$O_2^- + 2NH_3 \longrightarrow 2OH^- + 2\,NH_2^- \quad \text{.....(4)}$$

Molecular O_2 can then react with the amide intermediate:

$$2\,NH_2^- + 3/2O_2 \longrightarrow OH^- + NO_2^- + NH_3 \quad \text{.....(5)}$$

Step 2: Synthesis of AO_{2-x} by controlled thermal decomposition of AO_2

The AO_2 sample prepared in Step 1 is sealed in a glass tube and heated in a box furnace (Fig. 2.5). The decomposition temperature can be determined by TGA-DSC analysis performed in a dry argon atmosphere, as shown in Fig 6.2. The heating of AO_2 leads to successive transformations involving the loss of oxygen, apparent as weight loss in the TGA curves and as peaks in the DSC plots.

The multiple DSC peaks observed in the temperature range studied in Fig. 6.2 suggest that it might be possible to stabilize a range of oxygen deficient phases. The oxygen stoichiometry of the product is thus very sensitive to the temperature at which the sample is held. Furthermore, the decomposition reaction relies on the diffusion of oxygen out of the sample, hence the product obtained after a single heating cycle is inhomogeneous.

In order to perform controlled decomposition over the entire sample, several heating cycles are necessary with intermediate regrinding and resealing in glass tubes with the same volume. Heating for too long, or at too high a temperature, results in at least part of the sample being decomposed to the peroxide (A_2O_2). The samples studied in this chapter were obtained by heating CsO_2 and KO_2 at temperatures of 180 C and 300 C, respectively.

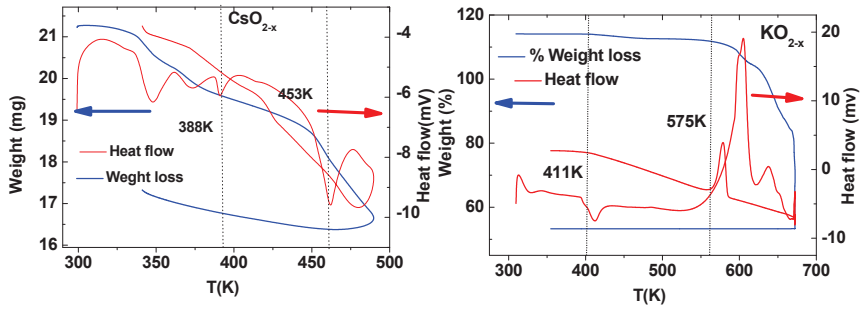

Figure 6.2: TGA-DSC plots of stoichiometric CsO_2 (left) and KO_2 (right).

For each sample 3 to 4 cycles of heating were carried out using a 5 mm diameter glass tube of length 4-5 cm containing 40 - 50 mg sample. Keeping to this mass and dimensions helps to obtain better control over the decomposition. The samples were nearly pure with traces of a secondary phase. Figure 6.2 shows DSC plots for both CsO_{2-x} and KO_{2-x}. For CsO_{2-x} the peak at 115 C indicates the formation of an initial CsO_{2-x} phase and preliminary X-ray diffraction measurements indicate a hexagonal structure.

However, this phase coexists with tetragonal CsO_2 and a cubic form of CsO_{2-x} and has not yet been characterized further. Figure 6.3 shows the X-ray diffraction pattern of the initial phase. Similarly, the DSC measurements on KO_2 also show the possible existence of a new phase forming at 138 C, which also needs further investigation.

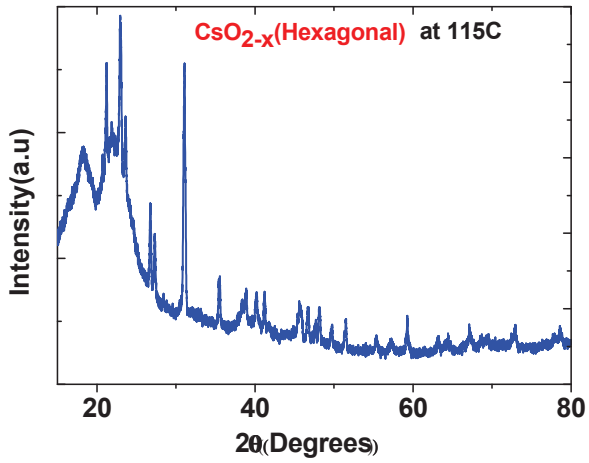

Figure 6.3: XRD pattern of possible new hexagonal nonstoichiometric phase of CsO_{2-x}, coexisting with tetragonal CsO_2 and cubic CsO_{2-x}.

6.3 Results and Discussion

As already discussed, AO_2 (A = K, Rb, Cs) adopt the body centered tetragonal (I4/mmm) structure at room temperature. The controlled thermal decomposition of these AO_2 leads to nonstoichiometric AO_{2-x} phases that adopt the disordered cubic structure with space group Fm-3m. RbO_{2-x} has previously been studied and is described in Ref. [6]. However, there are no reports of KO_{2-x} or CsO_{2-x} phases in the literature. Here the characterization of novel non-stoichiometric Cs and K oxides is discussed in detail.

6.3.1 Non-stochiometric CsO_{2-x}

The oxygen content of this phase was determined by performing TGA/DSC analysis on the sample in an oxygen atmosphere. Heating in oxygen will result in the oxidation of CsO_{2-x} back to stoichiometric CsO_2. The amount of oxygen absorbed, measured by the weight gain, allows the oxygen content

of CsO_{2-x} to be estimated. The data collected on heating to 50 C and holding under isothermal conditions for 2 h with continuous oxygen flow are shown in Fig. 6.4. The completion of oxidation is reflected by the end of weight gain in the TGA plot (a relatively small and steady weight gain is observed after 2 h, perhaps due to the absorption of water in the imperfectly sealed sample environment). By extrapolating the gentle weight gain curve after 2 h back to zero time (as indicated by the dashed line) and comparing with the initial sample weight, the amount of oxygen absorbed corresponded to a composition of $CsO_{1.87}$.

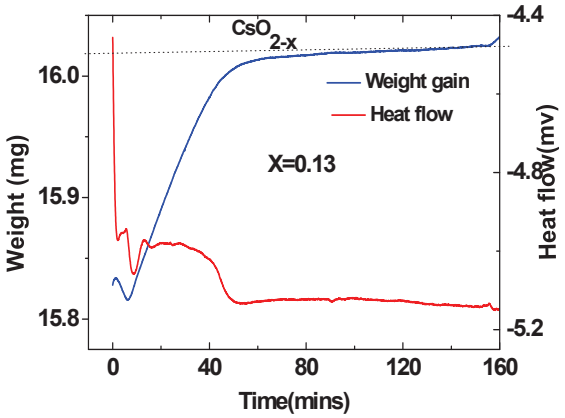

Figure 6.4: DSC/TGA plot of CsO_{2-x} heated at 50 C under isothermal conditions in an oxygen atmosphere.

$CsO_{1.87}$ adopts the cubic Fm-3m structure in which the oxygen dimers have essentially disordered orientations, perhaps with a preference for the [111] set of unit cell body diagonal axes. This structure is the same as the disordered pyrite structure of NaO_2 at room temperature (see Chapter 5). The refined structures of CsO_2 and $CsO_{1.87}$ are compared in Table 6.1.

XRD measurements on $CsO_{1.87}$ were also carried out at temperatures down to 17 K. The data were collected on warming. Fitted XRD patterns and the evolution of the lattice parameters are shown in Fig. 6.6. $CsO_{1.87}$

transforms to the I4/mmm structure over a broad temperature range starting at ∼270 K; the tetragonal phase remains down to 17 K. This is an order - disorder transition, where the anions become oriented along the tetragonal *c*-axis on cooling. At low temperature some of the XRD peaks become broadened (Fig. 6.6b), which might be due to the formation of orthorhombic domains of small length scale in which the superoxide anions are tilted and shifted to break the orbital degeneracy. This has been studied in stoichiometric KO_2, where the tetragonal structure is an average that is mimicked by the superposition of orthorhombic domains. This type of nanostructure cannot easily be probed by X-ray powder diffraction. The refined structural parameters of $CsO_{1.87}$ in the tetragonal model are given in Table 6.1.

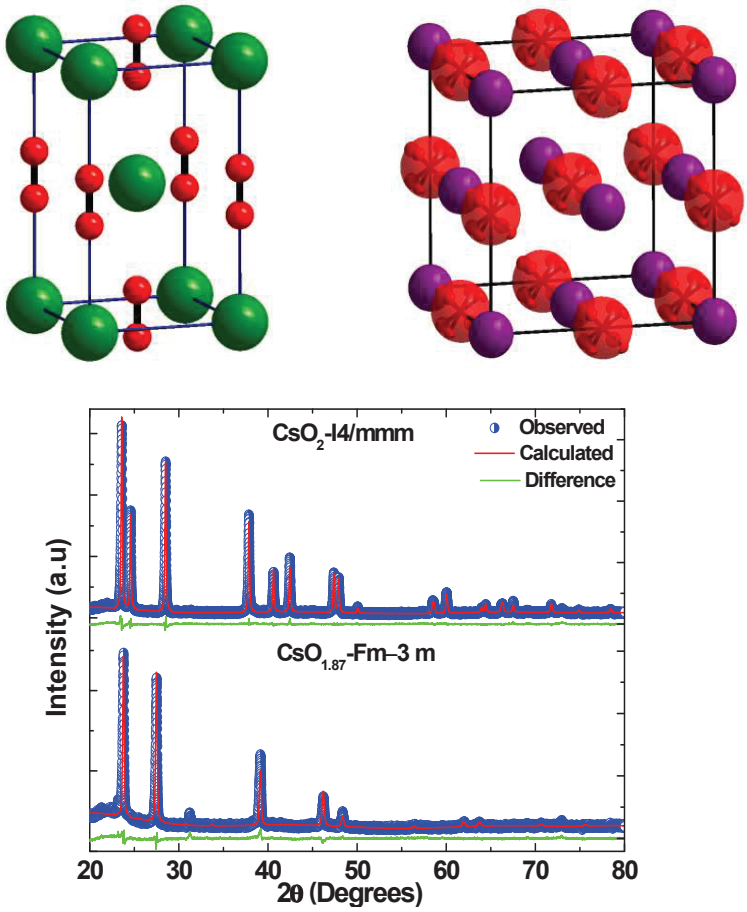

Figure 6.5: Room temperature structures of CsO_2 (I4/mmm, top left) and $CsO_{1.87}$ (Fm-3m, top right) and their corresponding XRD patterns.

Sample	Temperature	a	b	c
CsO_2(I4/mmm)	300K	4.4687(1)	4.4687(1)	7.9195(1)
CsO_2(Immm)	20K	4.3857(2)	4.4101(2)	7.3367(2)
$CsO_{1.87}$(Fm-3m)	300K	6.546(3)	6.546(3)	6.546(3)
$CsO_{1.87}$(I4/mmm)	<18K	4.3913(2)	4.3913(2)	7.2164(5)

Table 6.1: Lattice parameters of $CsO_{1.87}$ and CsO_2.

Complementary to the XRD data, the structural order to disorder transition is also reflected in the low temperature DSC measurements in Fig. 6.7, where the labels 1, 2 and 3 represent successive heating, cooling and heating. The broad DSC peaks at 243 K on cooling indicate the transition temperature. The main DSC peak is observed at 222 K on heating. The difference in transition temperatures observed on cooling and heating can be attributed to the energy barrier involved in the cooperative reorientation of oxygen dumbbells. It is possible that the transition temperature could depend on the cooling/heating rate, as observed for $RbO_{1.72}$ [6].

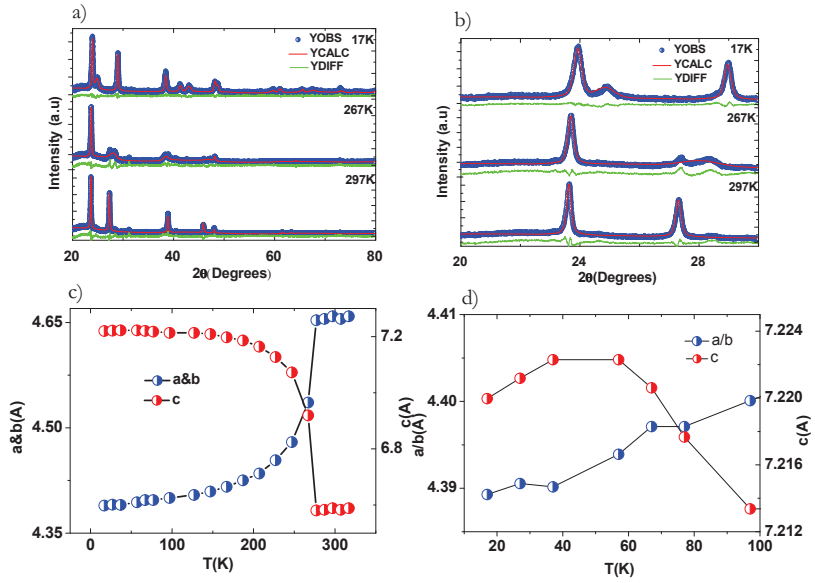

Figure 6.6: (a) and (b) Fitted XRD patterns of $CsO_{1.87}$ at different temperatures. (c) and (d) Lattice parameter evolution with respect to temperature.

The nature of the dioxygen anions was probed by the Raman spectroscopy measurements shown in Fig. 6.8. The peaks observed at 1134 cm^{-1} for both CsO_2 and $CsO_{1.87}$ are characteristic of the O-O stretching

mode for the superoxide anion. The peak is broader in $CsO_{1.87}$, reflecting the disorder in the anion orientations. There is also a very weak peak at 1043 cm^{-1}, which as discussed in Chapter 4 can be attributed to the out-of-phase stretching of superoxide-like anions in a mixed valent compound. Assuming that no Cs vacancies are present, ∼7% of the anions in $CsO_{1.87}$ must nominally be peroxide in order to achieve charge balance, which makes $CsO_{1.87}$ a mixed valent material.

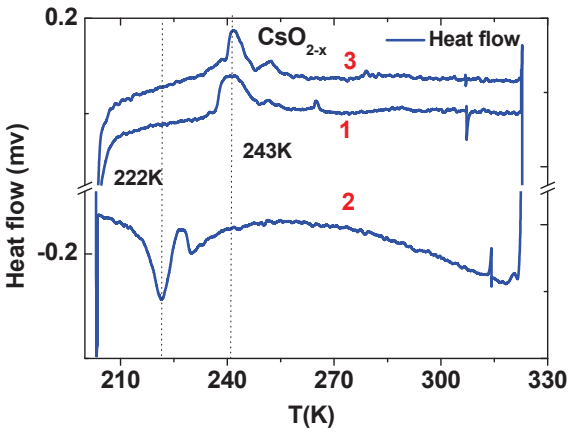

Figure 6.7: Low temperature DSC analysis of $CsO_{1.87}$. The sample was initially heated (1), then cooled(2) and heated again (3).

The presence of both the main "superoxide" mode at 1134 cm^{-1} and a weak "out of phase" mode at ∼1030 cm^{-1} might be a signature of coupled anions between which charge transfer takes place. By a symmetry analysis of tetragonal CsO_2, the allowed modes for Cs (site symmetry 4/mmm) and O (4mm) are obtained as:

$$\Gamma_{op}(4/\mathrm{mmm}) = \mathrm{A_{2u}} + \mathrm{E_u}$$

$$\Gamma_{op}(4\mathrm{mm}) = \mathrm{A_{1g}} + \mathrm{A_{2u}} + \mathrm{E_g} + \mathrm{E_u}$$

For $CsO_{1.87}$ (Fm-3m), the possible modes for O will be:

$$\Gamma_{op}(\text{-3m}) = A_g + E_g + 3F_g + 2A_u + 2E_u + 5F_u$$

The A_g and E_g components are Raman active. The observed mode at 1134 cm^{-1} likely consists of two components (stretching modes A_g and F_g). Phonon modes were not investigated in this work.

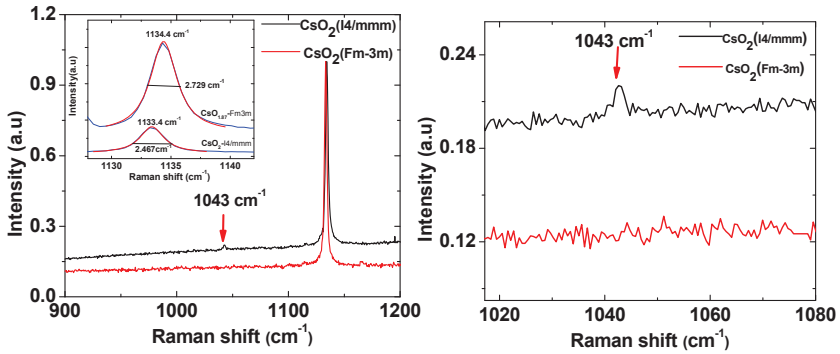

Figure 6.8: Raman spectra of both CsO_2 and $CsO_{1.87}$ at room temperature.

Magnetic Properties

Figure 6.9 shows the magnetic susceptibility and inverse susceptibility as a function of temperature for $CsO_{1.87}$. The inverse susceptibility shows a change in slope near the structural phase transition at ∼240 K. Curie-Weiss fits were performed on the linear regions above and below the transition, indicated by the labels 1 and 2 in Fig. 6.9. The effective moment of 1.67 μ_B in the high temperature region is slightly smaller than the spin-only value of 1.73 μ_B that would expected for stoichiometric NaO_2, which is a spin 1/2 system. In general, there is a significant orbital contribution in AO_2 that increases the effective paramagnetic moment to ∼2.0 μ_B , so the current value of 1.67 μ_B is reasonable considering the nominal superoxide content of 87.5% in $CsO_{1.87}$. The effective moment in the tetragonal regime below 240 K is significantly lower, 1.33 μ_B. This might indicate that short

range antiferromagnetic interactions (the Weiss constant is negative in both fitting regions) between spins become significant here.

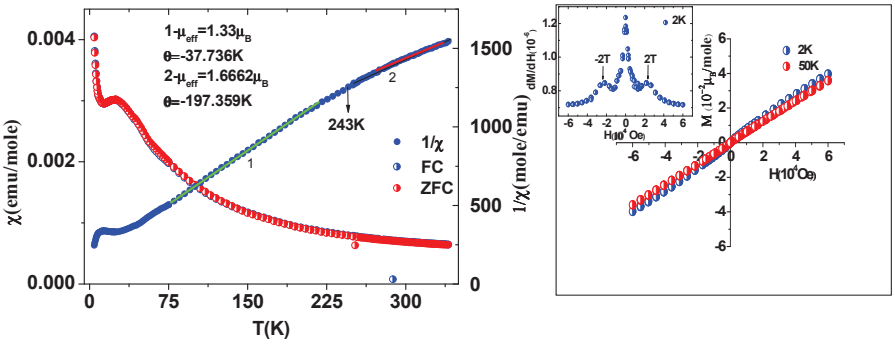

Figure 6.9: Left: field-cooled (blue data points) and zero-field-cooled (red data points) magnetic susceptibility versus temperature for $CsO_{1.87}$, measured in 1000 Oe. Curie-Weiss fits in two temperature regimes are shown (1 and 2, see text for explanation). Right: magnetization versus applied field at temperatures of 2K and 50K. The inset shows the derivative of the magnetization at 2K.

On further cooling, a broad peak in the magnetic susceptibility is apparent at 26 K, which is similar to that observed in stoichiometric CsO_2 [9] and might indicate low dimensional short range ordering. The susceptibility in the low temperature region was fitted using a Heisenberg square lattice model as discussed below. The fit yielded the exchange parameter J/k_B = 32.1 K, which is a bit higher than the value of 20 K for stoichiometric CsO_2. This model fits the curve reasonably well up to ∼75 K. In contrast to stoichiometric CsO_2, no obvious anomoly in the susceptibility curve is apparent at temperatures above the maximum. Below ∼7K a paramagnetic tail is observed, which might be due to unpaired spins at chain ends. This paramagnetic tail was fitted using the Curie law and yielded a Curie constant of 0.032 which corresponds to an effective moment of 0.45 μ_B. The magnetization versus field measurements in Fig. 6.9 indicate that antiferromagnetic

ordering remains down to 2 K. However, this is likely to be short-range in nature. Unlike in CsO_2, there is no obvious anomaly in the susceptibility below the broad maximum that might indicate a crossover to 3D ordering, thus the spin chain in $CsO_{1.87}$ might persist down to low temperature. The weak anomaly at 2 T might indicate a small reorientation of the oxygen dumbbells by the applied magnetic field.

Low dimensional antiferromagnetic spin chain

The following section presents a detailed analysis of the susceptibility maximum centered at 26 K. A similar feature in CsO_2 corresponds to a 1D spin chain induced by orbital ordering. Because the spins associated with dioxygen dumbbells are oriented orthogonal to the molecular axis, magnetic interactions in alkali oxides are strongly coupled to the anion orientation and to the geometrical arrangement of the half-filled π^* orbitals.

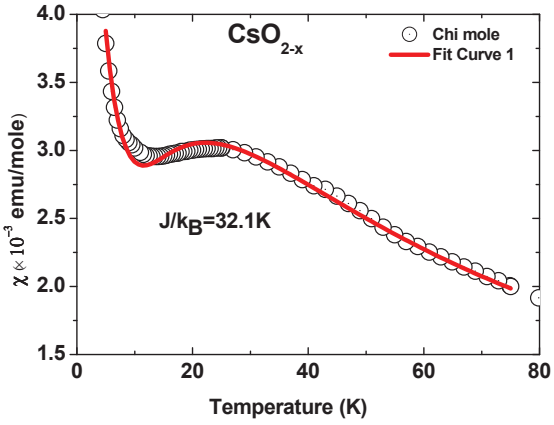

Figure 6.10: Fit of the broad field-cooled magnetic susceptibility maximum of $CsO_{1.87}$ to a 1D spin chain model (see text), including a term describing the low-temperature paramagnetic tail using the Curie law.

The spins in alkali superoxides can rotate in the plane orthogonal to the molecular axis. Since EPR shows only a moderate anisotropy of the

g-tensor for stoichiometric CsO_2 [9, 20], it can be considered as an isotropic spin system (Heisenberg). Here the same assumption is made for $CsO_{1.87}$.

The temperature range 15K to 60K fits reasonably well with the 1D AFM Heisenberg spin-1/2 chain model with an added Curie contribution for the low-temperature tail. The observed maximum in the susceptibility plot can be fitted using the model of Feyerherm et al. [11]:

$$(1+x)^n = 1 + \frac{Ng^2\mu_B^2}{4(2J)t}\,\frac{(t^3+0.08516t^2+0.23351t)}{(t^3+0.73382t^2+0.13969t+0.53568)} \qquad \text{where } t = \frac{k_B T}{2J}$$

This is based on the formulation for a S=1/2 Heisenberg AFM chain by Bonner and Fisher in Ref. [12]. The best fit to the maximum is shown in Fig. 6.10, which gave $J/k_{\mathrm{B}} = 32.1$ K and $C = 0.257$. The low temperature range gives a Curie constant of 0.0412 emu K/mole. This corresponds to 11% uncoupled spins, possibly at the chain-ends. The average chain length is approximately 20 spins.

6.3.2 Non-stoichiometric KO_{2-x}

The oxygen stoichiometry of the KO_{2-x} compound was estimated using TGA analysis in an oxygen atmosphere in similar fashion to CsO_{2-x}. The KO_{2-x} sample was heated to 50 C and kept at this temperature for two hours while oxygen was supplied. The results are shown in Fig. 6.11. Weight gain essentially stopped after 2 h. The amount of oxygen absorbed corresponded to a composition of $KO_{1.86}$. This oxygen stoichiometry can be varied depending on the duration of the thermal decomposition step and the quantity of sample used in the decomposition. However, full characterization was performed only for the $KO_{1.86}$ sample.

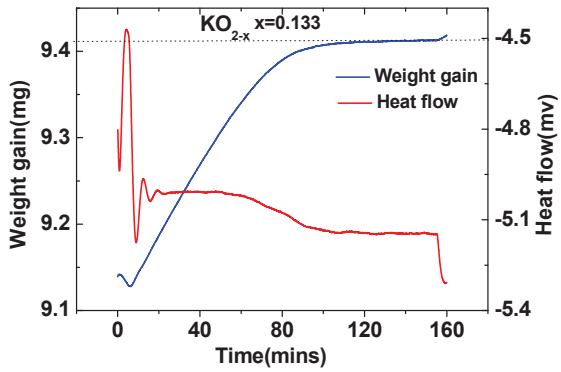

Figure 6.11: DSC/TGA analysis of $KO_{1.86}$ heated to 50 C in oxygen.

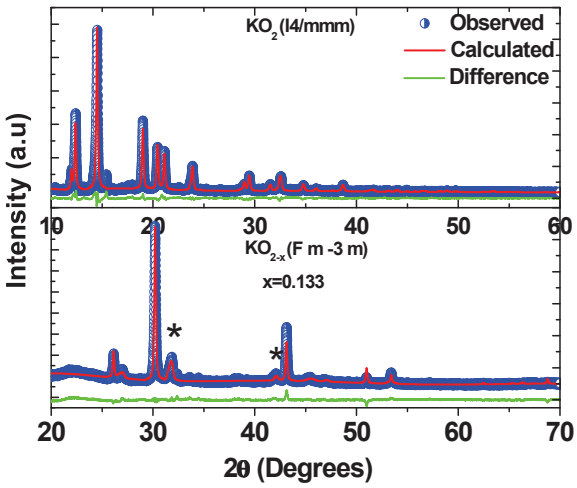

Figure 6.12: X-ray diffraction patterns of stoichiometric KO_2 (Mo Kα X-ray source) and $KO_{1.86}$ (Cu Kα X-ray source).

Figure 6.12 shows fitted XRD patterns at room temperature for $KO_{1.86}$ and stoichiometric KO_2 (body centered tetragonal I4/mmm structure). Similar to $CsO_{1.87}$, $KO_{1.86}$ stabilizes in the disordered Fm-3m structure (Fig.

6.5). A small fraction of a second phase with the tetragonal structure coexists with cubic $KO_{1.86}$, the peaks of which are indicated by (*) labels in Fig. 6.12.

Sample	T(K)	a	b	c
KO_2(I4/mmm)	At 300K	4.4687(4)	4.0330(4)	6.6990(5)
KO_{2-x}(Fm-3m)	At 300K	5.966(3)	5.966(3)	5.966(3)
KO_{2-x}(I4/mmm)	20K	3.941(1)	3.941(1)	6.6594(5)

Table 6.2: Lattice parameters of $KO_{1.86}$ and KO_2.

Temperature dependent XRD patterns of $KO_{1.86}$ are shown in Fig. 6.13. These data were collected on warming. Just below room temperature the disordered cubic phase begins to transform to the ordered tetragonal structure in which the anions are aligned along the tetragonal *c*-axis. The two phases coexist over a broad temperature region and the transition is complete by ∼220 K. However, refinement of the low temperature XRD patterns using the body centered tetragonal (I4/mmm) model gave a bad fit. This suggests that the tetragonal structure might only be an average picture, similar to KO_2 where orthorhombic Jahn-Teller distorted nanodomains involving short-range correlated shifts and tilts of the anions are thought to mimick tetragonal symmetry. The peaks of $KO_{1.86}$ are broad at low temperature, consistent with the presence of small domains that are probably formed to lift the orbital degeneracy. Low temperature DSC measurements were carried out on $KO_{1.86}$ and are shown in Fig. 6.14. Here the labels 1, 2 and 3 represent successive heating, cooling and heating. A peak is observed in both of the heating curves at 235 K (slightly lower for the cooling curve). A second peak is observed at 274 K and 283 K in the heating curves. The upper and lower peaks in the heating curves likely correspond to the onset and completion of the order-disorder transformation, which is consistent with Fig. 6.13b in which a broad region of phase coexistence is apparent, indicating a first-order transition. The variation in peak positions over the

three scans suggests that the phase transition region might be dependent on thermal history.

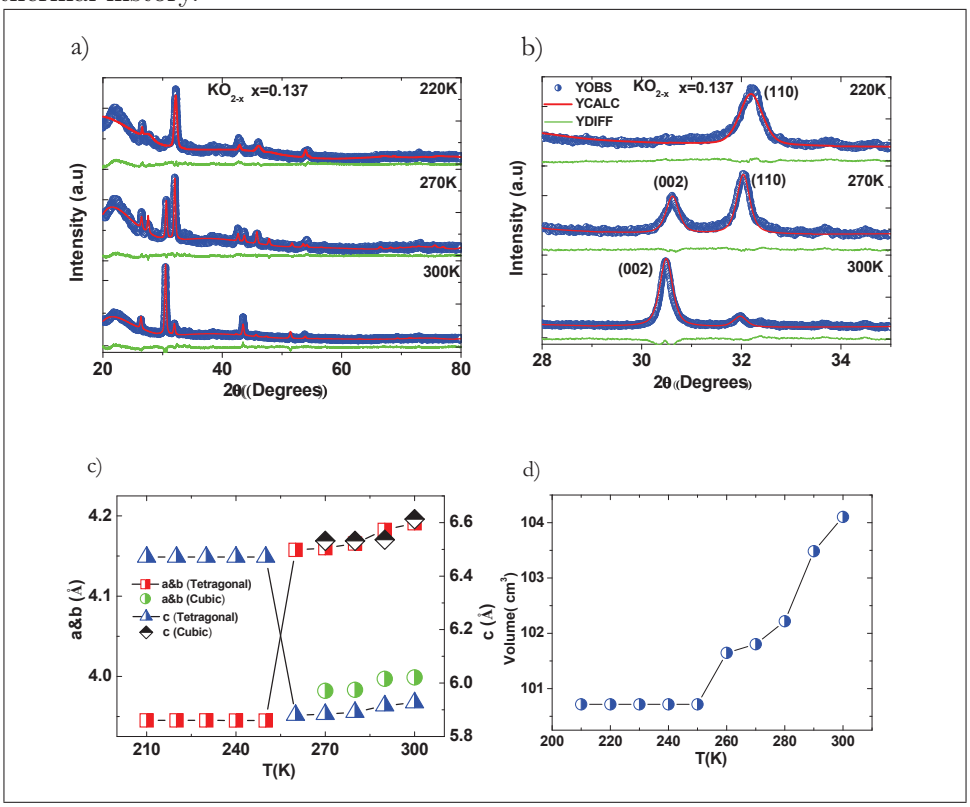

Figure 6.13: (a,b) Fitted XRD patterns of $KO_{1.86}$ at different temperatures. (c,d) Evolution of lattice parameters and volume with temperature.

Figure 6.15 shows Raman spectra of $KO_{1.86}$ and KO_2 acquired at room temperature in the frequency region where the O-O stretching modes of the oxygen dimers appear. The symmetry analysis described previously for CsO_2 is applicable to KO_{2-x}. The mode at ~1145 cm^{-1} is approximately five times broader for $KO_{1.86}$ than for KO_2, which must reflect significant orientational disorder of the oxygen anions. However, the broadening is much more extreme than in the case of $CsO_{1.87}$ (Fig. 6.8), thus there might be an additional source of disorder in the structure of the potassium analogue. In addition to the main mode at 1145 cm^{-1}, an additional sharper

mode is apparent at 1065 cm^{-1}.

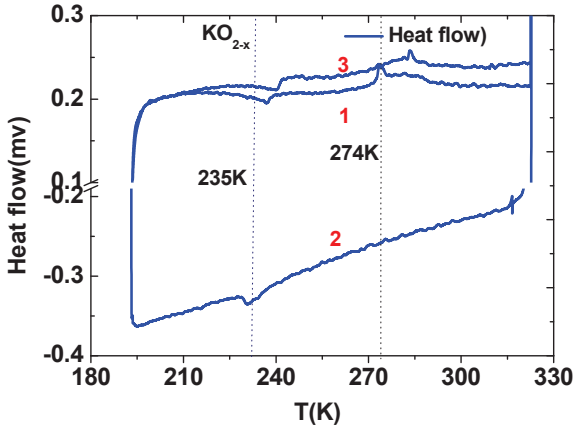

Figure 6.14: Low temperature DSC analysis of $KO_{1.86}$ measured on heating (1), subsequent cooling (2) then heating again (3).

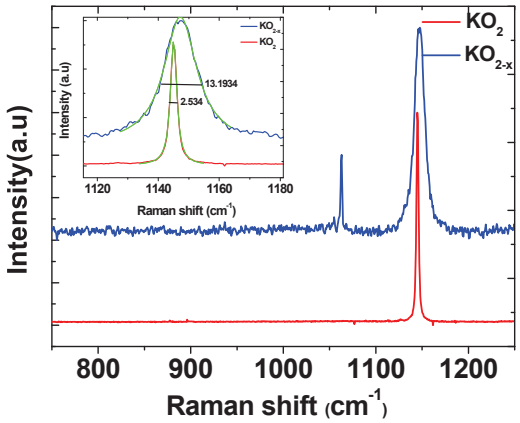

Figure 6.15: Room temperature Raman spectra of both $KO_{1.86}$ and stoichiometric KO_2. The inset shows fits of the main peaks using Pseudo–Voigt functions.

As discussed for $CsO_{1.87}$ and in Chapter 4, this mode is a signature of mixed valent compounds and corresponds to the out-of-phase stretching mode for ions of superoxide character. The presence of this mode indicates that significant charge transfer can occur locally between neighboring anions.

Magnetic Properties

Magnetic susceptibility versus temperature and magnetization versus field curves for $KO_{1.86}$ are shown in Fig. 6.16. The data were taken on warming after fast cooling the sample from room temperature to 25 K in field or in zero field. In contrast to stoichiometric KO_2, which exhibits long-range antiferromagnetic ordering below 7 K [4], $KO_{1.86}$ shows no signature of long-range ordering down to 2 K. The low temperature downward deviation of the inverse susceptibility from Curie-Weiss behavior suggests that short-range antiferromagnetic interactions are present. Weak ferromagnetic interactions are induced by an applied field at 5 K, as shown by the narrow hysteresis loop in Fig. 6.16b. From a Curie-Weiss fit above 100 K, an effective magnetic moment of $1.65\mu_B$ and a Weiss temperature of -33 K were extracted. The effective moment is in good agreement with that expected for the composition $KO_{1.86}$, where $\sim$93% of the anions are nominally magnetic superoxide and $\sim$7% are non-magnetic peroxide to balance the positive charge of K^+.

The type of magnetic ordering in alkali oxides is strongly influenced by the orientational ordering of the anions, where the spins are orthogonal to the molecular axis. It is somewhat surprising that $KO_{1.86}$ shows only a small deviation from paramagnetic behavior down to 2 K. The parent phase KO_2 shows 3D antiferromagnetic ordering, although the crystal structure is different with a monoclinic distortion where the anions are tilted far from the pseudo-tetragonal c-axis. However, $CsO_{1.87}$ exhibits low-dimensional ordering and $RbO_{1.72}$ shows ferromagnetic clusters and a large degree of glassy behavior when cooled fast [6].It might be the case that in $KO_{1.86}$ the

crystal structure is unfavorable for 3D magnetic ordering. From the XRD data it appears that the low temperature crystal structure is only tetragonal on average and is likely made up of nanodomains.

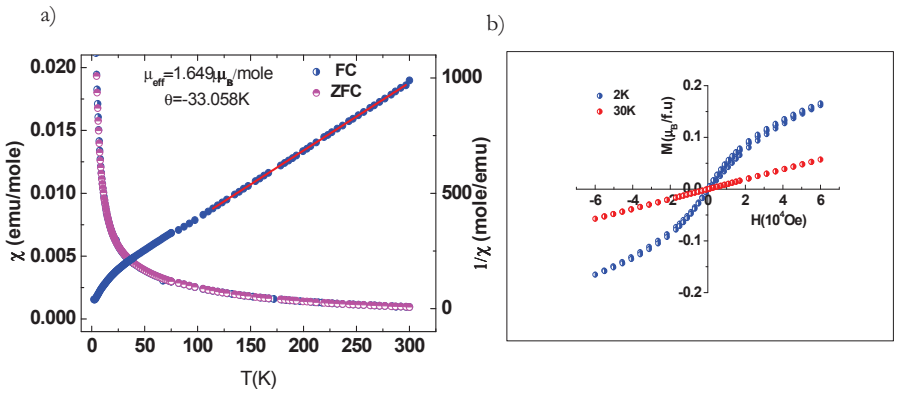

Figure 6.16: a) Field-cooled (FC) and zero-field-cooled (ZFC) magnetic susceptibility and inverse susceptibility versus temperature for $KO_{1.86}$ measured on warming in a field of 1000 Oe. (b) Magnetization (M) versus applied magnetic field measured at 2 K and 30 K.

These might be inhomogeneous or too small for long-range ordering to develop, a situation that is likely to be similar to $RbO_{1.72}$ when slow cooled [6]. The effect of cooling rate on the structural and magnetic properties of $KO_{1.86}$ has not been investigated, but the DSC data in Fig. 6.14 show that the thermal history influences the cubic-tetragonal phase transition temperature.

6.4 Summary

In this chapter it is demonstrated that, similar to $RbO_{1.72}$ that was studied earlier, non-stoichiometric systems with compositions $CsO_{1.87}$ and $KO_{1.86}$ can also be stabilized by thermal decomposition of their respective stoichiometric superoxide phases. All three materials adopt the disordered pyrite

(Fm-3m) structure at room temperature. However, their low temperature structures differ. In $RbO_{1.72}$ the dioxygen anions become oriented in a plane in a transition that strongly depends on cooling rate; ferromagnetic ordering in clusters is observed for fast cooled samples whereas slow cooled samples show little deviation from paramagnetic behavior [6]. $CsO_{1.87}$ becomes tetragonal below ∼240 K where the anions become ordered parallel to the c-axis. A one-dimensional antiferromagnetic spin chain is formed with $J/k_B = 32$ K, similar to the parent phase CsO_2. However, unlike CsO_2 there is no signature of 3D antiferromagnetic ordering in the ground state, thus it appears that the spin chain is more robust in the non-stoichiometric phase. By analogy with CsO_2, it is expected that the spin chain in $CsO_{1.87}$ is driven by a particular type of orbital ordering involving lower symmetry than tetragonal, but better structural data would be required to probe this in detail. $KO_{1.86}$ also becomes tetragonal below ∼220 K; the precise transition temperature seems to depend on thermal history, an aspect that needs to be studied further. Unlike $CsO_{1.87}$, no signature of magnetic ordering is observed down to 2 K. It appears that the tetragonal structure is an average picture and there are likely to be nanodomains of lower symmetry. Further structural studies would be required to understand why magnetic ordering is suppressed. Raman spectroscopy suggests that both $CsO_{1.87}$ and $KO_{1.86}$ can be considered as mixed-valent materials. The anion vacancies require that each anion possesses a non-integer number of valence electrons for charge balance, and the Raman spectra exhibit signatures of local charge transfer between neighboring anions, to a greater extent in $KO_{1.86}$ where the unit cell is more compressed and the anions are in closer proximity to each other. The deliberate introduction of non-stoichiometry in alkali superoxides is thus a promising route towards novel mixed-valent materials. It is likely that the oxygen composition can be varied by altering the conditions used in the thermal decomposition step of the synthesis, perhaps leading to further novel phases. This aspect should be explored in the future.

Bibliography

[1] Hesse, W.; Jansen, M.; Schnick, W. Progress in Solid State Chemistry 1989, 19, 47.

[2] Smith, H. G.; Nicklow, R. M.; Raubenheimer, L. J; Wilkinson, M. K. Journal of Applied Physics 1966, 37, 1047.

[3] Volnianska, O.; Boguslawski, P. Journal of Physics: Condensed Matter 2010, 22, 073202.

[4] Labhart, M.; Raoux, D.; Känzig, W.; Bosch, M. A. Physical Review B 1979, 20, 53.

[5] Winterlik, J.; Fecher, G. H.; Jenkins, C. A.; Medvedev, S.; Felser, C.; Kuebler, J.; Muehle, C.; Doll, K.; Jansen, M.; Palasyuk, T.; Trojan, I.; Eremets, M. I.; Emmerling, F. Physical Review B 2009, 79, 214.

[6] Riyadi, S.; Giriyapura, S.; de Groot, R. A.; Caretta, A.; van Loosdrecht, P. H. M.; Palstra, T. T. M.; Blake, G. R. Chemistry of Materials 2011, 23, 1578.

[7] Känzig, W.; Labhart, M. Journal de Physique Colloques 1976, 37, C7.

[8] Winterlik, J.; Fecher, G. H.; Felser, C.; Muehle, C.; Jansen, M. Journal of the American Chemical Society 2007, 129, 6990.

[9] Riyadi, S.; Zhang, B.; de Groot, R. A.; Caretta, A.; van Loosdrecht, P. H. M.; Palstra, T. T. M.; Blake, G. R. Physical Review Letters 2012, 108, 217206.

[10] Keith, B. C.; Landee, C. P.; Valleau, T.; Turnbull, M. M.; Harrison, N. Physical Review B 2011, 84, 104442.

[11] Feyerherm, R.; Abens, S.; Günther, D.; Ishida, T.; Meißner, M.; Meschke, M.; Nogami, T.; Steiner, M. Journal of Physics: Condensed Matter 2000, 12, 8495.

[12] Bonner, J. C.; Fisher, M. E. Physical Review 1964, 135, A640.

Summary and conclusion

This thesis shows that the magnetic properties of alkali oxides, which arise from the p-orbitals of dioxygen anions, share many characteristics with much more widely studied d- and f-electron-based magnetic materials. The work presented here focuses on the synthesis and properties of alkali oxides containing mixed valent dioxygen anions. These materials have oxygen valence states that are intermediate between superoxide (O_2^-) and peroxide (O_2^{2-}). Mixed valency in alkali oxides is an aspect that until now has not been explored in the scientific literature.

Chapter 1 presents a summary of previous studies on magnetic alkali oxides and gives an overview of which compounds exist and what is known about their structural and magnetic properties. The magnetic exchange interactions relevant to alkali oxides are discussed and a general background to the concept of mixed valency and charge transfer in solid materials is presented.

The high sensitivity of alkali oxides to moisture in air requires sophisticated synthesis and handling procedures in controlled atmosphere. These procedures are described in detail in Chapter 2 and at the start of each subsequent chapter. Chapter 2 also describes the techniques that are used to characterize the chemical and physical properties of the synthesized compounds.

In Chapter 3 it is shown that a range of mixed valent $K_xBa_{1-x}O_2$ com-

pounds can be stabilized by the reaction of KO_2 with $Ba(NO_3)_2$ in liquid ammonia. The magnetic superoxide content can be varied up to a maximum of x = 0.412. X-ray and neutron diffraction suggest that there is no long-range ordering of the K^+ and Ba^{2+} cations and thus no charge ordering of discrete O_2^- and O_2^{2-} anions. The magnetic properties, which are similar for all compounds in the composition range studied, are then discussed. Below ∼40 K the samples exhibit signatures of competing antiferromagnetic (AFM) and ferromagnetic (FM) interactions, and below 5K FM interactions become more prominent in applied fields. This suggests that the samples are inhomogeneous and are comprised of nanodomains or clusters with locally different magnetic exchange interactions. The nature of the magnetic exchange interactions between two neighboring dioxygen anions is determined by their local cation coordinations. Slow spin dynamics are also observed in the samples. A weak dependence of the magnetization on cooling rate is observed and thermoremanent magnetization measurements show that in an applied field an equilibrium state is achieved on the timescale of several hours. This feature of $K_xBa_{1-x}O_2$ arises both from glassy behavior due to competing magnetic interactions and from the difficulty of reorienting spins in an applied field, which requires reorientation of the dioxygen anions themselves and involves an energy barrier. $K_xBa_{1-x}O_2$ thus exhibits a delicate balance between collective elastic interactions due to anion reorientation and magnetic interactions determined by the local cation environment.

In Chapter 4 Raman spectroscopy is performed on the $K_xBa_{1-x}O_2$ samples synthesized and studied in Chapter 3. The spectra are explained with the help of density functional theory (DFT) calculations, which suggest that there is significant coupling between neighboring oxygen ions. This coupling is associated with a significant degree of charge transfer. Based on the well-known classification of mixed-valent systems by Robin and Day, $K_xBa_{1-x}O_2$ lies at the border between Class II and Class III where the coupling is moderate. In these compounds the redox centers are separated by an energy barrier that can be overcome by external stimuli. In $K_xBa_{1-x}O_2$ it

appears that such stimuli include light and lowering of pressure. Increasing the power of the Raman laser leads to a redistribution of spectral weight that corresponds to enhanced charge transfer. When the power is reduced, the spectral weight shifts back to its original distribution. The reversible nature of this effect suggests that light induces a purely electronic transition. It is proposed that illumination with the laser populates an excited state in which an electron in the π^* level of the dioxygen anion is promoted to the higher σ^* level. The resulting hole in the π^* level increases the probability of electron transfer from a π^* orbital of a nearest-neighbor anion. This process appears to be enhanced even more in vacuum, an observation that will require further study to understand. With exposure times to the laser light of several hours, some of the Raman peaks become sharper and the fine structure on these peaks becomes better resolved. This implies that the local chemical environments of the anions become better defined, which might be a result of light-induced cationic reordering.

In Chapter 5 a new route to the synthesis of NaO_2 that avoids high pressure is described. The key factor is to use a solvent mixture of 70% methylamine and 30% ammonia. A high concentration of methylamine suppresses a side reaction of superoxide anions with the ammonia solvent. Attempts to resolve some of the unresolved questions regarding the magnetic properties of NaO_2 are made. The magnetic ordering in the marcasite phase appears to be of short-range AFM nature and the magnetic susceptibility data are fitted to a one-dimensional spin chain model with an exchange parameter J/k_B = -375 K. This suggests strong overlap of the superoxide p-orbitals and demonstrates that high magnetic ordering temperatures are in principle possible in the alkali oxides. It is still unclear from the current data whether long-range magnetic ordering sets in at low temperature, but two anomalies in the susceptibility at 45 K and 60 K are observed and can be attributed to magnetic phase transitions. At low temperature there appears to be a competing exchange pathway that favors FM interactions when a small magnetic field is applied. It is likely that field can induce a partial reorientation of the dioxygen dumbbells, allowing the FM exchange

pathway to become more favorable. The synthesis of a novel solid solution $Na(O_2)_{1-x}(OH)_x$ in ammonia is also reported in Chapter 5. Raman spectroscopy shows that this is a mixed valent compound, with a characteristic spectrum of oxygen-oxygen stretching modes similar to that observed for $K_xBa_{1-x}O_2$ in Chapter 4. Similar to that system, the electronic coupling between adjacent dioxygen anions in $Na(O_2)_{1-x}(OH)_x$ is moderate, allowing electron transfer to take place on a local level. Although this compound exhibits predominantly AFM interactions without long-range order, weak field-induced ferromagnetism is observed at low temperature. This suggests that double exchange occurs on local length scales.

In Chapter 6 it is demonstrated that decreasing the oxygen stoichiometry of alkali superoxides by controlled thermal decomposition can induce mixed valence. Compounds with the compositions $CsO_{1.87}$ and $KO_{1.86}$ are synthesized and their structural and magnetic properties are investigated. Both materials adopt the cubic disordered pyrite structure at room temperature. $CsO_{1.87}$ becomes tetragonal below 240 K where the anions become ordered parallel to the c-axis. A similar transition occurs between ∼230 K and ∼280 K in $KO_{1.86}$ and involves phase coexistence, the extent of which depends on thermal history. The magnetic susceptibility of $CsO_{1.87}$ indicates that a one-dimensional AFM spin chain is formed with J/k_B = -32 K, which is slightly higher than in the parent phase CsO_2. The oxygen vacancies lead to a more compressed unit cell than CsO_2 and probably to a greater overlap of the orbitals responsible for the one-dimensional AFM exchange. However, unlike CsO_2 there is no signature of 3D AFM ordering in the ground state, thus it appears that the spin chain is more robust in the non-stoichiometric phase. In $KO_{1.86}$ no signature of magnetic ordering is observed down to 2 K. Further studies are required in order to understand why magnetic ordering is suppressed. Raman spectroscopy suggests that both $CsO_{1.87}$ and $KO_{1.86}$ can be considered as mixed-valent materials. The anion vacancies require that each anion possesses a non-integer number of valence electrons for charge balance, and the Raman spectra exhibit signatures of local charge transfer between neighboring anions. This is observed

to a greater extent in $KO_{1.86}$ where the unit cell is more compressed and the anions are in closer proximity to each other. The deliberate introduction of non-stoichiometry in alkali superoxides is thus a promising route towards novel mixed-valent materials.

Samenvatting en conclusies

Dit proefschrift laat zien dat de magnetische eigenschappen van alkali-oxides, ten gevolge van de p-orbitalen van di-zuurstof anionen, overeenkomen met die van verbindingen die de veel meer bestudeerde d- en f-elektron-blok elementen bevatten. Dit onderzoek richt zich op de synthese en eigenschappen van alkali-oxides met gemengd-valente di-zuurstof anionen. Deze materialen bevatten moleculair di-zuurstof in een valentietoestand tussen superoxide (O_2^-) en peroxide (O_2^{2-}). Gemengde valentie in alkali-oxides is een aspect dat tot nu toe nog niet is gerapporteerd in de wetenschappelijke literatuur.

Hoofdstuk 1 geeft een samenvatting van eerdere studies van magnetische alkali-oxides en een overzicht welke verbindingen bestaan en wat bekend is van hun kristalstructuur en magnetische eigenschappen. De relevante magnetische exchange interacties voor alkali-oxides worden besproken en een een algemene achtergrond wordt behandeld van het concept van gemengde valentie en ladingsoverdracht in vaste stoffen. De hoge gevoeligheid van de alkali-oxides voor vocht in lucht maakt het noodzakelijk dat de synthese en verwerking gebeuren in een gecontroleerde atmosfeer. Deze procedures worden beschreven in detail in hoofdstuk 2 en aan het begin van de daarop volgende hoofdstukken. Hoofdstuk 2 beschrijft ook de technieken die gebruikt zijn om de chemische en fysische eigenschappen van de gesynthetiseerde materialen te bepalen.

In hoofdstuk 3 wordt aangetoond dat een reeks van gemengd valente $K_xBa_{1-x}O_2$ verbindingen kunnen worden gestabiliseerd door KO_2 te reageren met $Ba(NO_3)_2$ in vloeibare ammoniak. De concentratie x kan worden gevarieerd tot een maximale waarde x= 0.412. Röntgen- en neutronendiffractie suggereren dat er geen lange afstandsordening van de K^+ en Ba^{2+} kationen is en daarom er ook geen ladingsordening is van de afzonderlijke O_2^- and O_2^{2-} anionen. De magnetische eigenschappen zijn vergelijkbaar voor alle composities. Beneden ∼40K worden de eigenschappen bepaald door wedijverende antiferromagnetische (AFM) en ferromagnetische (FM) interacties en onder ∼5K worden de FM interacties meer prominent in aangelegde magnetische velden. Dit suggereert dat de preparaten inhomogeen zijn en bestaan uit nanodomeinen of clusters met lokaal verschillende magnetische plaatsuitruil interacties. De aard van de magnetische interacties tussen twee nabuur di-zuurstof anionen wordt bepaald door hun lokale kation coördinatie. De preparaten vertonen ook trage spin dynamica. Er wordt een zwakke afhankelijkheid voor de magnetisatie van de koelsnelheid waargenomen. Thermoremanente magnetisatie metingen laten zien dat in een aangelegd magneetveld evenwicht wordt bereikt op een tijdsschaal van enkele uren. Deze eigenschap van $K_xBa_{1-x}O_2$ is een gevolg zowel van de bevroren dynamica als van de energie barrière die ontstaat omdat een heroriëntatie van spinrichting ook een verandering van de oriëntatie van het zuurstof molecuul vereist. $K_xBa_{1-x}O_2$ laat dus een evenwicht zien tussen collectieve elastische interacties tengevolge van anion heroriëntatie en magnetische interacties die bepaald worden door de lokale kation omgeving.

Hoofdstuk 4 beschrijft de Raman experimenten op $K_xBa_{1-x}O_2$ preparaten waarvan de synthese beschreven is in hoofdstuk 3. De spectra worden geanalyseerd met behulp van dichtheidsfunctionaal theorie (DFT) berekeningen. Deze laten zien dat er een aanzienlijke koppeling bestaat tussen nabuur zuurstof moleculen. Deze koppeling wordt in verband gebracht met een redelijk grote mate van ladingsoverdracht. Gebruik makend van de bekende classificatie van Robin en Day, plaatsen we $K_xBa_{1-x}O_2$ op de grens van Klasse II en Klasse III met matig sterke koppeling. In deze verbindingen

worden de redox centra gescheiden door een energie barrière die kan worden overwonnen met externe stimuli. In $K_xBa_{1-x}O_2$ kunnen deze stimuli bestaan uit licht of drukverlaging. Een vergroting van het vermogen van de Raman laser leidt tot een verandering in het spectraalgewicht dat overeenkomt met een hogere mate van ladingsoverdracht. Als het Raman laser vermogen wordt verminderd, keert de verdeling terug naar de oorspronkelijke situatie. De reversibiliteit van dit proces suggereert dat de overgang alleen elektronisch van aard is. Het voorstel is dat de laser een aangeslagen toestand bevolkt waarbij een elektron van een π^* orbitaal van het di-zuurstof anion wordt geëxciteerd naar een hoger liggend σ^* orbitaal. Het resulterend gat in het π^* niveau verhoogt de kans op elektron overdracht van een π^*orbitaal van een naaste nabuur anion. De proces lijkt te worden versterkt in vacuüm, hetgeen nadere studie vergt om te worden begrepen. Bij langdurige bestraling door de Raman laser gedurende enkele uren, worden de Raman lijnen scherper en wordt de fijn structuur beter opgelost. Dit betekent dat de lokale ch emische omgeving van de anionen beter gedefinieerd wordt en dit zou kunnen plaatsvinden ten gevolge van een licht-geïnduceerde kation herordening.

In hoofdstuk 5 wordt een nieuwe route voor de synthese van NaO_2 beschreven zonder dat hoge drukken worden gebruikt. De sleutel is om een mengsel van 70% methylamine en 30% ammoniak te gebruiken. Een hogere concentratie methylamine onderdrukt een nevenreactie van superoxide anionen met ammoniak. Pogingen worden beschreven om onbeantwoorde kwesties van NaO_2 te beantwoorden Het magnetisch gedrag in de marcasiet fase lijkt te berusten op korte-afstand AFM gedrag en de data worden gefit met een één-dimensionale spin keten met een plaatsuitruil parameter J/k_B = -375 K. Dit suggereert sterke overlap van de superoxide p-orbitalen en toont aan dat in principe hoge ordeningstemperaturen mogelijk zijn in de alkali oxides. Het is niet duidelijk uit de huidige data om te oordelen of lange-afstandsordening bij lage temperatuur optreedt ofschoon twee anomalieën optreden in de susceptibiliteit bij 45 K en 60 K die kunnen worden toegeschreven aan magnetische faseovergangen. Bij lage

temperatuur treedt een wedijverende interactie op die ferromagnetisch van aard is door een klein aangelegd magneetveld. Het is waarschijnlijk dat het veld een partiële heroriëntatie induceert van het haltervormig zuurstof molecuul dat FM interacties bevoordeelt. De synthese van een nieuwe oplossing $Na(O_2)_{1-x}(OH)_x$ in ammoniak wordt ook beschreven in hoofdstuk 5. Raman spectroscopie laat zien dat dit een gemengd valente verbinding is met een karakteristiek spectrum van zuurstof-zuurstof strek-vibraties vergelijkbaar met die beschreven voor $K_xBa_{1-x}O_2$ in hoofdstuk 4. Vergelijkbaar met dat systeem is de elektronische koppeling tussen nabuur di-zuurstof anionen in $Na(O_2)_{1-x}(OH)_x$ matig sterk en maakt elektron-overdracht plaatselijk mogelijk. Ofschoon deze verbinding voornamelijk AFM interacties vertoont zonder lange-afstandsordening, nemen we zwak veld-geïnduceerd FM gedrag waar bij lage temperatuur. Dit suggereert dat dubbel-plaatsuitruil optreedt op lokale lengteschaal.

In hoofdstuk 6 wordt aangetoond dat gemengde valentie van alkali superoxides ook kan worden verkregen door het verlagen van de zuurstof stoïchiometrie door gecontroleerde thermische decompositie. Verbindingen met samenstelling $CsO_{1.87}$ and $KO_{1.86}$ zijn gesynthetiseerd en hun structuur en magnetische eigenschappen zijn onderzocht. Beide materialen hebben de kubische wanordelijke pyriet structuur bij kamertemperatuur. $CsO_{1.87}$ wordt tetragonaal onder 240 K als de anionen ordenen parallel aan de c-as. Een vergelijkbare overgang treedt op tussen ∼230 K en ∼280 K in $KO_{1.86}$ die in verband staat met fase coëxistentie die afhangt van de thermische geschiedenis. De magnetische susceptibiliteit van $CsO_{1.87}$ toont aan dat een één-dimensionale AFM spinketen wordt gevormd met J/k_B = -32 K, die is groter is dan in de oorspronkelijke verbinding CsO_2. De zuurstof vacatures leveren een gecomprimeerdere eenheidscel op dan van CsO_2 en waarschijnlijk tot een grotere overlap van de orbitalen die verantwoordelijk zijn voor de één-dimensionale AFM plaatsuitruil. Echter, in tegenstelling tot CsO_2 is er geen aanwijzing voor 3D AFM ordening in de grondtoestand. Het lijkt daarom waarschijnlijk dat de spin-keten meer robuust is in de niet-stoïchiometrische fase. In $KO_{1.86}$ is er geen aanwijzing voor magnetische

orde tot 2 K. Vervolgonderzoek is nodig om te begrijpen waarom de magnetische ordening onderdrukt wordt. Raman spectroscopie suggereert dat zowel $CsO_{1.87}$ and $KO_{1.86}$ kunnen worden beschouwd als gemengd valente materialen. De anion vacatures vereisen dat ieder anion een niet heel-tallig aantal valentie elektronen heeft vanwege ladingsevenwicht en Raman spectroscopie geeft aanwijzingen voor lokaal ladingsoverdracht tussen nabuur anionen. Dit gedrag wordt nog sterker in $KO_{1.86}$ waargenomen waar de anionen sterker zijn samengedrukt en dichter bij elkaar staan. Het opzettelijk aanbrengen van niet-stoïchiometrie in alkali superoxides is daarmee een veelbelovend pad naar nieuwe gemengd valente materialen.

Acknowledgement

Acknowledgements: It's hard to believe that I have finished four and half years in Groningen already. But time moves, so do we. It is therefore; time to thank the many helpful individuals that have played an important part, directly and indirectly, in the successful completion of my thesis. It fills me with immense pleasure to be able to express my gratitude. Yet, it is difficult to express my gratitude completely and I make a humble attempt while fighting a mixture of emotions.

First I choose to express my sincere gratitude to my promoter Prof.Thom Palstra and co-promoter Dr.Graeme Blake. I stand in admiration of you both; for all that you have done to see this thesis through to a completion. Thom, you have been marvelous with your insights and constructive criticism. I remain particularly impressed with the questions you raised and clarity of thought and reasoning, during our discussions. Looking back, I can honestly say, that your words have gone a long way in shaping me as a scientist. I wish I could have had more time to discuss science with you, but I do not doubt that the time we spent was very valuable. I am very happy to have had you as my supervior.

Graeme, my special thanks go to you for being an excellent supervisor. It was nice to have frequent and regular access to you, and to be able to discuss developments at first hand. You were the first person I met in Groningen. I have learnt immensely from you. Discussing with you gave

me a better understanding of many concepts and ideas and I thank you for that. On a more personal level, I enjoyed visiting Oxford and Berlin, with you. I am very thankful to you for all your help and support during my PhD.

I thank Prof. Rob de Groot for your sharing his immense knowledge in theory and introducing me to a new class of materials. You have been particularly motivating in many instances. I still remember your words when I lost my first sample to decomposition, "Nature does not reveal its secrets very easily, we need to try hard to understand it". Many thanks for all your support.

I would also like to thank Prof. Paul van Loosdrecht for helpful discussions, especially with the Raman spectroscopic results and allowing me to use Raman spectrometer. I would like to thank Prof. Beatriz Noheda for organizing the weekly "FUN" meetings and keeping the group active. Your energy has been an inspiration to me. Thanks for all your support.

I would like to thank the members of my reading committee, Prof. Petra Rudolf, Prof. Anthony Maignan and Prof. Catherin Pappas, for their useful comments and inputs for the correction of my thesis. As our work regularly involves sensitive chemicals and instruments, it would be impossible to run experiments without the help of many skilled technicians. Jacob Bass, you have been so helpful all these years. Without you, many things would have been difficult to manage. You are quite social with all the members of the lab, which I find appealing. I have learnt quite a lot from you, I am grateful for your support. I am happy you enjoyed the ZICS cricket and the spicy Indian dishes I made for you. I would also like to thank Henk Bruinenberg. Henk, though I did not work much with you, you have been nice and concerned about me, all these years. I still remember our wadlopen (mud waking) trip to Schiermonnikoog. Henk Bonder, thank you also for being so nice and friendly with me during these days. Also, many thanks for the gold electrodes you made for my electrical measurements. I would also like to thank Ben Hesp and Anthoni Caretta for their help in Raman measurements. Ben, thanks so much for being kind to me and helping

me in absorption measurements. Tony, despite getting a bit impatient, occasionally, during our measurements, you helped me a great deal with setting up the experiments. I like to thank you for all the help you and for the nice time we had during our London trip. I would also like to thank Maarten, from the glass work shop. Maarten you have been so kind and helpful throughout. My thanks also go to Gert Alberda van Ekenstein from the polymer group, for the low temperature DSC measurements. Thanks Gert for your kind help and discussion regarding DSC. I would like thank also Hans van der Velde for helping me with ICP analysis of my samples. My thanks also go to Wesley Browne for his initial Raman spectroscopic measurements. The SEM is done with the help of Gert ten Brink from the Department of Nanostructured Materials and Interfaces. Gert thanks a lot for the help you did for me. My thanks also go to Ms. Annette Korringa-de Wit and Ms. Yvonne van der Weerd from the Graduate School of Science for quickly organizing the paper work for me.

Many people like Dr.L.S.Nadeesh, Prof.Arun M.Umarji, Prof.K.C.Patil, Prof S.A.Shivashankar ,Prof.Vasudev Naik and Dr Y.S.Arthoba Naik have influenced my journey towards science and research. I am very fortunate to meet you all and would like to thank all for your support. I have been so fortunate to have colleagues(IISc) and friends like Nagesh Kini , Joyita, Ujwala, Geetika, Girish, Ankur, Suresh and Venki. Dear all, thanks a lot for your whole hearted support during my time in IISc.

In order to have good research, one also needs an active and conducive environment. I thank all my colleagues, who have created such a friendly and active environment. Syarif (my office-mate and project-mate for last four years!), I enjoyed working with you. We were great team and I learnt lot from you. Thanks so much and have fun with pigments or colors! Baomin, you have been a wonderful collaborator. We had great discussions and I really appreciate your energy and enthusiasm. It was great to cooperate with you. All the best for your career in the days ahead. Anne, thanks for organizing the football matches and group trips. Johan, Gijsbert, Ard, Christophe, Jeroen, Saeedeh, Alex, Oleksiy, Kalyani, Sylvia,

Jacob, Henk, Anil, Guowei, Mai, Igor, Mufti, Umut, Aisha, Arnoud, Jose, Thomas, Sander and Alwin and all visitors: thank you all for all your suuport.

Life outside the lab has also been wonderful due to many friends, who helped and shared things with me. Out of all, I have quite a lot to say about two guys with whom I spend a lot of time. Adi and Ashoka, you have been so kind and nice all these years. I like to address you as "Adi & Ashoka", though I know that you guys don't like it! As you know, we had lot of fun in Groningen, with some crazy things we did. I have always been impressed with the energy you guys have. I have learnt lot from you. I will cherish these memories, I have spent with you for rest of my life. Thanks for being wonderful friends. Have fun in the US. Harsh, Thanks for the fun time we had in Plutolaan, during the DGW (Desis Gone wild) days, and cricket at ZICS. I would like to thank many others for spending their time with me, for cooking numerous dinners with delicious food. Particularly, Lakshmi (Delicious food and time in DGW), Kiran (Thanks for the cricket and typical comments and remarks) Bhushan and Prachi, Yamini, Gopi, Santanu, Praveen, Subhradeep, Shirish, Gourav, Subir, Siddesh, Shivashankar, Khayum, Appu, Milon , Suresh , Eshwar , Raju , Pranav, Praneeth , Goutham , Arun, Akshay, Ashwin, Rama Kataria, Amol & Sneha, Saumen Paul, Afzal Rana and all ZICS members. I am sorry If I miss any one I like to thank them from bottom of my heart.

I like thank specially to my paranymfen Adi and Jacob for, helping me in finishing things the way I want.

My special thanks go to young and talented artist, Yamani, for sketching the cover page of my thesis. Yamini, I was really impressed with the way you understand my views and could present it beautifully. Thanks for spending your valuable time for this, and inviting me for nice Indian tea and onion pakura. I should ask to make one more PhD thesis cover page, just for the onion pakura and Indian tea. Gopi, thanks for your help and support in this cover page.

After working time, nice and peaceful house is very much needed. I am

really fortunate to have very diverse, helpful and understanding housemates over all these years in Groningen.The experience in the student house with international students was s memorable and nice. I like to thank Housing Office for this. During my stay in Groningen I had to stay in different places, so that with different house mates like Marcel Trip (Thanks for nice movies) Jeroen Koeten (I am sorry I could not get the chicken pickel for you) Leena Kleinebecker (for wonderful parties), Christine (Thanks for keeping house clean and tidy all the time) Malte, (Thanks for video games and cleaning rota), Christina (Thanks for your nightmare stories, sharing your experiences of the India trip and of course for teaching me a bit of German), Caroline (thanks for nice coffee from your new coffee machine, long and funny conversations about Addidas and Apple), Henriet (thanks for being nice to me), Michael(thanks for your philosophical views), Jana(thanks for introducing me your dog Iama). During my stay, GISA has been organizing Indian traditional events at regular intervals and so I never had to miss home. It was nice to be given a chance to perform group songs and folk dance during our stay here. I like to thank to GISA and all members for all the support. During my PhD, many people and friends in India also helped in many instance. Rudresh, thanks for being such a supportive friend and tolerating me; Ramesh; Ravi ; Mahesh, thanks for being so helpful all the time when I needed; Harish thanks for being so helpful and taking care of things at home and helping our family; Suresh; Hemanth; Thontesh; Raghu and Bharath and all other friends for their support. During the PhD I have been supported by all my family members I like to thank all of them. Last but not least, Ma and Pa, I have been so lucky to have parents like you. Despite your emotional blackmails, you have been so understanding, supportive and encouraging all these years. From the beginning you gave me so much freedom to take my own decisions. I really respect that. With out your support and encouragement, it would have been impossible for me to stand where I am today. I will not say thank you but I will ask your blessings always. My lovely sister Bhavya, you have been very understanding and have always respected my thoughts. Thanks so much for it. Bhavya and

Chandan, thank you both for your support and you both shall be my best friends forever.

In life's journey, one often meets many people and many things happen because of them. Sometimes, these happenings are noticeable and significant and sometimes not. So I like to thank whole-heartedly all who support and helped me. If I miss anyone, please don't hesitate to stop me, kick me and remind me about this, as mistakes also need recognition.

September 2012
Groningen
Shivakumara Giriyapura